

The Origin and Development  
of a  
Tropical Mesoscale Cloud Line

by

FRANK DECATUR MARKS, JR.

S.B., Belknap College  
(1973)

S.M., Massachusetts Institute of Technology  
(1975)

SUBMITTED IN PARTIAL FULFILLMENT  
OF THE REQUIREMENTS FOR THE  
DEGREE OF  
DOCTOR OF SCIENCE

at the

MASSACHUSETTS INSTITUTE OF TECHNOLOGY

June 13, 1980  
*(i.e. February, 1981)*

© Massachusetts Institute of Technology 1980

Signature of Author \_\_\_\_\_

*1*  
Department of Meteorology, June 13, 1980

Certified by \_\_\_\_\_

Frederick Sanders, Thesis Supervisor

Accepted by \_\_\_\_\_

Chairman, Department Committee

**WITHDRAWN**  
MASSACHUSETTS INSTITUTE  
OF TECHNOLOGY  
**FROM**  
MIT LIBRARIES  
LIBRARIES

**The Origin and Development  
of a  
Tropical Mesoscale Cloud Line**

by

Frank D. Marks, Jr.

Submitted to the Department of Meteorology  
on 13 June 1980 in partial fulfillment of  
the requirements for the degree of  
Doctor of Science

**Abstract**

Long narrow lines of precipitating convection that form off the west coast of Africa in the summer are described from satellite, rawinsonde, and quantitative radar data taken during the field phase of the GARP Atlantic Tropical Experiment (GATE). The lines appeared on the satellite images in the eastern Atlantic, west of the coast of Africa near 15°N, along the leading edge of large dust plumes that emerged from the desert regions of Africa in the ridge region of traveling synoptic-scale waves. Analysis of the wave structure showed that the lines were in a region of strong negative relative vorticity and easterly vertical wind shear in the lower and mid-troposphere but with little surface convergence. On the basis of precipitation analyses derived from the radar measurements, the lines were found to contribute about 20-25 percent of the precipitation associated with the waves.

The convective lines were about 400 - 1000 km in length, but only 25 - 35 km wide, and they moved slowly toward the south - southwest at speeds of 4 - 6 m s<sup>-1</sup>. The cloud tops in the lines were typically only 3 - 4 km when the lines were north of the region of low-level convergence associated with the monsoon trough in the eastern Atlantic Ocean. The character of the lines changed dramatically, however, when they propagated into the monsoon trough region where the convection deepened and the lines widened considerably.

A detailed analysis of one line that affected the GATE ship array is presented. Fields of divergence, vorticity, and resultant deformation, together with cross - sections of wind and thermodynamic variables derived from the 6 - h upperair data, were used to determine the structure of the lower troposphere in the regions where the long convective line formed and moved. The analyses showed that the line was positioned in the wave ridge at the southern boundary of a layer of hot, dry, midtropospheric air, just north of a strong easterly midtropospheric jet. The boundary of the hot dry air layer was characterized by sharp temperature and humidity gradients, 2.4 - 3.3 K (100 km)<sup>-1</sup> and 3 - 4 g kg<sup>-1</sup> (100 km)<sup>-1</sup>,

respectively. The line formed in the exit region of a midtropospheric jet streak along the boundary of the SAL as the jet streak propagated across the west coast of Africa. The kinematic properties of the flow in this region were characterized by divergence and strong resultant deformation. The axis of dilatation was aligned perpendicular to the line as well as wind shear in the lower troposphere. Thus, ruling out the possibility that the convective line formed as a result of a frontogenetical circulation. However, the analyses also showed that the line formed in a region of very low and slightly negative potential vorticity. An indication that the flow might have been unstable to symmetric inertial circulations that could act to organize the convection into a line. Later in the lifetime of the convective line, it entered a region of positive potential vorticity, convergence, and high resultant deformation. In this region, the axis of dilatation was aligned along the cloud line and the shear vector in the lower troposphere, indicating that a frontogenetical type mechanism may have been acting to maintain the organization of the convection in a line. Computation of the frontogenetical function, as defined by Petterson (1956), indicated that, in the absence of diabatic processes and differential vertical advectons, the observed values of deformation would have doubled the existing thermal gradient in one day. This computation suggests that a frontogenetical circulation probably acted to maintain the convective line structure later in its lifetime.

The role of symmetric inertial instability in organizing the convection is discussed. Comparison of theory with observations indicates that inertial instability is a likely mechanism for the organization of the line. The origin of the inertially unstable air is investigated on the basis of the mean kinematic and thermodynamic structure in the flow upstream near the coast of Africa and inland over the Sahara. Synoptic-scale waves develop south of the central portions of the desert between 10 - 20°E. The wave amplitudes typically increase between 10°E and 0° longitude, and are a maximum near 20°N at the surface. Within and just east of the wave ridge, the air parcels in the lower troposphere have the lowest positive potential vorticity. As the waves travel westward over the desert, it is hypothesized that the potential vorticity of the lower tropospheric air parcels is rapidly destroyed by strong diabatic heating near the surface, and that in the wave ridge the potential vorticity approaches zero. The diabatic heating over the desert destroys positive potential vorticity, but it will not make the potential vorticity negative.

Two mechanisms that can generate negative potential vorticity in the lower troposphere are discussed one in the midtroposphere over the Sahara, and the other in the lower troposphere along the coast of West Africa. Over the Sahara, in the midtroposphere north of the jet maximum, differential vertical turbulent momentum flux divergence across the southern boundary of the hot, dry air layer can act to generate negative potential vorticity. The air parcels north of the jet maximum are vigorously mixed in the vertical, transporting low momentum air up into the midtroposphere and higher momentum air down to the lower troposphere. South of the hot, dry air layer, in the vicinity of the jet maximum, the vertical mixing is greatly reduced. The differential momentum flux reduces the component of the absolute vorticity along the potential temperature gradient by generation of negative relative vorticity north of the jet streak.

As the waves cross the west coast of Africa, the air parcels in the ridge come into contact with a relatively cool sea surface and there is a rapid change in diabatic heating near the surface that causes the potential vorticity to become negative in the lower troposphere.

Thesis Supervisor: Frederick Sanders  
Title: Professor of Meteorology

To my wife

Anita

### Acknowledgements

I am deeply grateful to my two principal advisors, Dr. Pauline Austin and Prof. Frederick Sanders, for their advice, patience, and stimulation during the course of my graduate work. Many other people at M.I.T. were also very helpful. I would particularly like to thank Dr. Robert Burpee, whose help speeded up the completion of this thesis. I am grateful to George Huffman and Prof. Peter Stone for many helpful discussions on potential vorticity which were useful in the development of chapter 4. Also, I would like to thank my friends and colleagues in the Weather Radar Project, Spiros (Speed) Geotis, Alan and Ginny Siggia, Bill Silver, Mark Merritt, and Barbara Wysochansky, who helped me greatly through their technical skills and friendship through good times and bad. I would also like to thank the past and present members of the convection club, George Huffman, John Gyakum, Frank Colby, Prof. Sanders, Prof. Lance Bosart, Dr. David Randall, Prof. Richard Passarelli, and Dr. Burpee for many stimulating conversations and constructive criticism during the course of my work. I would like to thank Sam Ricci for drafting the figures.

I especially thank my wife, Anita, and my daughter, Sara, for their love, patience, and understanding during the course of this research. Without them, I never would have finished this thesis. I would also like to thank the many friends and colleagues working with the GATE data sets who kindly supplied me with data and advice during the course of this research. I would particularly like to thank Dr. Michael Hudlow, of NOAA's Hydrologic Research Laboratory, for his help in acquiring and using the GATE radar data set. His help and advice kept me going during the early stages of my research. I would like to thank Dr. Vic Ooyama, currently at NHRL, for the use of his analyses of the GATE rawinsonde data which was useful in the case study in chapter 3. Prof. Richard Reed, of the University of Washington, kindly supplied me with his composite wave analyses which were used in chapter 2. I would also like to thank Dr. Edward Zipser, of NCAR, for allowing me to spend a week at NCAR to access GATE data archived there. His interest in my work and his comments on the mesoscale organization of deep convection are gratefully acknowledged.

My financial support during this research came from an M.I.T. research assistantship supported by NSF grants ATM77-12534 and ATM78-00232.

This thesis was printed using the text processing facilities of the M.I.T. Artificial Intelligence Laboratory.

## Table of Contents

<b>Abstract</b>	<b>2</b>
<b>Dedication</b>	<b>5</b>
<b>Acknowledgements</b>	<b>6</b>
<b>Table of Contents</b>	<b>7</b>
<b>1. Introduction</b>	<b>9</b>
<b>2. Synoptic-scale and mesoscale organization of convection during GATE</b>	<b>14</b>
2.1 Synoptic-scale organization of convection during GATE	14
2.2 Mesoscale organization of convection during GATE	19
2.2.1 <i>General characteristics of mesoscale features</i>	19
2.2.2 <i>Features in the monsoon trough zone</i>	23
2.2.3 <i>Features north of the monsoon trough region</i>	27
2.3 Role of African waves in organizing mesoscale features during GATE	30
<b>3. Case study of lines that form north of the monsoon trough</b>	<b>35</b>
3.1 Development and movement of the narrow convective line	35
3.1.1 <i>Synoptic-scale features</i>	36
3.1.2 <i>Convective structure</i>	42
3.1.3 <i>Vertical atmospheric structure near the convective line</i>	45
3.2 Kinematic fields in the vicinity of the convective line	47
3.3 Discussion of the formation and maintenance of the convective line	50
3.3.1 <i>Formation of the convective line</i>	50
3.3.2 <i>Maintenance of the convective line</i>	53
<b>4. Discussion of symmetric inertial instability and the origin of the negative potential vorticity</b>	<b>57</b>
4.1 Role of symmetric inertial instability in organizing convective lines	57
4.1.1 <i>Conditions for symmetric inertial instability</i>	57
4.1.2 <i>Growth rate of a symmetrically unstable perturbation</i>	59
4.1.3 <i>Structure and dimensions of symmetrically unstable circulations</i>	61
4.1.4 <i>Organization of convection by symmetrically unstable circulations</i>	63
4.2 Origin of inertially unstable airmass	65
4.2.1 <i>Mean conditions over central west Africa</i>	66
4.2.2 <i>Time rate of change of potential vorticity</i>	67
4.2.3 <i>Destruction of positive potential vorticity</i>	69
4.2.4 <i>Generation of negative potential vorticity</i>	73
<b>5. Summary and suggestions for future study</b>	<b>81</b>
5.1 Summary	81
5.2 Suggestions for future study	84

<b>Tables</b>	<b>88</b>
<b>Figures</b>	<b>93</b>
<b>References</b>	<b>139</b>
<b>Biographical Note</b>	<b>145</b>

## 1. Introduction

The importance of deep cumulus convection to the large-scale tropical circulation was first recognized by Riehl and Malkus (1958). They argued that virtually all the upward heat and mass transfer in the equatorial trough zone takes place in a few tall cumulus clouds or "hot towers". Since these convective transports have a fundamental role in the maintenance of the large-scale circulation in the tropics, it is necessary to identify the mechanisms that determine where these "hot towers" occur, before the impact of smaller-scale convective systems can be treated adequately in a model of the large-scale tropical circulation. One of the central unsolved problems in the tropics is the determination of the mechanism or mechanisms by which deep convection is organized in the intertropical convergence zone, synoptic-scale convergence zones, waves, and vortices over the tropical oceans.

Early studies of the organization of deep convection over the tropical oceans first pointed out the synoptic-scale patterns, and consequently much of the work on tropical disturbances prior to the mid-1960's assumed the convection was controlled by synoptic-scale mechanisms (e.g. Piersig, 1936; Dunn, 1940; Riehl, 1948). The advent of meteorological satellites in the early-1960's provided evidence that the deep convection over the tropical oceans was often organized on scales smaller than that of the synoptic-scale disturbances. By the late-1960's satellite images provided a view of clouds over large areas of the tropical oceans at frequent intervals. These images showed that deep convective activity over the tropical oceans tended to be organized in convective "clusters", with dimensions of a few hundred kilometers. Frequently, the clusters were organized in lines, some of which were aligned with the intertropical convergence zone (e.g.

Anderson *et al.*, 1969; Joint Organizing Committee for GARP, 1970). The cloud clusters were found to persist for short time periods and, at times, appeared to be distributed at random, which led some researchers to question the importance of synoptic-scale mechanisms in organizing deep convection. However, Frank (1971), in a study of 674 cloud clusters identified during the summers of 1969 and 1970, showed that 85 percent of the clusters were associated with synoptic systems. He hypothesized that these systems apparently provided a favorable setting for the growth of mesoscale convective processes. Within the synoptic systems, however, the convection in the clusters was observed to be quite variable. This observation led to an increased interest in the internal structure of the clusters.

While the satellite images pointed out the existence of the clusters, the large areas of cirrus cloud produced by the convection in the clusters tended to obscure the internal structure of the clusters. The extent to which the deep convection within cloud clusters is organized on the mesoscale became apparent from observations made in the first few large tropical field experiments in the late 1960's. Using aircraft and rawinsonde measurements taken during the Line Islands Experiment in 1967, Zipser (1969) described a case in which the deep convection within a cloud cluster was organized on the mesoscale. He found that the convective organization was similar to that seen in squall lines observed over land in the mid-latitudes. The characteristics of cloud populations typically present in cloud clusters over the Caribbean were determined by López (1973, 1976), using aircraft radar measurements taken as part of the 1968 Barbados Meteorological Experiment. He determined that convection in the clusters was very complicated, having a large range of scales, from numerous small, independent echoes with areas on the order of  $10 \text{ km}^2$ , to a few extremely large line or band echoes with areas on the

order of  $10^3 \text{ km}^2$ . López also noted that while the small, independent echoes were more numerous, they were typically much shallower and shorter lived than the larger echoes. Estimates of the strength of the mesoscale systems observed in cloud clusters were obtained by Smith *et al.*, (1975 a, b) from an analysis of one system during the Barbados Oceanographic and Meteorological Experiment (BOMEX) in 1969. They found that the vertical motions in the mesoscale system were an order of magnitude greater than those associated with the synoptic-scale wave, and that the integrated vertical mass-flux in the mesoscale system was comparable to that produced by the synoptic-scale wave.

While these studies documented the existence and relative strength of mesoscale circulations within the cloud clusters, very little was known about how these circulations originated or how they interacted with the synoptic-scale patterns. To obtain measurements of the interactions between the synoptic scale, mesoscale, and convective scale over the tropical oceans, the Global Atmospheric Research Program (GARP) initiated the GARP Atlantic Tropical Experiment (GATE) during the summer of 1974. GATE was designed to identify and describe the different scales of organization of deep convection, and to estimate the effects of small-scale tropical weather systems on the larger scales over the eastern Atlantic Ocean (Kuettner *et al.*, 1974). To describe the weather systems on different scales, observations were made with a number of instrumented platforms that were positioned over the eastern Atlantic Ocean within the region of low-level convergence, referred to by Sadler (1975) as the monsoon-trough zone. Shipborne rawinsonde and surface observations were taken to determine the structure of the different circulations, while satellite and shipborne radar observations were made to describe precipitation and cloud features.

The deep convection observed during GATE was organized on both the synoptic and mesoscale. Studies of westward traveling synoptic-scale waves during Phase III of GATE showed a pronounced modulation of deep convection and precipitation by the waves (e.g. Payne and McGarry, 1977; Reed *et al.*, 1977). These studies indicated that measurements of cloudiness and precipitation, at and just downstream of the wave trough, exceeded those near the ridge by a factor of more than two. Radar studies from GATE pointed out that a large fraction of the precipitation was observed in mesoscale disturbances, typically lines, small compared to the scale of the convective clusters observed by satellite, but large compared to an individual convective cloud (e.g. Houze and Cheng, 1977; Marks and Hudlow, 1976). However, Pestaina-Haynes and Austin (1976) showed that these mesoscale lines had large variations in motion and speed. For example, Houze (1977) and Zipser (1977) identified and described two separate fast moving lines of deep convection that they referred to as "squall lines", while Leary and Houze (1979) discussed the movement and structure of several different slower-moving line systems in a single cloud cluster. The squall lines were easily distinguished from the slower moving lines on the radar maps and satellite images, not only because of their rapid motion, but also because of their sharp and generally arc-shaped leading edge. However, both the squall lines and the slower-moving lines had a very similar "life-cycle" or sequence of events as the line intensified, matured, and decayed (Leary and Houze, 1979). Within one mesoscale circulation, Zipser and Gautier (1978) estimated that the upward vertical mass flux was comparable to and larger than that on the synoptic scale. They also found areas of mesoscale sinking, on scales of  $100 \text{ km}^2$ , that compensated for the excess (over the synoptic-scale) mass flux in the areas of mesoscale ascent.

While many of the main features of the structure and life of the mesoscale lines in GATE

appear to be similar, it is quite likely that more than one physical mechanism accounts for the origin of the different convective systems. The strong modulation of precipitating convection by the synoptic-scale waves during GATE suggests that some of these mechanisms that organize deep convection may be linked to the structure of the waves. One such mechanism is investigated in this thesis. In chapter 2, the mean structure of the waves observed during GATE is described and the principal mesoscale precipitation features that typically occur within the waves are identified. The second part of the thesis, presented in chapters 3 and 4, focuses on one type of mesoscale line organization. The structure, morphology, and typical region of occurrence of this line are described, and a physical hypothesis that accounts for its origin and maintenance within the context of the synoptic-scale waves is presented.

## **2. Synoptic-scale and mesoscale organization of convection during GATE**

### **2.1 Synoptic-scale organization of convection during GATE**

For many years, westward propagating synoptic-scale disturbances have been observed during the summer months near the coast of West Africa (Piersig, 1936) and in the Caribbean (Dunn, 1940). Analyses completed by Riehl (1948) showed that these wave disturbances modulated the patterns of deep convective activity in the Caribbean. Later, as satellite imagery became available, Arnold (1966) and Frank (1969) showed that these African wave disturbances also influenced the distribution of deep convection over western Africa and the Atlantic Ocean. Carlson (1969a, b) and Burpee (1972, 1974) made extensive studies of the structure and behavior of the African wave disturbances. Their studies showed that the waves typically cross tropical Africa south of the Sahara from mid-June until early October, with wavelengths ranging from 1500 - 4000 km, periods from 2.2 to 5.5 days, and a westward speed of 5 - 10 m s<sup>-1</sup>. The waves had their maximum amplitude in the meridional wind component at around 700 mb during the latter part of August and September. Burpee (1972) discussed the origin of the African waves and pointed out that typically the waves appeared first at pressure levels of 600 - 700 mb near 10°E in central tropical Africa. He hypothesized that the waves were a result of an instability of the midtropospheric easterly jet that was found within the baroclinic zone south of the Sahara in the summer. From satellite images, Carlson (1969b) found an increase in cloud cover just to the west of the wave trough, and an indication that the precipitation amounts were also larger prior to the passage of the trough than they were after trough passage. It was clear from these studies

that the waves modulated the cloud clusters and precipitation over Africa and the eastern tropical Atlantic, but the magnitude of the modulation was not quantitatively known.

Reed *et al.* (1977a, b), and Norquist *et al.* (1977) have identified eight wave disturbances in Phase III of GATE and the preceding interphase (21 August - 21 September 1974) when the waves were most clearly defined. They found that the characteristics of these eight waves were qualitatively similar to those found in studies prior to GATE. The 700-mb positive vorticity center of the disturbances propagated toward the west in a zone of cyclonic shear to the south of the 700-mb easterly jet which was centered between 16 and 17°N. The mean latitude of the center tracks was 11°N over land, and 12°N over the eastern Atlantic. The mean wavelength of the disturbance was about 2500 km with a period of 3.5 days, very close to those reported by Carlson (1969a,b), as well as by Burpee and Dugdale (1975) and Burpee (1975) from their preliminary GATE findings for waves in all three phases of GATE.

Reed and his colleagues used the rawinsonde data from GATE in the region of western Africa and the eastern Atlantic to determine the mean three-dimensional structure and the energetics of the waves. The data for the land and ocean stations were analyzed separately. Except for the surface circulation, however, the differences in wave structure between the two analyses were too small to justify presenting separate results. At the surface over the Sahara, the monsoon trough zone was typically located near 20°N, while over the ship arrays it was generally near 8 - 10°N, resulting in a northeast - southwest tilt of the trough zone over the eastern Atlantic. In association with the displacement of the monsoon trough toward the south over the ocean, there was a corresponding southward displacement of the surface circulation center. Over the land, there tended to be two cyclonic circulation centers, one in the monsoon

trough near  $20^{\circ}\text{N}$  and a second south of the 700-mb vorticity center at about  $10^{\circ}\text{N}$ . These two centers tended to merge into one circulation center over the ocean near  $8 - 10^{\circ}\text{N}$ . Figure 1 shows the structure of the composite wave at three different pressure levels for the combined land and ocean regions. The position of the cyclonic circulation center of the total wind field shown in Fig. 1 a was located between that of the perturbation circulation center (not shown) for both land and ocean regions. To derive the mean structure Reed *et al.* (1977a) used a compositing technique similar to that used by Reed and Recker (1971). The procedure consisted of dividing the wave into eight categories in the east - west direction that were defined by the wind field associated with the waves at 700 mb and at a latitude of the mean disturbance track, approximately  $11.5^{\circ}\text{N}$ . The observations were placed into their respective categories and averaged. Category 2 was centered on the region of the maximum northerly wind component, category 4 on the trough, category 6 on the region of the maximum southerly component, and category 8 on the ridge. Categories 1, 3, 5, and 7 occupied the intermediate locations. In the north - south direction, the observations were averaged by  $4^{\circ}$  latitude bands, with the middle band centered on the average latitude of the disturbance path. Since the categories were defined at one pressure level (700 mb) and at one latitude ( $11.5^{\circ}\text{N}$ ), any mean horizontal or vertical tilt of wave features were identified at other pressure levels and latitude bands.

The surface and 850-mb divergence deviation from the zonal mean, and vorticity analyses from Reed's composite wave are shown in Fig. 2. The mean structure of the waves in the lower troposphere is in good agreement with that expected from quasi-geostrophic theory for a wave embedded in a region of easterly vertical wind shear. Reed *et al.* (1977) found that the composite disturbance was strongest near 700 mb and the maximum low-level convergence

occurred just west of the positive vorticity center in the wave trough. The energy budget for the composite wave, discussed by Norquist *et al.* (1977) and Reed *et al.* (1977b), showed that the baroclinic and barotropic energy conversions were equally important in the maintenance of the wave, confirming the results presented by Burpee (1972).

As shown in Fig. 3 a, the 850-mb vertical velocity deviation from the zonal mean for Reed's composite wave had a maximum just to the west of the trough position. The cloud cover, as indicated by the infrared satellite images, and the precipitation amounts, recorded by the synoptic-scale observation network, were also a maximum just west of the wave trough as shown in Figs. 3 b and 3 c (Payne and McGarry, 1977; Reed, 1978). The composite wave categories 2 and 3, just ahead of the trough, had more than twice the amount of precipitation and percent cloud cover compared to the amount that occurred in wave categories 6 and 7, indicating a relatively strong modulation of the convective activity by the waves in Phase III. The magnitude of the low-level vertical velocity was a maximum to the north of the mean disturbance track, while the maxima of precipitation and cloud cover occurred to the south of the disturbance track. The patterns of cloud cover and precipitation north of the disturbance track are consistent with the lack of low-level moisture, on the southern fringe of the Sahara and the subtropical Atlantic Ocean. South of the disturbance track, in the wave categories west of the trough, the maxima of low-level convergence, vertical velocity, cloud cover, and precipitation all tended to tilt from northeast to southwest (like the trough itself). In the wave categories east of the wave trough there was very little tilt of these maxima. The tilt to the west of the wave trough was apparently a result of the wave modulation of the monsoon trough zone. In the region of interest, the monsoon trough zone was the boundary between low-level southwesterly

winds, which were located over the southern regions of west Africa and the eastern equatorial Atlantic near the African coast, and the northeasterly winds over the southern portions of the Sahara and the eastern tropical Atlantic. During Phase III, the convergence in the monsoon trough zone was modulated by the interaction of the low-level wave circulations. West of the wave trough, but east of the wave ridge, the increased low-level northerly flow in the wave tilted the convergence zone toward the south, while east of the wave trough the low-level southerly flow in the wave tilted the convergence zone toward the north.

A study by Thompson *et al.* (1979) emphasized the close correspondence in time between the vertical mass, heat, and moisture fluxes on the wave scale and the precipitation computed from the radars during Phase III. The wave fields were determined by fitting low-order polynomials to the three - hourly ship rawinsonde data using the method of least squares. Thompson and his colleagues composited the three - hour data values for six waves identified during Phase III following the method employed by Reed *et al.* (1977a), with the exception that the east - west categories were defined by the wind field at 700 mb at the latitude and longitude of the center of the GATE ship arrays, 8.5°N, 23.5°W. In these analyses no latitudinal or longitudinal variation was considered. Figure 4 shows the GATE ship arrays and Table 1 lists the name, location, and country of each ship in the arrays. The wave structure from the study by Thompson *et al.* (1979) was very similar to that described by Reed *et al.* (1977a). The moisture convergence varied strongly with wave position, but correlated well with the observed variation in rainfall. Thompson *et al.* (1979) also obtained moisture budgets that were nearly balanced for two individual waves and for the composite wave.

Reeves *et al.* (1979) have shown that over the B-scale array during Phase III the major

precipitation events corresponded closely in time to the passage of the cyclonic maxima of the 700-mb relative vorticity, in agreement with the results of Reed *et al.* (1977a) and Thompson *et al.* (1979). They also pointed out that during Phases I and II, the close correspondence between the 700-mb vorticity and the precipitation was not as evident. However, during all three phases the major precipitation events were closely related to the synoptic-scale 700-mb upward vertical-velocity maxima and surface convergence.

## 2.2 Mesoscale organization of convection during GATE

### *2.2.1 General characteristics of mesoscale features*

A number of investigators have used quantitative radar data to identify and describe different mesoscale precipitation features observed during the field phase of GATE: Houze and Cheng (1977), Houze (1977), and Leary and Houze (1979), to name three. These analyses concentrated on specific case studies and general statistical analyses. Their findings indicated that the majority of the precipitating convection in the GATE region was organized on the mesoscale and that the organization typically had the shape of lines, the behavior of which varied from case to case.

In view of the strong modulation of the precipitation by the traveling wave disturbances and the preponderance of mesoscale organization of the precipitating convection, it was decided to survey the mesoscale precipitation features within the waves in the GATE region during Phase III. The principal types of mesoscale organization were identified from satellite images

and from merged radar maps constructed from the available C-band radar data taken during Phase III. The positions of the four ships with the C-band radar systems and the area covered by the merged radar maps are indicated in Fig. 4.

The radar data used to construct the merged maps were in the form of low-level Cartesian maps of equivalent reflectivity factor (dBZ) with a horizontal resolution of  $4 \times 4$  km at 15-min intervals. The reflectivity data were calibrated for each individual radar system, and corrections for atmospheric gas attenuation and biases based on intercomparison of the different radar systems were added to the reflectivity maps before merging. The characteristics of the radar systems and the details of the intercomparison analyses are described by Hudlow *et al.* (1979). The Cartesian data were merged at three-hour intervals for all of Phase III to make maps that covered an area of about  $5 \times 10^5$  km<sup>2</sup> and were centered on the B-scale array (Fig. 4). During periods of active convection, hourly maps were constructed to aid in the identification of important features. The merged maps and satellite images were grouped by wave category at the center of the B-scale ship array for five of the six waves identified by Thompson *et al.* (1979) in Phase III. The dates of the passage of each of the five troughs at the center of the B-scale array are listed in Table 2. The first wave that was identified by Thompson and his colleagues was omitted from the survey because part of the wave had crossed the region of the ship arrays before the ships were in position.

The results of the survey of mesoscale precipitation features are schematically illustrated in Fig. 5 along with the surface and 700-mb streamlines from the Reed *et al.* (1977a) composite wave for the combined land and ocean regions. The combined composite is shown rather than the oceanic composite that was based on measurements made nearer the radar and satellite

observations for two reasons: first, there was very little difference in the structure of the waves over land and ocean regions, and second, a much larger data sample was included in making the combined composite. As can be seen in Fig. 5, the organization of deep precipitating convection was rare in the categories downstream from the ridge (5, 6, and 7). This was the same region of the wave where Reed *et al.* (1977a) and Thompson *et al.* (1979) computed the lowest precipitation amounts. The clouds in this region of the wave were typically very shallow and organized in arcs and streets that were oriented along the low-level southerly wind shear (e.g. Warner *et al.*, 1979). Organization of precipitating convection into lines was most frequent in the wave categories corresponding to the northerly flow that occurred just west of the trough. This was also the region of the wave where the largest precipitation amounts were observed. In this region, three principal types of mesoscale organization of precipitating convection were identified: squall lines and non-squall bands of deep convection (referred to as monsoon trough bands in the remainder of the text) that appeared within the low-level convergence of the monsoon trough, and long narrow lines of convection that formed north of the monsoon trough region.

The precipitation amounts produced by these three types of mesoscale features were determined from the quantitative radar data. Maps of hourly precipitation estimates were derived at the GATE Convection Subprogram Data Center (Hudlow and Patterson, 1979) with a spatial resolution of 4 X 4 km for a 200-km radius circle centered on the B-scale ship array (referred to as the Master Array by Hudlow, 1979). The area covered by the Master Array is outlined in Fig. 4. Hudlow and Patterson (1979) and Hudlow (1979) have described the methods used to compute the precipitation maps from the radar data and discussed the quality of these maps. A time - latitude precipitation map was constructed by computing three - hour

averages of the precipitation amounts in the Master Array for seven areas, each of which measured a half-degree latitude by a half-degree of longitude and was centered on 23.5°W. The time - latitude precipitation map is shown in Fig. 6 along with a time series of wave category determined by Thompson *et al.* (1979) at the center of the B-scale ship array every three hours. The amount of precipitation associated with each of the mesoscale features identified on the merged maps was computed from the hourly precipitation maps. These precipitation amounts were used to determine the contribution of each type of mesoscale feature to the precipitation within every 0.5°X 0.5° block in the time - latitude map. Then each three-hour latitude block was stratified according to both the wave category at the center of the B-scale array at that time, and the type of mesoscale organization.

The results of the precipitation analyses, corresponding to the time series in Fig. 6, are shown in Fig. 7 a - d. The values analyzed in the four frames are the mean precipitation rates for the composite wave, the monsoon trough bands, the squall lines, and the long narrow bands, respectively. The number in the top left hand corner of each frame denotes the mean precipitation rate for that frame. Within the latitude band covered by the precipitation analyses, the monsoon trough bands and the squall lines produced almost 60 percent of the measured precipitation in the wave; the monsoon trough bands contributed primarily in wave categories 3 - 4, and the squall lines in categories 2 - 3. The long narrow lines that formed north of the monsoon trough region made up 20 - 25 percent of the precipitation in the composite wave, primarily in wave categories 1 - 3. The remaining 15 - 20 percent of the precipitation was accounted for by isolated convective features in the wave categories downstream from the ridge (5, 6, and 7). However, 60 percent of the total precipitation amount which fell in these wave

categories (5 - 7), occurred in categories 5 - 7 of the second wave disturbance. Exclusion of this perhaps anomalous wave disturbance from the five wave composite, suggests that precipitation falling in wave categories 5 - 7 account for only 10 - 15 percent of the total precipitation of the wave composite. These precipitation estimates cover only a small portion of the composite wave in the north - south direction, but it is assumed that they are fairly representative of the entire north - south extent of the waves. This assumption seems to be reasonable since the estimates encompassed the portion of the wave in which the maximum precipitation amounts typically occurred. There were a number of precipitation events north of  $10^{\circ}\text{N}$ , but these events appeared to be a result of north - south variability in the wave track rather than the result of another type of feature.

### *2.2.2 Features in the monsoon trough zone*

The preferred region of the wave where the monsoon trough bands and the squall-lines typically formed was in wave categories 2 - 4 and south of the track followed by the disturbances centers. As can be seen in Figs. 2 and 5, this region of the wave was characterized by strong low-level convergence and positive vorticity. It was noted earlier in section 2.1 that the area of strong convergence and positive vorticity was tilted from northeast to southwest because of the interaction between the low-level northerly flow in the wave and the southwesterly monsoon flow.

### *Monsoon trough bands*

In each wave during Phase III, a large band of active convection (monsoon trough band) typically formed in the southern part of the GATE A/B-scale ship array just after the ridge passed. A good example of a monsoon trough band is located between the arrows in Fig. 8 a - b for 1200 and 1800 GMT 4 September (wave 2), respectively. Figure 8 also shows the corresponding streamline analyses in the region of the band at the surface and 700 mb. As shown in Fig. 8, the bands were typically about 70 km wide and between 400 and 650 km long. However, satellite images indicated that the bands often extended beyond the view of the radars and had lengths between 600 and 800 km. The position and orientation of the bands were coincident with the monsoon trough convergence in this region of the wave. The centroid of the large-scale bands usually moved from east to west, at an angle between  $60^\circ$  and  $90^\circ$  to their orientation, at speeds close to that of the wave trough ( $7 - 8 \text{ m s}^{-1}$ ). This behavior can be seen in Table 3, which summarizes the characteristics of the monsoon trough bands for each wave from the merged radar maps. (The peak rainfall rates were computed using the rainfall - reflectivity relationship  $Z = 180 R^{1.35}$  that was proposed by Austin and Geotis (1979). This relationship was also used for Tables 4 and 5.) However, some of the bands appeared to be stationary during part of the 24 - 36 h period they were visible from the radars and/or satellite. For example, the monsoon trough bands in waves 1 and 5 moved very little until the wave trough was about 300 km east of the ship array. As these two troughs crossed the array, the bands started moving from east to west through the ship array at approximately the same speed as the troughs.

### *Squall lines*

In two of the waves during Phase III (2 and 4), a total of three squall lines were observed in the same region of the waves where the monsoon trough bands typically occurred. Over Africa, Payne and McGarry (1977) pointed out that, in general, the occurrence of squall lines was most prevalent in the region approximately one-fourth of a wavelength downstream of the wave trough (categories 2 and 3). These squall lines typically moved at a mean speed of  $16 \text{ m s}^{-1}$  to the west (roughly twice the average speed of the waves) and subsequently dissipated just east of the wave ridge. The three squall lines observed over the ocean crossed the ship array just upstream of the wave ridge (category 1) and were probably in a mature stage of development. The squall lines normally exhibit the most pronounced line organization and produce the largest amount of precipitation in the mature stage.

The three squall events are indicated by arrows on the time - latitude precipitation map in Fig. 6. Table 4 summarizes the properties of the three squall lines as observed by the radars and Fig. 9 a - b shows the first squall line at 1200 and 1800 GMT 4 September (wave 2) together with the corresponding streamline analyses at the surface and 700 mb. This particular squall line has been well documented by Houze (1977).

As can be seen in Table 4, the three squall lines were very similar in size, orientation, and movement. Each squall line was composed of an arc of deep convection with a radius of 150 km followed by a larger area of weaker stratiform precipitation. As illustrated in Fig. 9, the squall lines were typically oriented roughly perpendicular to the monsoon trough band and moved perpendicular to their orientation, from northeast to southwest, along the axis of the monsoon

trough. The most vigorous convection in the squall line was centered on the trough axis (Houze, 1977; Zipser, 1977). Behind the squall lines, the convergence band was shifted towards the northerly flow by the wake of outflow air behind the squall line. The wake structure has been described by Zipser (1969, 1977) and Houze (1977).

#### *Characteristics of the line structure*

Leary and Houze (1979) and Houze (1977) have described the three-dimensional structure and life-cycle of a squall line and a number of lines within a single cloud cluster observed during Phase III. One of their most significant findings was that the three-dimensional structure and morphology of these features was very similar, even though they were very different in terms of development, speed of movement, and orientation with respect to the monsoon trough. In an effort to expand and generalize their results, the three-dimensional structure and morphology of the mesoscale features in the monsoon trough region (monsoon trough bands and squall lines) of all the waves were examined. To do this, time sequences of three-dimensional radar maps were constructed using the polar radar data sets from the four C-band radars. As can be seen in Figs. 8 and 9, each of these larger scale line systems was typically composed of a number of mesoscale *line elements*, 20 - 30 km wide and 70 - 100 km long, that moved parallel to the motion of the large-scale line system. The line elements had a structure similar to, and evolved in a manner close to, those discussed by Leary and Houze (1979). These line elements contained a number of convective *cores* or regions of high reflectivity which tended to move parallel to the motion of the line. Figure 10 a - b shows examples of the

vertical structure of the cores in the monsoon trough band and squall line that were presented in Fig. 9 a. The cross-sections were made using the *Oceanographer* polar radar data, and represent vertical slices along the lines in Fig. 9 a, each 12 km high and 128 km long. As can be seen in Fig. 10, these cores were characterized by steep horizontal gradients of reflectivity and small vertical gradients. In this example, the tops of the higher cores extended above the vertical extent of the cross-sections. However, other cross-sections, made with larger vertical extents showed that the tops of the highest cores typically reached 12 - 13 km, and one core in the 4 September squall line reached 17 km (see for example Fig. 19 in Houze, 1977). Tables 3 and 4 show that the cores in these deep convective lines within the monsoon trough region typically had peak rainfall rates greater than or equal to  $50 \text{ mm h}^{-1}$  and their tops typically reached 12 - 13 km.

### 2.2.3 Features north of the monsoon trough region

In each wave there were one or more long thin lines of precipitating convection which formed north of the mean disturbance path in the wave categories 8 and 1 (in and just east of the ridge). As can be seen in Figs. 1 and II, which depict the horizontal and vertical structure of the wave in this region, the midtropospheric easterly jet in these categories of the wave achieved its highest wind speed and maximum southerly extent, to the vicinity of the reference latitude (about  $12^{\circ}\text{N}$ ). In the vertical, the jet was positioned at about 600 mb along the boundary of a layer of hot, dry midtropospheric air to the north and a deep layer of cooler moist midtropospheric air to the south. The hot, dry midtropospheric air was normally laden with

dust and usually could be traced backward to an origin over the southern fringe of the Sahara. Carlson and Prospero (1972) have labelled this air mass the Saharan Air Layer (SAL). In the vicinity of the jet there were regions of strong vertical and horizontal wind shear, on the order of  $10^{-2}$  and  $10^{-5} \text{ s}^{-1}$ , respectively. The north - south temperature gradient at 800 mb in the same region was about  $1 \text{ K (100 km)}^{-1}$ , slightly larger than that needed for thermal wind balance.

The long thin cloud lines typically formed just west of the African coast (in wave categories 8 and 1), but north of the region covered by the merged radar maps. Consequently, no detailed account of their structure at the time of development can be given. Once formed, however, they moved slowly toward the south - southwest into the region covered by the radars with the speed and direction of the lower-tropospheric flow. By the time the convective lines reached the area covered by the radars, they were just west of the wave trough in wave categories 2 and 3. This difference occurred primarily because the mean east - west speed of the flow in the lower troposphere ( $3 - 4 \text{ m s}^{-1}$ ) where the lines were observed, was slower than the speed of the wave ( $7 - 8 \text{ m s}^{-1}$ ) toward the west; therefore, the wave troughs were slowly overtaking the cloud lines from the east.

While the lines were north of the region covered by the radars, the characteristics of the lines were determined by satellite images. Figure 12 a - b shows one of the longest and most clearly identifiable of the narrow convective lines at 0300 and 0600 GMT on 5 September (wave 2), while Fig. 13 shows the same line as viewed by satellite and radar at 0900 GMT 5 September. The corresponding streamline analyses at the surface and 700 mb are also shown in Figs. 12 and 13 b. Table 5 summarizes the characteristics of these lines as determined from both the satellite images and the merged radar maps. In Table 5, two peak rainfall rates and

two maximum echo heights are given for each wave. The first of these numbers corresponds to the period before the convective lines entered the monsoon trough region, and the second value to the period after the lines entered the trough zone. As can be seen in Table 5, the lines were typically 400 - 1000 km long and 25 - 35 km wide. They were usually oriented east-west and their centers moved toward the south - southwest, at 4 - 6 m s<sup>-1</sup>. The speed of the line was very close to the mean speed of the synoptic-scale northerly flow in the lower troposphere for the wave categories west of the wave trough (1 - 3). In a few waves, more than one line was observed. An example of this can be seen in Fig. 14, which shows a visible satellite image at 1000 GMT 2 September (wave 1). Three of the five lines observed for this wave were visible in the satellite image. The spacing between the lines, in this wave and the other two waves in which more than one line was observed, was between 90 and 120 km. The long convective lines typically were visible by satellite and/or radar for 18 - 24 h. The line in wave 2, shown in Figs. 12 and 13, was tracked for 40 h. The early growth and maintenance of this line will be discussed in detail in the following sections.

The long narrow lines also had a similar three-dimensional structure and morphology to that described previously for the features in the monsoon trough region, and to those lines discussed by Leary and Houze (1979), even though the long narrow lines originated in a much different environment. The three-dimensional structure of the line in Fig. 12 at 0315 and 0601 GMT 5 September is shown in Fig. 15. Figures 15 a and 15 c are stacks of X - Y planes, 256 km on a side, showing the radar reflectivity distribution at different heights for the area outlined in Figs. 12 a and 12 b, respectively. Figures 15 b and 15 d are Y - Z cross-sections, 12 km high and 256 km long, for the vertical plane along the dashed lines shown in Figs. 15 a and

15 c. As can be seen in Fig. 15, the line elements in the long narrow lines were approximately 70 km in length. The average lifetime of the line elements in the narrow lines was only slightly shorter than that observed for the squall lines and monsoon trough bands in the monsoon trough region. The line elements in the squall lines and monsoon trough bands had an average lifetime of about 90 min, while those in the narrow lines typically lasted only about 60 min.

Comparison of Tables 3, 4, and 5, and Figs. 10 and 15 reveal that the cores in the narrow lines of convection had lower peak rainfall rates and tops than the squall lines and the monsoon trough bands: 25 - 30 mm h<sup>-1</sup> and 4 - 5 km, compared to 50 - 60 mm h<sup>-1</sup> and 12 - 13 km. The portions of the narrow lines in wave category 3, just to the west of the trough, had dramatically higher peak core rainfall rates and echo tops (40 - 45 mm h<sup>-1</sup> and 10 - 13 km) than the portions of the narrow lines in wave categories 1 and 2. This transition can be seen in the time sequence for the 5 September line (Figs. 15 a and 15 c). At 0600 GMT, the cores in the eastern end of the line became much more intense, the echo tops increased from about 5 km to 12 - 13 km and the peak reflectivities (and rainfall rates) increased from 38 - 40 dBZ (25 - 30 mm h<sup>-1</sup>) to 45 - 47 dBZ (40 - 45 mm h<sup>-1</sup>). The rapid vertical growth and intensification of the convection occurred at the time that the wave trough was overtaking the eastern end of the cloud line.

### 2.3 Role of African waves in organizing mesoscale features during GATE

The description in the previous section of the organization of precipitating convection within the context of the synoptic-scale waves has pointed out the strong influence that the waves had, not only on the precipitation amount, but also on the type of mesoscale organization. The

waves had an obvious influence on the determination of the position of the low-level convergence in the monsoon trough region, and the degree of mesoscale organization of the deep convection appeared to be very sensitive to these changes in low-level convergence. Both the monsoon trough band and the squall lines had their most vigorous convection in the region of maximum low-level moisture convergence along the monsoon trough. The monsoon trough bands formed as the northerly flow increased after the passage of the wave ridge and dissipated in the region of the wave where there was cross-equatorial southerly flow after the trough passage. The interaction of the wave circulation with the monsoon flow, provided a preferred region of low-level convergence where the monsoon trough bands formed. Very little is known, however, about why the convection was organized on the mesoscale in the convergence zone.

As pointed out by Aspliden *et al.* (1976) and Payne and McGarry (1977), the squall lines generally formed over the land in the same region of the wave as the monsoon trough bands (wave categories 2 and 3), and propagated at 2 - 3 times the wave speed toward the ridge where they dissipated. The three squall lines observed in the ship array appeared to form over the land near the coast and propagate to the west over the ocean along the monsoon trough. This suggests that the oceanic squall lines were closely related to the disturbance lines over Africa, which were first described by Hamilton and Archbold (1945) and Eldridge (1957). As the squall lines propagated over the ocean, they appeared to be maintained by the low-level convergence in the monsoon trough zone.

The long narrow lines originated as a result of a completely different mechanism from the lines in the monsoon trough zone. The narrow lines typically formed in a region of the wave with little low-level moisture convergence, where the air had recently crossed the desert. As can

be seen in Fig. 19 a-c (and as described in detail in the next section), these lines normally appeared at the leading edge of large dust plumes that originated over Africa. These large dust plumes, described in detail by Carlson and Prospero (1972), Karyampudi (1979), and Carlson (1979), move largely toward the west, but reach their southernmost latitudes in the wave ridge. The dust, which was recognizable on the satellite images, acted as a tracer for the hot, dry air that had recently been over the desert (the SAL). The SAL was typically about 4 - 5 K warmer and much drier than the air over the ocean that did not traverse the desert region. As can be seen in Fig. 11, there was a strong baroclinic zone in wave category 8 along the southern boundary of the SAL, where the SAL air was adjacent to the relatively cool, moist, air near the monsoon trough. This baroclinity was also observed in the wave category just east of the ridge (category 1). As a result of the north - south baroclinity along the boundary of the SAL, there was a strong mid-level easterly jet with maximum speeds at the top of the baroclinic zone, typically 650 mb (Karyampudi, 1979). The narrow lines formed along the lower tropospheric shear (or thermal wind) in the region of the baroclinic zone at the southern edge of the SAL. Unlike the squall lines which propagated with respect to the wave, the lines along the SAL moved toward the south - southwest with the spreading dust plume and jet, at a speed very near the mean northerly flow in the lower troposphere east of the wave ridge. The close association of the lower tropospheric baroclinic zone and the easterly jet with the development and structure of these lines suggests that the narrow lines formed as a result of some hydrodynamic instability within the wave circulation that preferentially occurred in and just east of the wave ridge. Symmetric inertial instability of the easterly jet in the wave ridge would result in circulations parallel to the shear that could act to organize the narrow convective lines. Hoskins (1974) and

Emanuel (1978) have shown that negative potential vorticity is the condition required for symmetric inertial instability of a flow with horizontal and vertical density gradients.

As a preliminary means of investigating this possibility, Fig. 16 a shows the analyses of potential vorticity on the 310 K isentropic surface, where the potential vorticity is defined as in (3.4) divided by  $g$  (see the discussion in the next chapter). These calculations were based on Reed's composite wave analyses. Figure 16 b shows the cross-section of potential vorticity for the wave category 8, the same category used in the cross-sections of wind and potential temperature in Fig. 11. Comparison of Figs. 7, 11, and 16, indicates that the long narrow lines originated in a region of low potential vorticity at the leading edge of the SAL and parallel to the midtropospheric jet. Reed's composite analyses are averaged for 300 km in the east - west direction and 450 km in the north - south direction and are only useful for identifying features with a horizontal scale of at least 600 km. However, observations of the baroclinic zone along the edge of the SAL, from the few aircraft missions made before GATE, indicate that the changes in this zone occur over a much smaller scale, on the order of 100 km. This suggests that the magnitude of the potential vorticity near the wave ridge may have been closer to zero on a smaller scale. Given the typical vertical wind shear, on the order of  $10^{-3} \text{ s}^{-1}$ , in the region of the jet reported by many investigators (e.g. Burpee, 1972, Reed *et al.*, 1977, and Mass, 1979) a thermal gradient only slightly larger than that for thermal wind balance would be necessary for the values of potential vorticity to be negative. If negative potential vorticity actually occurs on scales smaller than those that can be resolved with the composite analysis, then symmetric inertial instability may account for the generation of these lines.

In the next section a detailed analyses of one narrow convective line will be described

with the aim of verifying this hypothesis. Because these narrow convective lines formed outside the GATE A/B-scale ship array and moved into it, there is little data available in the area where the lines originate, opening the possibilities for physical mechanisms that might produce these lines.

### **3. Case study of lines that form north of the monsoon trough**

To investigate the possibility that symmetric inertial instability played a role in organizing and maintaining the lines that form north of the monsoon trough zone, one case was considered in detail. The line observed on 5 September, shown in Figs. 12 and 13, was selected as an exceptionally clear example of those that affected the GATE ship array. The interaction of this line with other mesoscale features in the monsoon trough region has been studied in detail by Leary (1979) and Leary and Houze (1979). They emphasized the role the deep convection played in the changes in mesoscale structure within the monsoon trough zone. In this study the emphasis is on the origin and development of the convective line before it entered the monsoon trough zone.

#### **3.1 Development and movement of the narrow convective line**

The convective line developed off the west coast of Africa near 15°N northeast of the area covered by the GATE ship array. Visible satellite images were used to determine the structure and movement of the cloud line in the region of development and in the intervening area as the line moved toward the ship array (1800 GMT 3 September - 1800 GMT 4 September). Only these images were used to track the convective line movement because it was too shallow to be visible on the infrared (IR) satellite images until the line reached the monsoon trough zone. The IR images, which were taken every hour throughout the day and night, were useful in detecting very high, cold cloud tops, like those produced by deep convective clouds. Unfortunately, the

visible satellite images are available only during the daylight hours, and the position of the convective line during the nighttime hours was determined by extrapolating between the last visible satellite image on one day (typically 1900 GMT) and the first visible image the next day (typically 0800 GMT). Isochrones of line position from the visible satellite images are shown in Fig. 17.

### *3.1.1 Synoptic-scale features*

Synoptic-scale analyses on constant-pressure surfaces at 6-h intervals, such as those shown in Fig. 18 a - h, were used to depict the evolution of the large-scale environment during the period of convective line development. These analyses were constructed from rawinsonde and pilot balloon observations for the stations over west Africa, combined with the rawinsonde data from the ship array and aircraft dropwindsonde data. The positions, and station codes or names of the land and ship stations used in the analyses are shown in Fig. 4. The observations were taken from the GATE processed and validated data sets produced by the Synoptic and Convection Subprogram Data Centers. Any suspicious observations flagged by the data centers were deleted.

During the evolution of the narrow convective line, the large-scale atmospheric structure in the lower troposphere was dominated by the passage of the ridge of an African wave (Fig. 18 a - h). The structure of this wave was very similar to that of the composite wave described in the previous section. The surface circulation west of the ridge, as depicted by the heavy arrows in Fig. 18 a - c, was from the south, extending to almost 12°N at 1200 and 1800 GMT 3

September. In the wave categories east of the ridge the surface flow became more northerly, the maximum northerly flow occurring in wave category 2 at  $10^{\circ}\text{N}$  (Fig. 18 e - h). However, the wind remained southerly on the east side of the ridge over the land and portions of the ocean near the coast because of the southwest - northeast tilt of the monsoon trough at the surface. As illustrated in Fig. 18 a - h, this southerly flow extended from near the equator to about  $12^{\circ}\text{N}$ .

At 700 mb, the ridge (category 8) crossed the coast at 1200 GMT 3 September (Fig. 18 a). During the period of the line development (1800 GMT 3 September - 0600 GMT 4 September), the ridge propagated toward the west at about  $8\text{ m s}^{-1}$ , crossing the ship array between 0000 and 0600 GMT 4 September (Fig. 18 a - d). In the same period, a trough (category 4), originally positioned near  $6^{\circ}\text{W}$  at 0000 GMT 4 September (Fig. 18 c), propagated toward the west at about  $7\text{ m s}^{-1}$ . The mean position of the easterly jet was about  $16^{\circ}\text{N}$ , and it was positioned farthest to the south in and just east of the wave ridge. As illustrated in Fig. 18 e, the jet moved as far south as  $13^{\circ}\text{N}$  in the vicinity of the ship array.

The most striking feature of the synoptic-scale circulation was the the structure of the easterly jet at 700 mb. Throughout the period of analysis, the jet was typically composed of one or more maxima or *streaks*, an example of which can be seen in Fig. 18 a. At this time, the easterly jet, defined by wind velocities greater than  $15\text{ m s}^{-1}$ , was composed of two maxima. One jet streak was positioned west of the ridge near  $17^{\circ}\text{N}$ ,  $25^{\circ}\text{W}$ , and had a maximum velocity exceeding  $20\text{ m s}^{-1}$ . The second jet streak, with a maximum velocity of  $19\text{ m s}^{-1}$ , was positioned farther south, near  $13^{\circ}\text{N}$ ,  $14^{\circ}\text{W}$ , and east of the wave ridge. During the period of analysis, four jet streaks were observed. Beside the two jet streaks pointed out in Fig. 18 a, a third jet streak was located near  $14^{\circ}\text{N}$ , just east of the ridge in Fig. 18 b - g, and the fourth was near the wave

trough in Fig. 18 e-h. All four jet streaks were similar in intensity and movement. Their maximum velocity was typically  $19\text{-}25\text{ m s}^{-1}$ , and they all propagated toward the west, faster than the wave, at a mean speed of  $14\text{ m s}^{-1}$ . However, their position within the wave varied considerably, from near the trough to near the ridge.

The jet maximum east of the ridge, near  $14^{\circ}\text{N}$ , was associated with a dust plume that emerged from the Sahara, and crossed the coast of Africa between 1200 and 1800 GMT 3 September (Fig. 18 a - b). This dust plume was apparent as a smudge just northwest of Dakar in the visible satellite images at 1200 and 1800 GMT 3 September shown in Fig. 19 a - b. The position and intensity of this jet streak, along the southern boundary of the dust, agrees with those found by Karyampudi (1979) in a study of the SAL during GATE. He pointed out that the jet maximum usually occurred in wave category 1 just east of the wave ridge where the SAL was farthest south. The strongest lower-tropospheric baroclinity usually occurred along the southern boundary of the SAL in this region. Karyampudi (1979) also showed that often more than one jet maxima occurred within the wave, and that even though the jet maximum in his composite wave structure occurred in category 1, this maximum spread across the ridge (wave categories 5 - 1). He suggested that this broad maximum was caused by variations in jet streak position in the waves used to make the composite. Also, variations in the SAL structure on scales smaller than could be resolved by the existing data often resulted in more than one jet streak accompanying a major dust outbreak. Examination of the visible satellite images from early in the day on 3 September (not shown) indicated that the latter was the case for the existence of the jet streak west of the ridge. This jet streak was near the boundary of another dust plume that had crossed the African coast during the night on 2 September. Examination of

the satellite images also indicated that the jet maximum near 13°N, 14°W in Fig. 18 a-b, and that near the wave trough in Fig. 18 e-h were never associated with a dust outbreak. Of these two, the jet streak in the ridge was very weak, lasting only about 12 h, indicating it was most likely associated with a more transient feature than a major dust outbreak.

As can be seen in Figs. 18 and 19, only three of the jet streaks were associated with long narrow lines of clouds. However, two of the cloud lines were relatively short-lived, lasting 12-18 h. One of the short-lived cloud lines was located in the entrance region of the jet streak west of the ridge at 1200 GMT 3 September. This cloud line extended east-west from the Cape Verde Islands to within 270 km of the African coast (Fig. 19 a). Between 1200 and 1800 GMT, the cloud line drifted toward the south at  $5 \text{ m s}^{-1}$ , and by 1800 GMT, the eastern end of the line extended to about 19°W, 250 km from the coast. Comparison of Fig. 19 b and 19 c indicated that during the early morning of 4 September this cloud line dissipated while another cloud line formed in the exit region of the northernmost jet streak east of the ridge. The second short-lived convective line formed in the exit region of the southernmost jet streak in Figs. 18 a-b and 19 a-b. This cloud line was observed only in the last visible satellite image on 3 September (Fig. 19 b), and had dissipated by the first visible image on 4 September (Fig. 19 c).

During, and just after the time period that the short-lived cloud lines were dissipating, a long-lived convective line formed in the entrance region of the northernmost jet streak east of the ridge around 0000 GMT 4 September. At 1800 GMT 3 September, the dust plume associated with this jet streak had a very sharp southern boundary which appeared to connect to the eastern end of the cloud line associated with the jet streak west of the ridge (Fig. 19 b). In the period between the last visible satellite image on 3 September (Fig. 19 b) and the first

visible image on 4 September (Fig. 19 c), the long-lived convective line formed along this boundary of the dusty air between the coast and the eastern end of the preexistent cloud line. Extrapolation of the line position from the visible satellite images indicated that the narrow line developed north of the exit region of the jet streak, east of the ridge, as the ridge crossed the coast. The air parcels crossing the coast north of the jet streak were very dry. Therefore, the circulation associated with the convective line formation was probably not visible until enough moisture was available to form clouds. Hence, the mechanism that caused the convective line development probably required no latent heat release as a source of energy.

As shown in Figs. 18 c - e and 19 c, the narrow cloud line remained north of the jet streak east of the ridge throughout the first half of 4 September, while the short-lived cloud line west of the ridge decayed as the jet streak west of the ridge moved farther west. During this time period, the northernmost jet streak east of the ridge advected toward the west at about  $15 \text{ m s}^{-1}$  and toward the south at about  $5 \text{ m s}^{-1}$ , approximately the speed of the northerly flow in the lower troposphere (900 - 800 mb). The western edge of the long-lived cloud line also propagated toward the west at the same speed as the jet streak, while the whole line drifted toward the south at about  $5 \text{ m s}^{-1}$ . The wave trough was also moving toward the west at a mean speed of about  $7 \text{ m s}^{-1}$ . However, the east - west speed of the flow in the lower troposphere was only  $3 - 4 \text{ m s}^{-1}$ , therefore, the wave trough was slowly overtaking the cloud line from the east. The eastern end of the line was originally between wave categories 8 and 1 at 1800 GMT on 3 September, but by 1200 GMT on 4 September, the eastern end of the line was in wave category 2.

In the period 1200 - 1800 GMT 4 September, the eastern end of the convective line

crossed the jet maxima, moving from the anticyclonic shear side to the cyclonic shear side of the jet (Fig. 18 e - f). The western end of the line appeared to stay on the anticyclonic shear side of the jet maxima as it propagated toward the west. When the eastern end of the narrow cloud line propagated into the ship array, it entered a region of increasing cyclonic shear and low-level convergence on the west side of the wave trough (Fig. 18 f - h). By the time of the first visible satellite image at 0900 GMT 5 September, the eastern end of the cloud line had merged with the monsoon trough cloudiness, while the western end of the line extended over 1000 km to the northwest (Fig. 13 a). As illustrated in Fig. 18 h, by 0600 GMT on 5 September the eastern jet streak had propagated beyond 27°W, and only the extreme western portion of the cloud line was north of the jet streak position. It should be noted that the western end of this narrow line continued across the Atlantic and was tracked using visible satellite images for over 40 h (see Fig. 17).

The principal differences between the jet streak that was associated with the long-lived convective line and the other three jet streaks were, the position of the jet streak in the wave, and its proximity to the SAL boundary. One of the jet maxima associated with a short-lived cloud line was positioned just east of the wave ridge, but south of the SAL boundary. Whereas, the other two jet maxima were positioned farther north near the SAL boundary, but not in the wave ridge where the SAL boundary is typically the strongest (Karyampudi, 1979). The jet maxima west of the ridge, where the SAL was relatively strong, was associated with a short-lived cloud line, but the jet maxima near the trough (Fig. 18 e-h) was not associated with any lines. These observations suggest that the important synoptic - scale ingredients in the development of the long-lived narrow cloud line were the position of the line near a jet streak in

or just east of the wave ridge along the southern boundary of the SAL.

### *3.1.2 Convective structure*

During the period that the convective line was developing, it was outside the region covered by the shipborne radars. Consequently, the convective structure of the line in this region was inferred from the high resolution visible satellite images. The most striking feature of the convective line during the first 24 h after it formed was its sharpness in the satellite images. As can be seen in Fig. 19 d, the line reached a length of over 1500 km by 1800 GMT on 4 September, yet it had a width of just 25 - 30 km. In an independent study based on the visible satellite images, Adamski (1979) also examined the long cloud line on this date. He showed that during the first 24 h after the line developed, there was little change in structure and movement of the line, which was characterized by shallow convection with maximum tops around 3 - 4 km. As the narrow convective line drifted toward the south it became longer but the width and height of the convective elements in the line remained nearly constant.

After the line entered the ship array (from 2100 GMT 4 September - 1200 GMT 5 September) the merged radar maps were used to track the movement of the line and to determine any changes in line structure in the region covered by the radars. By this time, the convective line had crossed to the south side of the axis of the jet streak into the region of increasing cyclonic shear. Figure 20 shows isochrones of line position from the merged radar maps.

While the convective line was in the region covered by the radars, its three-dimensional

structure and evolution was obtained from the radar data. Figure 15 a - d shows the three-dimensional structure of the line at 0315 and 0601 GMT 5 September from the *Gilliss* radar. At 0315 GMT the cores in the line were still very low, about 4 - 6 km, but in the next 3 h the structure of the line and the intensity of the cores changed dramatically. By 0600 GMT 5 September the line was half way between the *Vanguard* and the *Gilliss*. As shown in Figs. 12 b and 15 c - d, it had widened to almost 35 km and the tops and intensity of the cores had increased, to 12 - 13 km and 45 dBZ, respectively. During the period 0300 - 0600 GMT, the eastern end of the cloud line moved toward the south faster than the western end of the line, 6 - 7 m s<sup>-1</sup> as opposed to 4 - 5 m s<sup>-1</sup>. The eastern end of the line was moving in discrete steps, i.e. new line elements developed ahead of the line, moved more slowly than the line, and eventually merged into the line. This type of growth has been documented by Leary and Houze (1979), and appears to be typical of not only the long narrow lines, but also most of the mesoscale line systems in GATE. As an example of this type of process, Fig. 15 d, shows three distinct cores in the line. The one farthest to the south had recently developed, while the other two cores were successively older cores that had already been incorporated into the line. This type of convective cell growth relative to the line continued throughout the time that the line was in range of the radar. The increase in width, strength, and height of the cores probably reflected an increase in the low-level moisture supply and surface convergence as the line neared the monsoon trough.

Leary (1979) and Leary and Houze (1979) have given a detailed account of the evolution of the line (line N1 in their study) after this time and its interaction with the other convective features. Both Adamski (1979) and Leary (1979) pointed out that passage of the leading edge of the convective line at the surface was characterized by cyclonic vorticity and convergence.

Furthermore, the surface observations behind the line also indicated that the temperature dropped slightly and the dewpoint and pressure went up. Also, Prospero *et al.* (1976) have shown that the *Gilliss* recorded one of the highest dust catches during Phase III shortly after the line passed.

Besides the long narrow cloud line, two other large mesoscale features were observed during the period of interest. At 0600 GMT 4 September, the monsoon trough band shown in Fig. 8 developed in the southern part of the ship array as the easternmost wave trough progressed toward the west and the ridge moved past the ship array. Early in the day on 4 September another interesting mesoscale feature, the squall line shown in Fig. 9 propagated toward the west, crossing the west coast of Africa at 0000 GMT 4 September. The squall line propagated toward the southwest along the monsoon trough band and crossed the ship array between 1200 GMT 4 September and 0000 GMT 5 September (Fig. 18 c - g). As a point of interest, it was apparent during the analysis of the 6 - h constant pressure maps that the squall line originated just south of the northernmost jet streak east of the ridge as the jet streak approached the west coast of Africa (Fig. 18 b). The squall line then propagated toward the southwest at the same speed as the jet streak until the squall line weakened. From the limited data available over Africa, it seems that the development of the squall line and the jet streak east of the ridge were related.

### *3.1.3 Vertical atmospheric structure near the convective line*

As noted in the previous section, the convective line had a typical width of only 25 - 30 km, even though it was synoptic-scale in length. Unfortunately, no aircraft data were available from the immediate vicinity of the cloud line until after it was in the wave trough region where interactions of the line with other convective systems had already occurred. Thus the mesoscale kinematic and thermodynamic structure perpendicular to the cloud line had to be inferred from the available 6-hourly upper air data. However, the mean spacing between the upper air stations was about 300 km, and in the region where the cloud line formed, there were no stations at all. Therefore, the vertical structure of the lower troposphere in the vicinity of the cloud line was obtained from north - south cross - sections of wind and thermodynamic variables along longitudes 16°W and 23.5°W, taking advantage of the north-south alignment and close proximity of the stations along these longitudes. The position of the two cross - sections with respect to the cloud line are illustrated in Fig. 18 c and 18 e. The cross-section at 0000 GMT 4 September (Fig. 21 a) was constructed primarily from land stations along the west coast of Africa at the time that the narrow convective line formed. The cross-section at 1200 GMT 4 September (Fig. 21 b) was constructed from ship and island rawinsonde data combined with one aircraft dropwinsonde just prior to the time that the cloud line crossed the axis of the jet streak from the negative to the positive shear side.

The thermodynamic data taken by the Soviet ships had to be corrected before they could be used in the cross-section analyses because of the large temperature biases in these soundings reported by Reeves (1978). The correction used in this study was a slight modification of that

suggested by Reeves and Esbensen (1977). The nighttime temperatures were averaged for each Soviet ship for all of Phase III. Then these phase means were compared to the phase means for the four B-scale ships recommended as a standard (*Researcher, Dallas, Quadra, and Oceanographer*). The temperature corrections applied to the Soviet soundings were derived from the difference in the phase mean temperatures between the Soviet ships and the standard, minus the temperature difference due to the thermal wind, calculated from the mean wind change with height from adjacent ships. The relative humidity from the uncorrected soundings was used with the corrected temperatures to determine a corrected humidity. The corrected height fields were then computed from the integral of the hydrostatic equation where the virtual temperature was calculated from the corrected temperatures and humidities.

In the lower troposphere below 600 mb, the potential temperature cross-sections illustrated in Fig. 21 indicated that the line was located along the boundary of hot air to the north and cooler air to the south. The potential temperature in the hot air was 313 - 314 K and the static stability was relatively low, about  $3 \times 10^{-3} \text{ K m}^{-1}$ . The mixing ratio (not shown) was very low in the high potential temperature air mass, with typical values of 2 - 3  $\text{g kg}^{-1}$ . These values of potential temperature and mixing ratio are characteristic of the SAL (Carlson and Prospero, 1972). The typical potential temperature and mixing ratio changes on a constant pressure surface across the region of the line were 2.0 - 2.6  $\text{K (100 km)}^{-1}$  and 3 - 4  $\text{g kg}^{-1} (100 \text{ km})^{-1}$ , respectively. The top of the hot - dry air mass (SAL), as depicted in Fig. 20, was about 650 mb. Over land the base of the SAL extended to the surface, while over the ocean it was between 850 - 900 mb.

In both cross - sections of the zonal wind component, the narrow convective line was positioned just north of the midtropospheric easterly jet along the southern boundary of the SAL.

As would be expected from the thermal wind relationship, the jet had a maximum easterly component of about  $20 - 25 \text{ m s}^{-1}$  at 650 mb near the top of the SAL. The vertical shear in the region just below the jet was negative and about  $6 - 7 \times 10^{-3} \text{ s}^{-1}$  (negative shear to the south), approximately one quarter of that required by the thermal wind relationship to balance the strong horizontal temperature gradient. The strong vertical shear is also indicative of a very low Richardson number in the lower troposphere (0.4 - 0.5). The horizontal shear along an isentropic surface in the vicinity of the convective line was negative and about  $3.0 - 4.0 \times 10^{-5} \text{ s}^{-1}$ , equal to or slightly greater than the value for the vertical component of the Coriolis force at that latitude. Therefore, the absolute vorticity along an isentropic surface in this region was near zero or slightly negative. When the jet streak was over the west coast of Africa, the lowest absolute vorticity along an isentropic surface was near 700 mb (Fig. 21 a). However, when the jet streak was over the ocean the lowest absolute vorticity along an isentropic surface was along the southern boundary of the SAL, extending from 700 mb to near 900 mb (Fig. 21 b).

### 3.2 Kinematic fields in the vicinity of the convective line

To aid in the determination of the mechanism or mechanisms resulting in the formation and maintenance of the narrow convective line, the relative vorticity, divergence, and resultant deformation were calculated for the 6-h constant pressure analyses. The technique outlined originally by Bellamy (1949) was used to compute the kinematic quantities over triangular areas. Bellamy (1949) developed a method of estimating divergence via a line integral technique. From a specialization of Stoke's Theorem, the horizontal divergence can be computed by integration of

the component of the wind normal to a closed curve bounding a specified area. For the curve, Bellamy (1949) selected a triangle with vertices at the wind observation points. The triangle produces the smallest scale and the least areal - smoothed information, since a minimum of only three points is required to define an enclosed area. The wind observations are treated as estimates of the displacement of the vertices of the triangle in a unit time. An estimate of the divergence is directly obtained, since the divergence is equal to the percentage increase in area enclosed by the curve per unit time. The major assumption in this method is that the wind varies linearly along each leg of the triangle. The vertical component of vorticity and resultant deformation can be similarly determined using the same line integral approach, since suitable rotation of the original wind vectors produce wind fields with vorticity and deformation that can be computed in an identical manner to the divergence of the original wind field (Saucier, 1955 p. 339 and p. 360). It should be pointed out that the limit in the defining equation implies that the computed divergence is the average value within the triangle and not a true point value. Therefore, a horizontal scale is attached to each estimate of divergence, which in this case is the average spacing between observations, about 300 - 400 km.

The information used to compute the kinematic fields was the 6 - h upperair observations used to construct the constant pressure analyses. Ooyama and Esbensen (1977) and Reeves (1978) have shown that there are often large errors in winds measured by the U.S. ships equipped with navaid wind systems (all U.S. ships excluding the *Vanquard*). Therefore, the wind measurements from these ships were avoided in the computation of the kinematic quantities. Using a procedure similar to that described by Ceselski and Sapp (1975), each wind observation was combined with the neighboring points to produce triangles for computation of the kinematic

quantities. Both theoretical and practical considerations limit the triangles for which kinematic computations can be made reliably, uniform triangle sizes producing the best results (Schaefer and Doswell, 1979). The ideal triangles are equilateral, because the evaluation of the line integral becomes unstable when the observations are unevenly distributed around the centroid of the closed curve. However, none of these requirements can be precisely specified when dealing with real data. Consequently, to minimize these problems, only triangles with internal angles greater than  $15^\circ$  were used in this study.

The relative vorticity and resultant deformation analyses for selected 700-mb maps shown in Fig. 18, are depicted in Fig. 22 a - j. Throughout the first 24 h of the convective line development (1200 GMT 3 September - 1200 GMT 4 September) the line was within a region of strong negative relative vorticity at 700 mb, on the order of  $3 - 4 \times 10^{-5} \text{ s}^{-1}$ , equal to or greater than the magnitude of the vertical component of the Coriolis parameter for these latitudes. Therefore, the vertical component of the absolute vorticity at 700 mb in this region, north of the jet, was near zero or slightly negative. Comparison of the cross-sections in Fig. 21 with the kinematic analyses in Fig. 22 c - d, indicated that the region of low absolute vorticity extended below 700 mb to near the base of SAL.

Also during this period, the line was in a region of relatively strong resultant deformation ( $1 - 4 \times 10^{-5} \text{ s}^{-1}$ ). However, the axis of dilatation was perpendicular to the line orientation, indicating that a frontogenetical mechanism was probably not responsible for the line formation. The divergence (not shown) was very noisy and positive for the triangles within the ridge.

During the 24-h period after the eastern end of the cloud line moved south of the jet streak, this portion of the convective line was in a region of increasing positive relative vorticity

and strong resultant deformation ( $1 - 2 \times 10^{-5} \text{ s}^{-1}$ ). However, unlike in the previous 24 h, the axis of dilatation was nearly parallel to the eastern end of the cloud line, indicating that the synoptic-scale deformation might have been acting as a frontogenetical mechanism, strengthening the temperature and humidity gradients across the SAL boundary in the vicinity of the convective line. Also, in the later 24-h period the synoptic-scale divergence was increasingly negative in the vicinity of the line.

### 3.3 Discussion of the formation and maintenance of the convective line

#### *3.3.1 Formation of the convective line*

In the last chapter it was pointed out that negative potential vorticity is a necessary condition for symmetric inertial instability in a fluid with horizontal and vertical density gradients, which is geostrophic and has equal diffusion of heat and momentum (e.g. Hoskins, 1974; Emanuel, 1978). To determine if symmetric inertial instability might have been responsible for the development of the line, a measure of the potential vorticity had to be estimated from the synoptic-scale analyses. In isentropic coordinates the potential vorticity,  $q$ , can be expressed as

$$q = \alpha \underline{\eta} \cdot \nabla \theta = \alpha \eta_k \partial \theta / \partial k \quad (3.1)$$

where  $\eta_k$  is the component of the absolute vorticity normal to the isentropic surface,  $k$  is distance in the direction of the potential temperature gradient, and  $\alpha$  is the specific volume (e.g.

Staley,1960).

By noting that  $\partial z / \partial k \approx 1$  if the isentropes are nearly horizontal, the component of the absolute vorticity in the k-direction,  $\eta_k$ , may be written to an excellent approximation in any of the following ways

$$\eta_k = \zeta_k + 2\Omega_k \approx \zeta_k + 2\Omega_z = \zeta_k + f \quad (3.2)$$

where  $\zeta_k$  is relative vorticity component normal to the isentropic surface,  $\Omega_k$  and  $\Omega_z$  are the components of the earth's vorticity normal to the isentropic surface and the earth's surface respectively, and  $f$  is the Coriolis parameter. Based on the previous assumption that the slope of the isentropes is small, the following approximation may be written with little error

$$\partial / \partial k \approx \partial / \partial z = -g\rho \partial / \partial p \quad (3.3)$$

Introduction of (3.2) and (3.3) into (3.1) yields

$$q \approx \alpha \partial \theta / \partial z (\zeta_k + f) = -g \partial \theta / \partial p (\zeta_k + f) \quad (3.4)$$

Since  $g$  is always positive and nearly constant in the troposphere, and the static stability is normally positive (i.e.  $\partial \theta / \partial z > 0$  or  $\partial \theta / \partial p < 0$ ), the necessary condition for negative potential vorticity is negative absolute vorticity along a potential temperature surface (i.e.  $\zeta_k + f < 0$ ).

As pointed out in the last section, the cross-sections in Fig. 21

indicated that there was a region of low absolute vorticity along an isentropic surface, and hence from (3.4) a region of low potential vorticity in the lower troposphere in a layer that extended roughly from 700 - 900 mb after the jet streak crossed the coast (Fig. 21 b). The convective line formed in the middle of this area of low potential vorticity in the lower troposphere. It is not surprising that the line was in a region of low potential vorticity in the lower troposphere, given the strong vertical wind shear along the line and the potential temperature difference observed across the line. Because of the nearly uniform wind conditions across the line, the strong vertical wind shear, and the potential temperature gradient north of and below the jet, the relative vorticity along the potential temperature surfaces was negative and equal to or greater than  $f$ . The static stability ( $\partial\theta/\partial z$ ) was positive in this region and as can be seen from (3.4), these conditions would make the potential vorticity ( $q$ ) near zero or slightly negative. An estimate of the magnitude of the negative potential vorticity can be made from (3.4) using the observations presented in the previous section. In the vicinity of the cloud line, the static stability ( $\partial\theta/\partial z$ ) was about  $3 \times 10^{-3} \text{ K m}^{-1}$ ,  $f = 3.5 \times 10^{-5} \text{ s}^{-1}$ , and the relative vorticity along the 315 K isentrope about  $-4 \times 10^{-5} \text{ s}^{-1}$ . Introduction of these values into (3.4) yields a potential vorticity of  $-1.5 \times 10^{-8} \text{ K m}^2 \text{ kg}^{-1} \text{ s}^{-1}$ .

The horizontal extent of the region of very low or negative potential vorticity was evident from the 700-mb vorticity analyses in Fig. 22. It can be seen from the cross-sections that the 700-mb pressure surface is roughly parallel to the 315 K isentrope. Consequently, the absolute

vorticity at 700 mb was equivalent to the absolute vorticity along an isentropic surface or the potential vorticity. During the period of line development, the region just north of the jet streak was characterized by negative relative vorticity, on the order of  $4 \times 10^{-5} \text{ s}^{-1}$ , comparable to or larger than the vertical component of the Coriolis parameter. Therefore, the potential vorticity was near zero or negative in the vicinity of the line formation. After the cloud line crossed south of the jet streak (1200 GMT 4 September), The potential vorticity of the flow in the vicinity of the line became increasingly positive. Therefore, some other mechanism had to be acting to maintain the convective line after this time.

### *3.3.2 Maintenance of the convective line*

In the discussion of the kinematic fields, it was pointed out that synoptic-scale deformation might be acting to maintain the convective line structure after the line had crossed south of the jet streak. Bluestein (1977) pointed out that synoptic-scale cloud lines in the tropics were often aligned along the axis of dilatation. He investigated the possibility that a frontogenetical circulation was acting to organize the cloud lines. In his analysis, however, the thermal forcing was too weak to be dynamically significant in the absence of latent heat release by the convection. Therefore, he hypothesized that the synoptic-scale deformation was acting to produce bands of cyclonic vorticity above the boundary layer and that a mechanism such as conditional instability of the second kind (e.g. Charney, 1971) was acting to maintain the convection in these bands. However, in the area where the line was observed a strong thermal gradient was present along the southern boundary of the SAL. Consequently, it seemed likely that a thermally driven

frontogenetical circulation was acting to maintain the line structure of the convection. To determine the applicability of a frontogenetical mechanism to the maintenance of the convective line the frontogenetical function defined by Pettersen (1956) was computed for the period after the line had crossed south of the jet streak.

Pettersen (1956) defined a frontogenetical function ( $F$ ) that in the absence of diabatic effect and vertical advection defines the rate that the synoptic-scale deformation and convergence of the horizontal winds can increase the thermal gradient. Pettersen defined ( $F$ ) as

$$F = 1/2 |\nabla\theta| (R \cos 2\beta - D) \quad (3.5)$$

where  $|\nabla\theta|$  is the magnitude of the existing horizontal temperature gradient,  $R$  and  $D$  are the resultant deformation and divergence of the observed horizontal wind field, and  $\beta$  the angle between the axis of dilatation and the isotherms. According to (3.5), horizontal convergence will always contribute to frontogenesis provided a horizontal temperature gradient exists within the region of convergence. However, deformation is frontogenetical only if the angle between the axis of dilatation and the isentropes is less than  $45^\circ$ . Strictly speaking, (3.5) is defined only for the case where the diabatic effects and differential vertical advectons are ignored. These effects are most likely important in any full interpretation of frontogenesis, but we can still make a reasonable estimate of the frontogenetic time scale from the kinematic fields computed in this case using (3.5).

Estimates of  $F$  were made using the fields of deformation and divergence at 850 mb where the strongest baroclinity had been observed along the SAL boundary. Figure 23 depicts

the 850-mb deformation fields during the period when the eastern end of the convective line was south of the jet streak. The convergence (not shown) in the vicinity of the line was positive, but an order of magnitude smaller than the resultant deformation. Therefore, to a first approximation

$$F \approx 1/2 |\nabla\theta| R \cos 2\beta$$

An estimate of  $\beta$  was made by taking the difference between the angle of the axis of dilatation and the angle of the shear vector from 900 - 800 mb, also illustrated in Fig. 23. This difference is a good estimate of  $\beta$  provided the wind field is nearly in thermal wind balance. Assuming,  $\beta$  is approximately 0,  $R = 2 \times 10^{-5} \text{ s}^{-1}$ , and  $|\nabla\theta|$  is about  $3 \times 10^{-5} \text{ K m}^{-1}$ , implies  $F$  is about  $3 \times 10^{-10} \text{ K m}^{-1} \text{ s}^{-1}$ , or nearly a doubling of the existing thermal gradient in one day from deformation alone in the absence of diabatic influences. The observation that there was convergence in the same region only adds to the magnitude of  $F$ . These computations suggest that synoptic-scale deformation was most likely acting to maintain the baroclinity along the boundary of the SAL in the region of the narrow convective line through a frontogenetical mechanism. This frontogenetical mechanism was also playing a role in the maintenance of the eastern end of the line as it was advected into the region of the ship array.

The kinematic and thermodynamic structure defined by the analyses outlined above require some subjectivity in handling soundings, i.e. correction of temperature biases. All of the corrections, however, followed procedures outlined by other researchers and were specified without regard to this case study. The observed low potential vorticity from the synoptic-scale

analyses supports the contention that in the vicinity of the convective line the potential vorticity was very small or slightly negative and appears to be quite reasonable in view of the well documented structure of the jet and horizontal temperature gradients observed in the two or three aircraft flights across these lines in the last few years (e.g. Carlson and Prospero, 1972). The strong vertical and horizontal wind shears that are typically found in the region of the midtropospheric jet require temperature gradients of just 2 - 3 K per 100 km for the jet to be inertially unstable. Observations made in the western Atlantic during BOMEX (Carlson and Prospero, 1972), over 3000 km from Africa, show thermal gradients along a constant pressure surface, in the region of the jet (the boundary of the SAL), of 4 K in 40 km.

The results from this case study support the hypothesis that the long narrow convective line formed within a region of symmetric inertial instability and remained in that region for some time before other mechanisms started to become important. The line structure appeared to be maintained initially by the symmetric instability of the easterly jet in the wave ridge. Later, as the line passed to the cyclonic side of the jet, it appeared to be maintained by a frontogenetical type circulation, possibly in combination with the convective circulations. In the next section, the importance of the symmetric inertial instability in organizing the convective lines, and a physically plausible mechanism for the origin of the inertially unstable air will be discussed.

#### **4. Discussion of symmetric inertial instability and the origin of the negative potential vorticity**

In the previous section, it was pointed out that the long lines of convection are observed in a region of the synoptic-scale waves where there is very low or slightly negative potential vorticity, and it was suggested that inertial instability in the lower and middle troposphere may account for the growth and initial maintenance of the convective lines. In this section symmetric inertial instability is described, its possible role in the organization of the convective lines is summarized, and the physical mechanisms that could lead to the generation of negative potential vorticity in the eastern Atlantic are discussed.

##### **4.1 Role of symmetric inertial instability in organizing convective lines**

Four aspects are of particular importance to the present study: the conditions for symmetric inertial instability, the growth rate of symmetrically unstable perturbations, the structure and spatial dimensions of the resultant circulations, and the organization of convection into long - lived lines by the symmetrically unstable circulations.

##### ***4.1.1 Conditions for symmetric inertial instability***

The stability of symmetric motions in rotating fluids with horizontal and vertical density gradients has been discussed by several authors. Stone (1966) solved the equations for the special

case of inviscid, Boussinesq, baroclinic flow with constant vertical shear and no horizontal shear.

He showed that the flow is unstable for symmetric disturbances if

$$Ri < 1$$

where  $Ri$  is the Richardson number. For the fully viscous, but linear equations, Emanuel (1979a) has shown that the condition for stability is singular with respect to the diffusion coefficients; that is, the solution of the viscous system in the limit of vanishing diffusion differs from the inviscid solution. This physical peculiarity was first noted by McIntyre (1970), who showed that the instability criterion for the case of viscous baroclinic flow with both horizontal and vertical shear is

$$Ri < f/\tilde{\eta} \left[ (1 + P)^2 / 4 P \right]$$

where  $P = \nu/\kappa$  is the Prandtl number,  $\nu$  and  $\kappa$  being the coefficients of momentum and heat diffusion, respectively,  $f$  the Coriolis parameter, and  $\tilde{\eta}$  the absolute vorticity. The quantity in brackets is smallest when  $P = 1$ , and becomes large as  $P$  approaches zero or infinity. This behavior implies that unequal diffusions of heat and momentum are destabilizing. When  $P = 1$  the stability criterion is

$$Ri < f/\eta \quad (4.1)$$

which for a flow that is in hydrostatic and geostrophic balance reduces to

$$g q / f N^2 < 0 \quad (4.2)$$

where  $q$  is the potential vorticity equivalent to that defined in (3.4) divided by  $\alpha\theta$ ,  $f$  the Coriolis parameter, and  $N^2$  the Brunt - Vaisala frequency (e.g. Hoskins, 1974; Emanuel, 1978). This relation implies that if  $f$ ,  $g$ , and  $N^2$  are positive, the condition required for instability is that the potential vorticity be negative. When the diffusion coefficients of the heat and momentum are unequal ( $P \neq 1$ ), the flow is also unstable for very small, but positive values of potential vorticity (Emanuel, 1979a).

The case study described in chapter 3 indicates that the lines are originally observed in a region with very low or slightly negative potential vorticity in the lower troposphere. The presence of air with  $q$  less than or equal to 0 suggests that the environment where the lines form can be inertially unstable regardless of the value of  $P$ .

#### *4.1.2 Growth rate of a symmetrically unstable perturbation*

Stone (1966) showed that in the inviscid case with no horizontal shear, the maximum linear growth rate ( $\omega$ ) for symmetrically unstable perturbations is

$$\omega^2/f^2 = [ (1 / Ri) - 1 ].$$

He noted that the largest linear growth rates were associated with perturbations of vanishing horizontal length scale in the direction transverse to the shear. However, the dependence of  $\omega$  on the transverse wavelength is not great for small wavelengths, so that Stone (1966) was able to define a maximum wavelength for instability. He found that the initial growth rates for symmetric disturbances exceeded those of baroclinic and Kelvin - Helmholtz instabilities when the Richardson number (Ri) lies between .25 and .95.

Emanuel (1978) showed that for the fully viscous system the hydrostatic linear growth rate may be expressed as

$$\omega^2/f^2 = 1/Ri [(1 + P)^2 / 4 P] - \eta/f \quad (4.3).$$

Whereas in the stability criterion  $P \neq 1$  decreases the stability, in (4.3),  $P \neq 1$  reduces the linear growth rate of the unstable perturbations. McIntyre (1970) has shown that both the inviscid and the diffusive modes of the instability have comparable growth rates; the inviscid modes being the largest. Physically, the instability for the viscous modes is fundamentally inertial in character, since the diffusion, when it is destabilizing, only acts to break the constraints of heat and/or angular momentum conservation following the parcel motions. When diffusion is added, a diffusive time scale must be considered as well, particularly because the diffusion makes the instability possible when  $P \neq 1$ . However, without knowing the value of  $P$ , the maximum linear growth rate can be determined by assuming  $P = 1$ .

For this case study, an estimate of the maximum linear growth rate of a symmetrically unstable perturbation in the vicinity of the jet streak was computed using (4.3) with  $P = 1$ . For a flow in hydrostatic and geostrophic balance where  $P = 1$ , Emanuel (1978) has shown that (4.3) reduces to

$$\omega^2/f^2 = -gq / fN^2 \quad (4.4)$$

where  $q$  is defined as in (4.2). Substituting from the observations summarized in section 3.3.1, values for the various parameters in (4.4) ( $f = 3.5 \times 10^{-5} \text{ s}^{-1}$ ;  $N^2 = 8 \times 10^{-5} \text{ s}^{-2}$ ;  $q = -5 \times 10^{-11} \text{ m}^{-1} \text{ s}^{-1}$ ; and  $g = 9.8 \text{ m s}^{-2}$ ) yields a growth rate of about  $1.5 \times 10^{-5} \text{ s}^{-1}$  or an e-folding time of 18 - 20 h. An estimate of the minimum length scale ( $L$ ), parallel to the shear vector needed for such a perturbation to grow by a factor of  $e$  can be determined from the product of the e-folding time ( $t$ ) and the speed of the mean flow parallel to the shear vector in the lower troposphere ( $u$ ). If  $t = 18 - 20 \text{ h}$  and  $u = 4 - 5 \text{ m s}^{-1}$ , then  $L$  is about 300 km. This length scale is in good agreement with the observations that the long-lived convective line formed between 1800 GMT 3 September and 0000 GMT 4 September in the 250 km gap between the preexistent cloud line west of the ridge and the coast of West Africa.

#### *4.1.3 Structure and dimensions of symmetrically unstable circulations*

Stone (1966) found that if the flow is inertially unstable, the circulations that develop for the inviscid case are two-dimensional rolls with the axes of the circulations aligned along the

shear vector and sloped along isentropic surfaces. In his analysis, the most rapidly growing disturbance had vanishing horizontal length scale in the plane perpendicular to the shear. The instabilities in the viscous solutions, reported by Emanuel (1979b), also take the form of rolls sloped along isentropic surfaces. The structure of these rolls has been determined numerically by Emanuel (1979b) and is depicted in Fig. 24.

The streamlines, as illustrated in Fig. 24 a, take the form of closed vortices elongated along isentropic surfaces sloping toward the colder air. As can be seen in Fig. 24, the regions of ascent are characterized by negative temperature and along line velocity perturbations, while the converse is true in the regions of descent. In his discussion, Emanuel (1979b) pointed out that the rolls clearly extend into the boundary layer, where they would be able to modify the moisture patterns through convergence in the boundary layer. At the surface the highest pressure occurred on the cold air side of the updraft and low pressure on the warm side of the updraft. Emanuel (1979b) found that the horizontal length scale for the most unstable mode, in the viscous solutions, was also singular with respect to the diffusion coefficients, and depended on the depth of the unstable domain divided by the slope of the isentropic surfaces.

Very few details of the roll structure of the convective lines could be verified from the observations in the case study. However, the surface observations at the ships affected by the line were in general agreement with the structure of the rolls as determined by Emanuel (1979b). The observations showed that there was low pressure, and positive vorticity at the leading edge of the line, and a sharp pressure rise behind the line. The observations presented in chapters 2 and 3 indicate that the convective lines typically extended over a depth of about 3 - 4 km outside of the monsoon trough zone, and that the isentropes in the region where the lines are

found have a slope on the order of 2 - 3 K per 100 km. These values when put into the expressions derived by Emanuel (1979b) yield a horizontal length scale on the order of 100 - 200 km. The case presented in detail earlier had only one main line and no spacing could be determined. However, there were other cases in Phase III when more than one line was observed. As can be seen in Table 5 and Fig. 14, the line spacings were generally 90 - 120 km, in close agreement with the computed values.

#### *4.1.4 Organization of convection by symmetrically unstable circulations*

Emanuel (1979a) has hypothesized that inertially unstable rolls might be important in organizing mesoscale convective lines and suggested that lines formed by this mechanism could persist for long time periods. He described how an environment that is characterized by weak inertial stability (or inertial instability), as well as convective instability, would be more favorable for vigorous convective development than an environment that is just convectively unstable. He argued that in an environment characterized by uniform convective instability and no wind or large-scale horizontal density variations, the slice method indicates that convection occurs when the kinetic energy generated from buoyancy in ascending parcels exceeds that required to do work against buoyancy by the descending parcels. The amount of work performed by the descending parcels depends on the dry static stability. Thus the ability of convection to form in this inertially stable environment depends not only on the degree of convective instability, but also on the dry static stability. In a large-scale environment characterized by convective instability and uniform vertical wind shear in thermal wind balance with the horizontal

temperature gradient, the amount of work performed by the compensating descending parcels is minimized if the convection occurs in lines parallel to the wind shear. Emanuel (1979a) showed that the amount of work done by the descending parcels is then dependent on the inertial stability of the environment, such that if the flow is inertially unstable, the work done by the descending parcels is negative. Under these conditions mesoscale circulations would develop along with the convection and might in turn support the convection by providing moisture convergence on the mesoscale. Thus, in this type of environment, the possibility of having convective lines aligned parallel to the shear is determined by the symmetric inertial stability which is dependent on the absolute vorticity and the static stability, or, as pointed out above, potential vorticity.

Emanuel (1979a) also pointed out that the convection could persist over many cloud lifetimes in such an environment if there is a mechanism, such as the release of latent heat in the ascending parcels of the convection, that can maintain the instability of the environment to symmetric circulations. In such a situation, the latent heat in the convection could act to maintain the inertial instability, while the resultant mesoscale inertial circulation supplies moisture to the convection through mesoscale convergence. Another possibility is that the synoptic-scale deformation acts to maintain the strong baroclinity in the lower troposphere in the vicinity of the jet, which in turn is necessary to maintain the instability of the environment to symmetric circulations. Direct frontogenetical circulations could act to strengthen the baroclinity as in mid - latitude frontal zones. The observations discussed in chapters 2 and 3 indicate that this may be the case, particularly after the convective lines have formed and entered the region of the monsoon trough zone.

In summary, the observations of the development and movement of the convective lines discussed in chapters 2 and 3 showed that the lines were aligned along the shear vector in the lower troposphere and were in a region of inertial instability or weak stability, in agreement with the above discussion. The observations of the cloud line from the case study indicated that the convective line was coincident with the region of very low or slightly negative potential vorticity in the lower troposphere, at least during the time before it crossed the ship array. While it could be argued that the convection in the lines was a result of an instability in the boundary layer, it seems more likely that symmetric inertial instability in the lower troposphere, but above the boundary layer, accounted for the development and maintenance of the convective lines that formed off the coast of Africa and then traveled toward the southwest over the eastern tropical Atlantic Ocean. Thus, an important remaining question is to determine how the negative potential vorticity was generated.

#### 4.2 Origin of inertially unstable airmass

It was shown in the previous chapters, that the air with very low or slightly negative potential vorticity originated over northwest Africa, rather than the southern hemisphere. Since potential vorticity is observed to be positive in almost all of the northern hemisphere, and it is conserved in the absence of frictional and diabatic effects (e.g. Eliassen and Kleinschmidt, 1957), then frictional and diabatic processes must be acting to destroy positive potential vorticity upstream in the flow. This destruction is most likely occurring over the desert in central West Africa. In the remainder of this section, the climatological conditions in this region of West

Africa are briefly summarized and a hypothesis is proposed to explain the generation of the negative potential vorticity in terms of the typical atmospheric structure in the region.

#### 4.2.1 Mean conditions over West Africa from 30°N to the equator

The mean lower tropospheric wind structure and surface temperature distribution over this region of Africa for late summer are shown in Fig. 25. Figures 25 a and 25 b show the mean surface and 700-mb streamlines and isotachs for Phase III of GATE from Reynolds (1977), and Fig. 25 c the mean sea-surface temperatures for Phase III of

GATE from Krishnamurti *et al.* (1976) combined with the August mean daily averaged surface temperatures from climatology presented by Burpee (1972). At the surface a cyclonic circulation was centered at about 20°N, 15°W with strong northerly flow along the coast and weaker southerly (monsoon) flow over the interior. As can be seen in Figs. 25 a and 25 b, both the surface northerlies and southerlies decreased rapidly with height to a predominately east - west flow at 700 mb. Figure 25 c shows that in the region over the desert between 5°E and 10°W, and between 18° and 30°N, the temperatures were typically greater than 35°C, while just west and south of this region the surface temperatures were considerably lower. The mean position of the easterly jet at 700 mb in Fig. 25 b, was centered along the strongest north - south surface temperature gradient near 16°N on the southern fringe of the Sahara (Fig 25. c).

A number of investigators have studied the stability of the African jet (e.g. Burpee, 1972; Reed *et al.*, 1977; Mass, 1979). Figure 26 depicts the mean north - south cross-sections of the zonal wind, the vertical component of the absolute vorticity, and the temperature deviation from

the values at the equator ( $\Delta$ -latitude = -12) for Phase III of GATE from Reed *et al.*, (1977). These mean fields were calculated using observations within the region extending from 10°E to 31°W and from 1°S to 26°N. The easterly jet was positioned along the strongest north - south temperature gradient in the lower troposphere. North of the mean midtropospheric easterly jet position, there was a distinct minimum of absolute vorticity extending from the surface at  $\Delta$ -latitude = 0 (12°N) to 700 mb at  $\Delta$ -latitude = 8 (20°N). The investigators deduced from these observations that the midtropospheric jet was barotropically unstable, and the instability accounted for the synoptic-scale waves that were observed in the lower troposphere as Burpee (1972) had shown prior to GATE.

In chapter 2, it was pointed out that the lines of convection typically formed in the ridge portion of the wave as this portion of the wave crossed the west coast of Africa. Karyampudi (1979) has shown that the lower-tropospheric temperature gradient at the boundary of the SAL and the midtropospheric jet were strongest in the wave ridge. As can be seen in Figs. 11 and 16, the ridge was characterized by very small values of potential vorticity in the lower troposphere which were centered just north of the jet, near 17°N, above the boundary layer (around 800 mb). Figure 27 shows that the mean vertical component of the absolute vorticity, in the ridge portion of the wave, was also a minimum near 800 mb near 16°N.

#### 4.2.2 *Time rate of change of potential vorticity*

The formula for potential vorticity,  $q$ , expressed in isentropic coordinates is:

$$q = \alpha \underline{\eta} \cdot \nabla \theta \quad (4.5)$$

where  $\alpha$  is the specific volume,  $\underline{\eta}$  the absolute vector vorticity, and  $\nabla \theta$  the three-dimensional potential temperature gradient or static stability. The absolute vector vorticity can be expressed as

$$\underline{\eta} = 2\underline{\Omega} + \nabla \times \underline{V}$$

where the first term on the right is the earth's vorticity and the second term is the three-dimensional relative vorticity. Since horizontal variations of  $\alpha$  are generally small, it may be treated as a constant, and the time rate of change of  $q$  may be written as

$$dq/dt = \alpha \underline{\eta} \cdot \nabla \dot{\theta} + \alpha \nabla \theta \cdot \nabla \times \underline{F} \quad (4.6)$$

where  $\dot{\theta}$  or  $d\theta/dt$  is the time rate of change of potential temperature (diabatic heating), and  $\underline{F}$  is the vector frictional force per unit mass (e.g. Staley, 1960).

It is useful to consider the physical interpretation of the terms on the right hand side of (4.6). If the flow is assumed adiabatic and frictionless, both terms on the right vanish and (4.6) reduces to the conservation of potential vorticity theorem of Ertel (1942). It can be seen from (4.5) that conservation of potential vorticity requires that the dot product of  $\nabla \theta$  (stability) and the absolute vector vorticity be invariant.

The first term on the right of (4.6) is the "stability change" term (Gidel and Shapiro,

1979). It forces potential vorticity changes by the production (destruction) of static stability ( $\nabla\theta$ ) as a result of gradients of diabatic heating in the direction of the absolute vector vorticity ( $\underline{\eta}$ ). For example, if the flow has a positive component of absolute vector vorticity upward and the gradient of the diabatic heating has a component in the same direction (becoming more stable by warming above and/or cooling below), then the potential vorticity will increase through increasing static stability. The rate at which the diabatic effects alter the potential vorticity is proportional to the absolute vector vorticity.

The second term on the right - hand side of (4.6) is the "vorticity change" term (Gidel and Shapiro, 1979). It represents the change of potential vorticity resulting when the component of the curl of the frictional force is normal to the isentropic surfaces. For example, if the potential temperature gradient has a positive component in the vertical and the curl of the momentum flux divergence has a component in the same direction (increasing the vertical component of the relative vorticity and hence the absolute vorticity through differential vertical divergence of turbulent momentum flux) then the potential vorticity will increase. The rate at which the frictional effects alter the potential vorticity is proportional to the static stability.

#### 4.2.3 Destruction of positive potential vorticity

Over the desert, the strong diabatic heating at the surface will produce large changes in potential vorticity through both the vorticity change and the stability change terms. Figure 28 a is a schematic diagram based on the observations presented in section 4.2.1 of the kinematic and thermodynamic structure over the desert along the cross-section marked A - A' in Fig. 25.

Figure 28 b shows the contribution of the terms in the vorticity and the stability change terms to the change of  $q$  in the lower troposphere in the region indicated by the circled X. In this figure, and the rest of the chapter, the discussion of the changes of potential vorticity will deal principally with the atmospheric structure of the ridge of the synoptic-scale wave at two locations: in the desert region, near the African coast, and in the area of the eastern Atlantic where the very low or slightly negative potential vorticity was observed; i.e. the region just north of the midtropospheric jet (about  $17^\circ\text{N}$ ) between 700 and 950 mb. The flow is assumed to be east - west, as it is in the ridge portion of the wave. For ease of interpretation, the coordinate system used in the schematic diagrams and subsequent description of vector components is Cartesian, rather than isentropic. This Cartesian coordinate system has the unit vectors  $\mathbf{i}$  in the x-direction (positive toward the east),  $\mathbf{j}$  in the y-direction (positive toward the north), and  $\mathbf{k}$  in the z-direction (positive upward). To evaluate the products in (4.5) and (4.6), the vectors in the equations are separated into components along these directions.

As can be seen in Fig. 28 a, the air parcels over the desert in the position marked by the X are in a region of the lower troposphere characterized by very strong easterly shear in the vertical (on the order of  $10^{-3} \text{ s}^{-1}$ ) and strong anticyclonic shear to the north of the jet (on the order of  $10^{-5} \text{ s}^{-1}$ ). The components of  $\tilde{\eta}$ , the vorticity of the earth ( $2\tilde{\Omega}$ ) and relative vorticity ( $\nabla \times \mathbf{V}$ ), are opposed in the  $\mathbf{j}$  and  $\mathbf{k}$  directions. As illustrated in Fig. 28 b, the earth's vorticity is toward the north and upward at an angle to the local horizontal (equal to the latitude,  $\phi$ , in degrees) and the relative vorticity is downward (negative in  $z$ ) and to the south (negative in  $y$ ). The  $y$ -component of the relative vorticity is larger than that of the earth's vorticity ( $2\tilde{\Omega}\cos\phi$ ), while the  $z$ -component is smaller than that of the earth's vorticity ( $2\tilde{\Omega}\sin\phi$ ): the Coriolis

parameter,  $f$ ). The resultant,  $\underline{\eta}$ , is negative along  $j$  (order  $10^{-3} \text{ s}^{-1}$ ), and slightly positive along  $k$  (order  $10^{-5} \text{ s}^{-1}$ ), in agreement with the mean cross-sections in Figs. 26 b and 27. The component of  $\underline{\eta}$  along  $i$  is very nearly zero or slightly positive because of very slight northerly shear of the meridional wind.

As shown in Fig. 28 a, the isentropes are approximately horizontal and the mean vertical stability ( $\partial\theta/\partial z$ ) is on the order of  $10^{-2} - 10^{-3} \text{ K m}^{-1}$ . However, air parcels crossing the desert are intensely heated at the surface during the day because of strong solar radiation. Air parcels in contact with the ground during the daylight hours are heated largely by upward vertical sensible heat flux, while there is little variation of diabatic heating in the  $x$  or  $y$  direction. The resultant  $\nabla\theta$  is directed toward the ground. Based on measurements over similar terrain (e.g. over salt flats in California by Vehrencamp, 1953 and over the Gobi Desert reported by Geiger, 1966), maximum diabatic heating at the surface near solar noon is probably around  $400 - 500 \text{ w m}^{-2}$ . This heating produces vigorous dry convection throughout a deep layer that is in convective contact with the ground and has been referred to as the SAL by Carlson and Prospero (1972). During the rest of the day the sensible heat flux at the surface is smaller than that at the maximum, and at night, when the lapse rate near the surface is very stable, the heat flux is slightly negative. However, on the mean, over a whole day, it is likely that the diabatic heating at the ground is strongly positive, with average diabatic heating rates at the surface on the order of  $10^{-3} \text{ K s}^{-1}$ . Assuming that  $\theta$  decreases to near zero in 1 - 2 kilometers of height, the mean  $\partial\theta/\partial z$  will be on the order of  $10^{-6} \text{ K m}^{-1} \text{ s}^{-1}$ .

The vertical component of  $\underline{\eta}$  is oriented in the opposite direction to the vertical component of  $\nabla\theta$  resulting in a destruction of  $q$  through the stability change term in (4.6). That is, the

diabatic heating reduces the static stability in the lower troposphere faster than the absolute vorticity can adjust to these changes. As a result of the decreased stability in the vertical, the isentropes tilt more nearly vertical and consequently, the positive component of  $\underline{\eta}$  along  $\nabla\theta$  is reduced and approaches zero as the heating continues. As can be seen from (4.5), this reduction brings  $q$  closer to zero. An estimate of the time scale over which this process occurs can be gained from the following consideration. The only component of  $q$  greater than zero in (4.5) is  $q_z$  or  $\alpha\eta_z \partial\theta/\partial z$ , which is being reduced through the vertical component of the stability change term in (4.6),  $\alpha\eta_z \partial\dot{\theta}/\partial z$ . Therefore, the rate at which  $q$  is being reduced by the stability change term can be expressed as

$$d/dt(\alpha\eta_z \partial\theta/\partial z) = \alpha\eta_z \partial\dot{\theta}/\partial z$$

or

$$dq_z/dt = \alpha\eta_z \partial\theta/\partial z [(\partial\dot{\theta}/\partial z) / (\partial\theta/\partial z)] = q_z [(\partial\dot{\theta}/\partial z) / (\partial\theta/\partial z)]$$

which reduces to

$$d \ln q_z/dt = [(\partial\dot{\theta}/\partial z) / (\partial\theta/\partial z)] \quad (4.7)$$

If the ratio in brackets in (4.7) is relatively constant and negative in the mean, then  $q_z$  will decay exponentially. From the typical mean values of  $\partial\dot{\theta}/\partial z$  and  $\partial\theta/\partial z$  given above, the e-folding

time for the decay of  $q$  will probably be on the order of a few hours. In the few days it takes a parcel to cross the desert, an air parcel may be in convective contact with the surface for 12 - 24 h. During these hours the potential vorticity becomes very small, possibly zero, in the region of lowest potential vorticity in the ridge of the synoptic-scale wave.

The exponential time dependence of  $q$  through the reduction of the vertical stability can only reduce  $q$  to values near zero, it cannot make  $q$  negative. Therefore some other mechanism must be acting to make  $q$  negative before the wave enters the region where the convective lines form off the west coast of Africa.

#### *4.2.4 Generation of negative potential vorticity*

As noted in the discussion of the cross-sections in Fig. 21, prior to the time the jet streak crossed the coast of West Africa (Fig. 21 a), the region of very low and slightly negative potential vorticity was confined to the middle troposphere (700 - 800 mb), just north of the jet streak. However, after the jet streak had crossed the coast (Fig. 21 b), this region of very low and slightly negative potential vorticity extended lower in the troposphere, to about 950 mb. Consequently, two separate mechanisms were probably acting to generate the slightly negative potential vorticity in the region just north of the jet. One process generated negative potential vorticity over the Sahara in the midtroposphere, while another process generated very low or slightly negative potential vorticity in the lower troposphere in the vicinity of the coast of West Africa.

### *Over the Sahara*

In the previous section it was pointed out that the strong diabatic heating over the desert during the day generates vigorous dry convective overturning throughout the SAL (often up to 600 mb). Besides altering the potential vorticity through the stability change term, this strong convective overturning was also acting to alter the potential vorticity through the vorticity change term. Air parcels in contact with the ground during the daylight hours are largely mixed in the vertical by the vigorous convective overturning within the SAL, while there is much less mixing in the x or y direction (Fig. 28 b).

As air parcels in the wave cross the desert their absolute vorticity was reduced through differential turbulent momentum flux divergence across the SAL boundary. As can be seen in Fig. 28 b, the most important term of the momentum flux divergence within the SAL was  $F_z$ , the vertical momentum flux divergence defined as

$$F_z = \partial/\partial z \langle w'u' \rangle i + \partial/\partial z \langle w'v' \rangle j$$

where the angle bracket represents a time average at a single point in space over some characteristic turbulent time scale and the prime is the turbulent deviation from the time average. In the vicinity of the jet streak this relation can be further simplified by ignoring the vertical flux divergence of the meridional wind perturbation, implying

$$F_z \approx \partial/\partial z \langle w'u' \rangle.$$

Physically, the vertical turbulent momentum flux divergence was acting to transport the high zonal momentum of the jet away from the level of maximum wind. Typical values of  $\langle w'u' \rangle$ , from observations in the vicinity of jet streaks in the free atmosphere are about  $0.7 - 1.0 \text{ m}^2 \text{ s}^{-2}$  (Lilly and Kennedy, 1973; Kennedy and Shapiro, 1975). Assuming this momentum flux occurs through a depth of 1 - 3 km, then the vertical momentum flux divergence will be on the order of  $10^{-3} \text{ m s}^{-2}$ .

South of the SAL, the vertical momentum flux divergence was probably greatly reduced ( $\approx 0$ ). Assuming this reduction occurs over a distance on the order of 100 km, then the vertical component of the curl of the momentum flux divergence defined as

$$(\nabla \times \tilde{F})_z \approx - \partial/\partial y (\partial/\partial z \langle w'u' \rangle)$$

was negative, and on the order of  $10^{-8} \text{ s}^{-2}$ . Consequently, the vertical component of  $\nabla \times \tilde{F}$  is oriented in the opposite direction to the vertical component of  $\nabla \theta$  resulting in a destruction of  $q$  through the vorticity change term in (4.6). That is, the differential turbulent momentum flux divergence between the air parcels in the SAL and those south of the SAL reduces the component of the absolute vorticity parallel to the potential temperature gradient. As can be seen from (4.5) this reduction brings  $q$  closer to zero. An estimate of the time scale over which this process occurs can be gained from the following consideration. As stated in the previous section, the only component of  $q$  greater than zero in (4.5) is  $q_z$  which is being reduced through the

vertical component of the vorticity change term in (4.6) approximated as  $-\alpha \partial \theta / \partial z \partial / \partial y [ \partial / \partial z \langle w'u' \rangle ]$ . Therefore, the rate at which  $q$  is being reduced by the vorticity change term can be determined from this expression. Typical values of  $-\partial / \partial y (F_z)$  (on the order of  $-10^{-8} - -10^{-9} \text{ s}^{-2}$ ) and  $\partial \theta / \partial z$  (on the order of  $10^{-3} \text{ K m}^{-1}$ ) indicate that, over the Sahara, the effect of the vorticity change term on  $dq/dt$  is comparable to and of the same sign as that of the stability change term. However, the vorticity change term will most likely be larger than the stability change term in the midtroposphere near the jet maxima where the reduction in the zonal wind by the vertical momentum flux divergence will generate the strongest lateral wind shears. Consequently, in this area the potential vorticity is being reduced faster than the exponential decay rate computed for the stability change term, and if  $q$  is small enough, it could become negative.

#### *Along the coast*

As air parcels in the wave approach the coast, they enter an area affected by coastal upwelling and characterized by relatively cool sea - surface temperatures. Figure 29 a is a schematic diagram, based on the observations presented in section 4.2.1, of the kinematic and thermodynamic structure of the lower troposphere at the coast along the north - south and east - west cross-sections marked B - B' and C - C' in Fig. 25, respectively. Figure 29 b shows the contribution of the terms in the stability change term to  $dq/dt$  in the region of the wave ridge indicated by the circled X in Fig. 29 a.

The meridional and vertical shears of the zonal wind in the region of interest are very similar to those over the desert. However, at the coast, there is a marked increase in the vertical

shear of the meridional wind because of the strong low-level east - west temperature gradient (e.g. Fig. 25 c). Figure 30 shows a typical noontime sounding along the coast at Nouadhibou, Mauritania (21°N, 17°W; indicated by N in Fig. 25) and over the desert at Tessalit, Mali (20°N, 1°E; T in Fig. 25). As can be seen in Fig. 30 a, the strong northerly winds along the coast decrease rapidly with height, causing a strong negative component of relative vorticity along  $i$  (on the order of  $10^{-3} \text{ s}^{-1}$ ). This component of the relative vorticity is unopposed by any component of the earth's vorticity in the east - west flow and as indicated in Fig. 29 b, the resultant,  $\underline{\eta}$ , has a negative component along  $i$  and  $j$ , and a small positive component along  $k$ .

The vertical stability in the region of interest has been reduced by diabatic heating over the desert, but is still positive. The vertical component of  $\nabla\theta$  in the lower troposphere changes sign at the coast, from strongly negative (toward the surface) over the desert to positive (away from the surface) over the sea surface because of the abrupt decrease of the surface temperature from east to west near the coast. Without the strong diabatic heating at the surface, the turbulent momentum flux is greatly reduced and the contribution of the vorticity change term to the time change of the potential vorticity becomes negligible compared to the stability change term in (4.6) (Fig. 29 b).

Very little is known about the time and space scales required for the diabatic heating to modify the stability of the lower troposphere, because very few observations of the wind and thermodynamic structure in the lower troposphere exist in this area. However, an estimate of the vertical extent of the change in sign of the vertical component of  $\nabla\theta$  can be made from Fig. 30 b. As can be seen in Fig. 30 b, the thermodynamic structure was identical at both stations above 830 mb; the potential temperature was 313 K, characteristic of the SAL. However, in the

surface layer, the desert station had an isentropic lapse rate with a surface temperature of 36°C, while the coastal station had a very stable lapse rate of potential temperature below 830 mb and a very cool surface temperature of 23°C. Nouadhibou is on the west coast of Africa, and the air near the surface had probably recently been over the cold sea surface, explaining the cold surface temperature. The depth over which the change in thermodynamic structure between the low-level air of the desert and that of the coast probably delineates the vertical extent of the change in  $\partial\theta/\partial z$ .

In the same region as the change in  $\partial\theta/\partial z$ , there is positive  $\partial\theta/\partial x$  (toward the desert). From Fig. 25 c, it seems reasonable to assume that the changes of diabatic heating in the x-direction occur on the scale of a few hundred km. Therefore,  $\partial\theta/\partial x$  will typically be two orders of magnitude smaller than  $\partial\theta/\partial z$  ( $10^{-8} \text{ K m}^{-1} \text{ s}^{-1}$  and  $10^{-6} \text{ K m}^{-1} \text{ s}^{-1}$ , respectively), while  $\eta_x$  is typically two orders of magnitude larger than  $\eta_z$  ( $10^{-3} \text{ s}^{-1}$  and  $10^{-5} \text{ s}^{-1}$ , respectively). As can be seen in Fig. 29 b, the resultant  $\nabla\theta$ , is positive along k (away from the surface) and along i (back toward the desert).

The components shown in Fig. 29 b, indicate that the x-component of the stability change term is acting to reduce q, while the vertical term is acting to increase it. In order to have  $dq/dt$  less than zero, it is necessary to have

$$| \eta_x \partial\theta/\partial x | > | \eta_z \partial\theta/\partial z | \quad (4.8)$$

somewhere in the region of interest. If q is already approximately zero, these conditions will make q negative.

Figure 31 depicts the change of the important terms in  $dq/dt$  as the parcels in the ridge cross the desert and the coast. As described in the previous subsection, the vertical component of the stability change term yields an exponential decay of  $q$  over the desert while the x-components are zero. At the coast, but after the change in sign of  $\partial\theta/\partial z$ , the above scale argument implies that the products in (4.8) are of the same order of magnitude. However, slightly inland where  $\partial\theta/\partial z$  changes from negative to positive,  $\partial\theta/\partial x$  is strong and nonzero and (4.8) is satisfied. In this region, if  $q$  is small positive or zero,  $q$  would become negative:

The depth of the layer in the lower troposphere where (4.8) holds will be determined by the depth over which the change in diabatic heating occurs. Figure 32 shows the vertical distribution of the terms in (4.8) in the region just inland from the coast marked by the arrow in Fig. 31 (about  $17^\circ W$ ). As can be seen in Fig. 30 b, the change in the diabatic heating probably extends to 800 - 850 mb. Assuming that both  $\partial\theta/\partial z$  and  $\partial\theta/\partial x$  decrease linearly with height, and that  $\eta_z$  is a minimum above the surface as in Fig. 28, and that  $\eta_x$  is nearly constant in the lower troposphere, then (4.8) will hold in the lower troposphere through a layer from about 800 - 950 mb. Thus, in the vicinity of the coast, the region where negative potential vorticity will be generated is above the surface but below about 800 mb. Over the Sahara, this region will be generated in the midtroposphere (700 - 800 mb), in good agreement with the observations in chapter 3 that the negative potential vorticity was observed in the midtroposphere before the jet streak crossed the coast and extended into the lower troposphere after the jet streak crossed the coast.

In summary, when the air parcels in the ridge portion of the wave are in convective contact with the ground over the desert, the vertical component of the gradient of diabatic

heating and the curl of the turbulent momentum flux divergence act to destroy the relatively low positive potential vorticity of the air parcels by reducing the component of the absolute vorticity along the potential temperature gradient. The diabatic heating is strong enough to reduce the low potential vorticity in the wave ridge just north of and below the midtropospheric jet to near zero. The differential turbulent momentum flux divergence across the boundary of the SAL acts to generate negative potential vorticity in the midtroposphere (700 - 800 mb) over the desert. When the air parcels in the wave ridge cross the coast, the gradient of diabatic heating in the east - west direction acts to generate negative potential vorticity. At the same time the vertical gradient of diabatic heating changes sign and contributes to the generation of positive potential vorticity, however, the vertical stability does not increase fast enough to compensate for the strong east - west temperature gradient so the potential vorticity becomes negative. In the vicinity of the coast, the generation of negative vorticity is strongest in the lower troposphere in the layer from about 800 - 950 mb.

## 5. Summary and suggestions for future study

### 5.1 Summary

Analyses of radar data obtained during Phase III of GATE have shown that mesoscale organization of deep convection in African wave disturbances usually occurred in the region of the wave west of the trough but east of the downstream ridge in the easterly flow. In this part of the wave three types of mesoscale lines frequently appeared: long slow-moving broad bands associated with the monsoon trough (monsoon trough bands); fast-moving lines of deep convection (squall lines); and long narrow lines aligned along the midtropospheric easterly jet (narrow lines).

The most vigorous deep convection in both the monsoon trough bands and the squall lines occurred in the region of low-level moisture convergence along the monsoon trough with the monsoon trough bands forming parallel to the trough and the squall lines propagating along it. The monsoon bands were normally oriented northeast - southwest and generally moved toward the west at  $7 - 8 \text{ m s}^{-1}$ , while the squall lines were typically oriented perpendicular to the monsoon trough bands and moved at twice the speed of these bands toward the west. Enhanced low-level convergence to the west of the wave troughs appeared to account for the formation and movement of the monsoon trough bands while the few squall lines that were observed in the GATE ship array originated over Africa to the west of a wave trough and moved faster than the wave into the region of low-level moisture convergence along the monsoon trough.

The results of this research indicate that the narrow lines most likely originated because

of inertial instability in the lower and middle troposphere. These lines formed near the African coast in and just upstream of the wave ridge near the leading edge of large dust plumes that were tracked back to a source region on the southern fringe of the Sahara desert. The dust acted as a tracer for hot, dry air called the Saharan Air Layer (SAL). In the vicinity of the GATE ship array, the southern boundary of the SAL was adjacent to the relatively cooler and moister air near the monsoon trough. Consequently, in this region there was a strong north-south, lower-tropospheric baroclinic zone and a midtropospheric easterly jet. The baroclinic zone and midtropospheric jet were strongest in and just upstream (to the east) of the wave ridge where the narrow lines were aligned with the jet and baroclinic zone. After the narrow lines formed, they drifted toward the southwest with the northerly flow in the lower-troposphere to the east of the wave ridge. During this stage of the line development, the linear structure of the convective line appeared to be maintained by a frontogenetical type mechanism which resulted from strong synoptic - scale deformation in the vicinity of the line.

Analyses of the mean composite wave structure for Phase III of GATE and from one case study showed that the narrow lines were found in a region of negative or very low potential vorticity in the lower troposphere. These values of potential vorticity indicate that the region was inertially unstable to symmetric circulations. The observed negative or very low potential vorticity appeared to be quite reasonable in light of the well documented structure of the midtropospheric jet and strong horizontal temperature gradients observed in the two or three aircraft flights across the SAL boundary in the last few years. Unfortunately no extensive GATE aircraft missions were made across the SAL boundary. Very few details of the theoretical structure of inertially unstable circulations could be verified directly from the

observations of the narrow lines. However, the spatial scales of the lines and the surface wind and temperature observations at the ships affected by the line in the case study were in general agreement with the theoretical structure. These observations suggest that the narrow lines originally formed as a result of symmetric inertial instability in the lower troposphere off the coast of Africa.

A hypothesis was proposed to explain the generation of the negative potential vorticity in the ridge portion of the wave. The proposed generation mechanism depends on the vertical and horizontal variations of diabatic heating and turbulent momentum flux divergence in the lower troposphere over the desert and along the Atlantic coast of West Africa. When the air parcels in the ridge portion of the wave are in convective contact with the ground over the desert, the vertical component of the gradient of diabatic heating and the curl of the turbulent momentum flux divergence act to destroy the relatively low positive potential vorticity of the air parcels by reducing the component of the absolute vorticity along the potential temperature gradient. The diabatic heating is strong enough to reduce to near zero the low potential vorticity in the portion of the wave ridge that is just north of and below the midtropospheric jet. The differential turbulent momentum flux divergence across the SAL boundary acts to generate negative potential vorticity in the midtroposphere (700 - 800 mb) over the desert.

Near 16°N along the coast of West Africa, the sea surface temperatures are relatively cool and consequently, there is a strong east - west temperature gradient in the lower troposphere. As a result of this temperature gradient the vertical gradient of diabatic heating near the surface changes sign abruptly in the coastal region. The vertical stability in the lower troposphere cannot increase fast enough to compensate for the strong east-west temperature gradient. The

generation of negative potential vorticity is strongest in the lower troposphere in the layer from about 800 - 950 mb.

## 5.2 Suggestions for future study

One of the more interesting results from this thesis was the reexamination of the strong mesoscale baroclinic zones in the lower troposphere at the southern boundary of the SAL previously described by Carlson and Prospero in the Caribbean and in the eastern Atlantic, and the documentation of the role this baroclinic zone played in organizing mesoscale convective features. The presence of this baroclinic zone in the lower troposphere over the tropical Atlantic Ocean near the African coast and in the Caribbean poses an immediate question about how the baroclinic zone is maintained as it crosses the Atlantic. As noted in this study, the synoptic-scale deformation may play an important role in the maintenance of the baroclinic zone through a frontogenetical process, as in the mid-latitudes. From the discussion in chapter 4, it can be seen that the atmospheric susceptibility to frontal circulations would be higher in a region of weak inertial stability. If an indirect frontal circulation developed in the region of the baroclinic zone, it is not clear how it would affect the maintenance of the convection in the long narrow cloud lines. Possibly the frontal circulation and the circulation in the convective lines are both needed to maintain the baroclinity. Investigation into the possible role that the synoptic-scale deformation plays in maintaining the baroclinic zone along the boundary of the SAL could be pursued both observationally and theoretically.

Observationally, an analysis of the deformation fields in a number of cases from GATE

in which the baroclinic zone is present will help determine whether frontogenesis could occur along the boundary of the SAL. Theoretical studies will be needed to determine how the possible frontal circulations could exist above the boundary layer, possibly through the presence of convection. The presence of the baroclinity in the lower troposphere over the Atlantic also poses questions about the effect it might have on the development of other convective systems in addition to the long narrow cloud lines. An interesting study would be to determine what role this baroclinic zone might play, if any, in hurricane or tropical storm formation. A cursory analysis of the satellite images from GATE indicated that the narrow cloud lines associated with the boundary of the SAL could be tracked across the Atlantic and, on most occasions, were in the general region where the 4 tropical cyclones originating from African waves formed during the summer of 1974. However, many hurricanes are observed in the Pacific and there are no documented observations of the long convective lines or the baroclinity in the lower troposphere over the Pacific. This may be because the convective lines and the baroclinity do not exist over the Pacific or that no one has noticed them (which seems unlikely). In either case, the fact that they do exist over the Atlantic in the region of tropical storm formation suggests that the baroclinity along the SAL's boundary may play some role in hurricane formation over the Atlantic.

Observationally, a climatology of the long convective lines over the Atlantic Ocean together with the existing hurricane climatologies might lead to a better documentation of the possible interaction of the midtropospheric baroclinic zones and tropical storms. This could be done using existing satellite imagery and synoptic-scale observations taken in the past few years. The long convective lines, dust, and tropical storms are easy to identify and track using satellite

imagery. The location of the strong mid-tropospheric baroclinity at the dust boundary can be determined from the position of the narrow cloud lines, because as documented in this study, these cloud lines are good indicators of the position of the baroclinic zone. In conjunction with the climatological study, more information is needed on the structure and intensity of the baroclinic zones along the SAL boundary, and a means of determining its strength by remote sensing (satellites). A possible observational study would be to make some direct aircraft measurements of the SAL boundary when it is over the Caribbean, either in conjunction with a hurricane reconnaissance flight or as a separate field study. Measurements of this type would be useful in defining the spatial scales and the strength of the baroclinic zones. The flight information would also be useful in a comparison with estimates of intensity and location of the baroclinic zone made using satellite techniques. Carlson (1979) has described a technique for determining the radiative heating rates within the SAL using satellite measurements of the optical depth of the dust. Possibly a technique could be devised along the same lines to estimate the strength of the baroclinic zone at the SAL boundary.

At the same time, theoretical studies will be needed to investigate the effect of the midtropospheric baroclinic zone on hurricane development. Most studies of hurricane formation assume very little shear in the mid-troposphere and it is not clear how the presence of strong baroclinity might alter existing hypotheses.

The destruction of positive potential vorticity by diabatic processes may also be applicable to other desert regions such as the desert southwest of the United States. During the spring and summer, dry lines typically form in this region, and once formed, act to organize lines of convection that often become severe. It seems possible, based on the arguments presented here,

that the dry lines might be caused by symmetric inertially unstable circulations forming as a result of the destruction of potential vorticity by diabatic heating over the desert southwest. However, at these latitudes  $f$  is much larger and the initial potential vorticity will have to be very low for the diabatic processes to destroy the positive potential vorticity completely. A description of the typical synoptic-scale thermodynamic and kinematic structure in the lower troposphere at the times when dry lines form would be needed to make an estimate of the destruction of potential vorticity by diabatic processes.

Table 1. GATE ships and their positions during Phase III.

Ship	Position (latitude°N-longitude°W)		Country
<i>Researcher</i>	7.1	23.5	U.S.
<i>Dallas</i>	8.5	22.5	"
<i>Gilliss</i>	9.3	24.8	"
<i>Oceanographer</i>	7.8	22.2	"
<i>Vanguard</i>	10.0	23.5	"
<i>Quadra</i>	8.9	22.5	Canada
<i>Prof. Vize</i>	8.4	23.5	USSR
<i>Akad. Korolov</i>	11.9	23.4	"
<i>Poryv</i>	10.5	19.9	"
<i>Ernst Krenkel</i>	6.4	19.8	"
<i>Prof. Zubov</i>	4.9	23.4	"
<i>Okean</i>	6.4	26.9	"
<i>Priboy</i>	10.5	27.0	"
<i>Meteor</i>	8.5	23.5	Federal Republic of Germany (FRG)
<i>Bidassoa</i>	7.7	24.7	France

Table 2. Wave disturbances passing through center of the B-scale Array.  
during Phase III (from Thompson *et al.*, 1979).

<u>Wave</u>	<u>Time and Date of trough passage at 8.5°N, 23.5°W</u>	
1	15 GMT	2 September 1974 (Julian Day:245)
2	00 GMT	6 September 1974 (Julian Day:249)
3	15 GMT	9 September 1974 (Julian Day:252)
4	18 GMT	13 September 1974 (Julian Day:256)
5	21 GMT	16 September 1974 (Julian Day:259)

Table 3. Characteristics of the monsoon trough bands.

Wave	1	2	3	4	5
length (km)	650	400	400	450	550
width (km)	100	50	60	50	90
orientation from north ( $^{\circ}$ )	40	65	40	70	50
movement from ( $^{\circ}/\text{m s}^{-1}$ )	120/7	135/7	130/7	135/7	120/8
peak rainfall rate ( $\text{mm h}^{-1}$ )	60	55	50	50	55
maximum echo tops (km)	13	13	12	13	13

Table 4. Characteristics of the squall line events.

Squall	1	2	3
Time visible (Julian Day/GMT)	247/09- 248/03	254/18- 255/00	255/11- 255/20
length(km)	280	270	300
width of active region(km)	35	30	30
width of trailing precipitation(km)	300	300	300
orientation from north( $^{\circ}$ )	140	135	140
movement from ( $^{\circ}/m\ s^{-1}$ )	050/11	045/18	050/14
maximum echo height(km)	17	14	15
maximum rainfall rate( $mm\ h^{-1}$ )	70	65	70

Table 5. Characteristics of the long narrow lines.

wave	1	2	3	4	5
number of lines	5	1	1	1*,4	2
length(km)	400-850	1000	420	400-600	450,600
width(km)	5-30	35	35	35,25	35
orientation from north(°)	305	280	280	300,305	270
movement from (°/m s <sup>-1</sup> )	035/6	010/6	355/5	030/6	035/5
line spacing(km)	90	-	-	110	120
peak rainfall rate(mm h <sup>-1</sup> )	25,45	30,45	25,40	25,40	30,45
maximum echo tops(km)	5,12	5,13	4,10	4,11	5,12

\* line ahead of 12 September squall line.

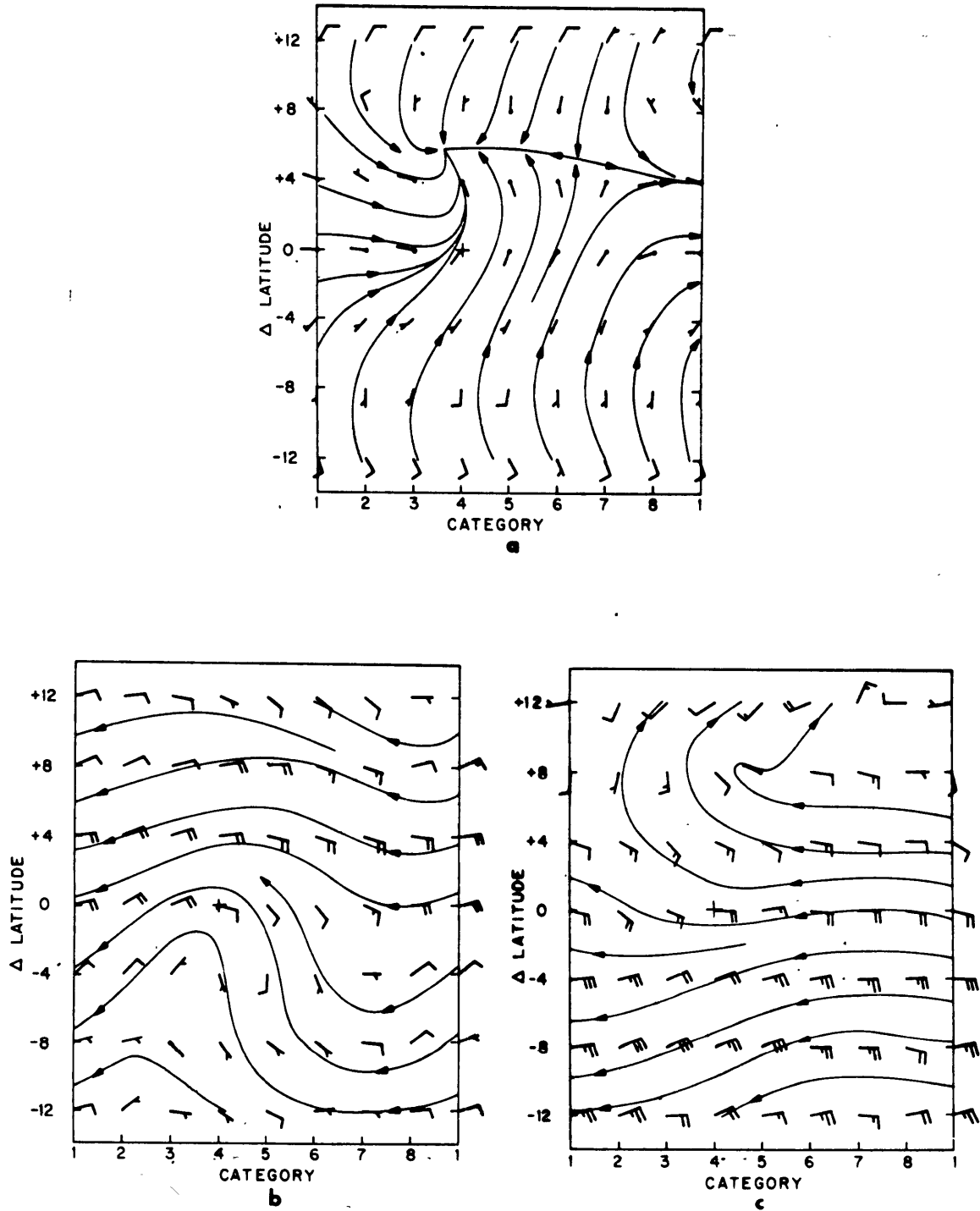


Fig. 1. Streamlines of the total wind field in the composite wave for Phase III and the preceding interphase period. Category separation is approximately 3 degrees longitude. Cross denotes disturbance center at 700 mb. "Zero" latitude corresponds to the average latitude of the disturbance path,  $11^{\circ}\text{N}$  over land and  $12^{\circ}\text{N}$  over ocean. Positive  $\Delta$ -latitude is north and negative south. One full barb corresponds to  $5 \text{ m s}^{-1}$ , one half barb to  $2.5 \text{ m s}^{-1}$ , and no barb to  $1 \text{ m s}^{-1}$ . (a) Surface, (b) 700 mb, (c) 200 mb (from Reed, *et al.*, 1977).

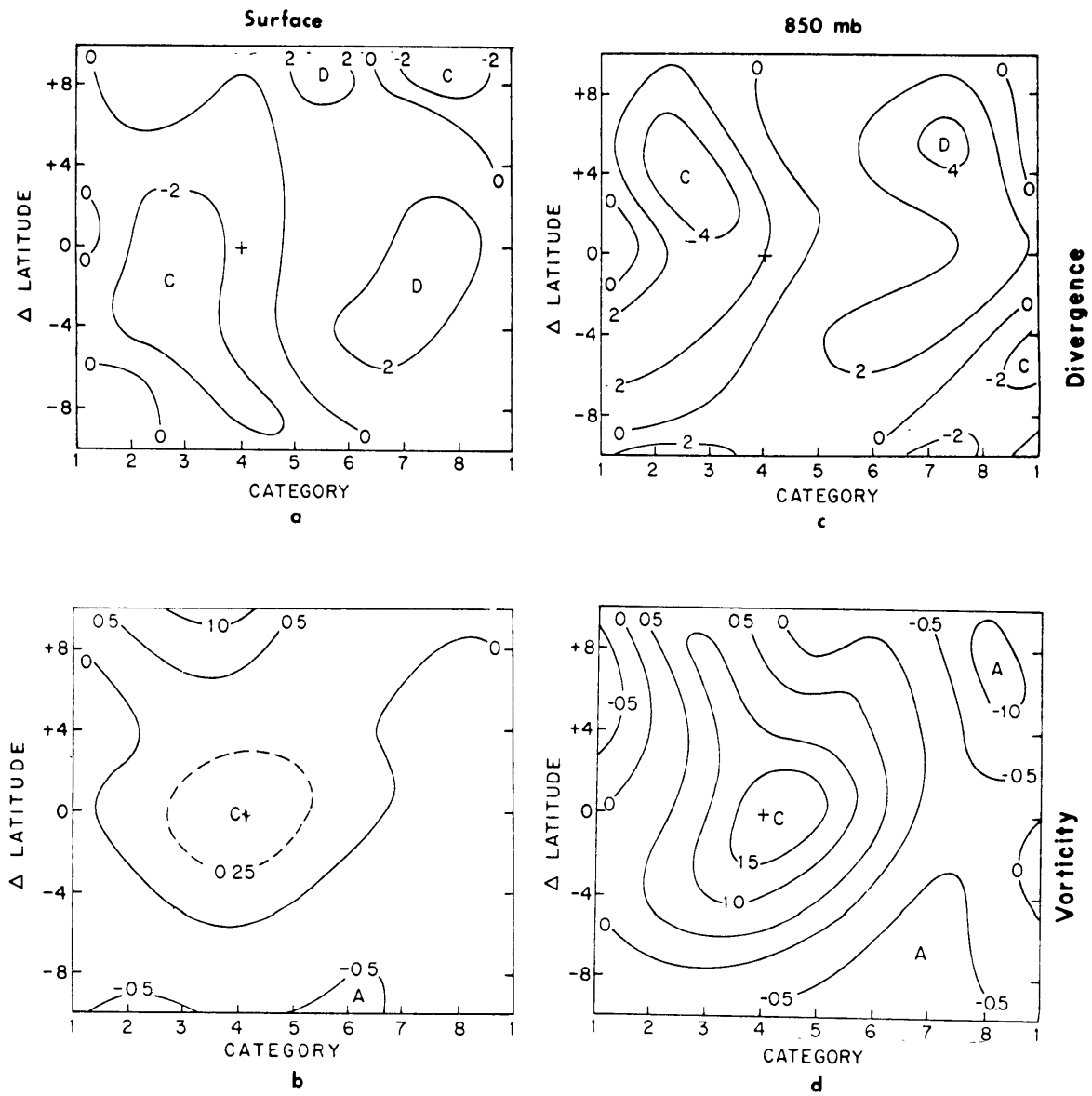


Fig. 2. Divergence deviation from zonal means in units of  $10^{-6} \text{ s}^{-1}$ : (a) Surface and (c) 850 mb. Vorticity in units of  $10^{-5} \text{ s}^{-1}$ : (b) Surface and (d) 850 mb. See Fig. 1 for further description (from Reed, *et al.*, 1977).

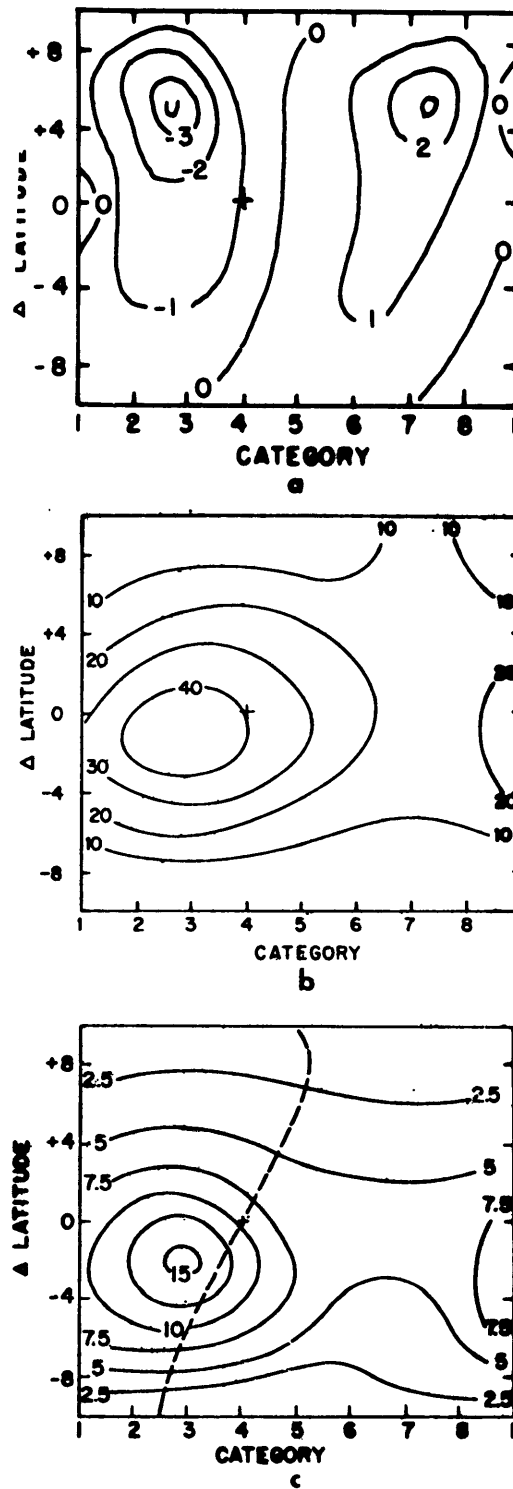


Fig. 3. (a) Vertical motion deviation ( $\text{mb h}^{-1}$ ) from zonal mean at 850 mb for the composite wave (from Reed, *et al.*, 1977). (b) Percentage cover by convective cloud defined as white appearing cloud in satellite infrared images at various positions in the composite wave (from Payne and McGarry, 1977). (c) Average precipitation rate ( $\text{mm day}^{-1}$ ) for the composite wave taken from 6-hourly ship amounts and daily totals for selected land stations. Dashed line is trough axis at 700 mb (from Reed, 1978).

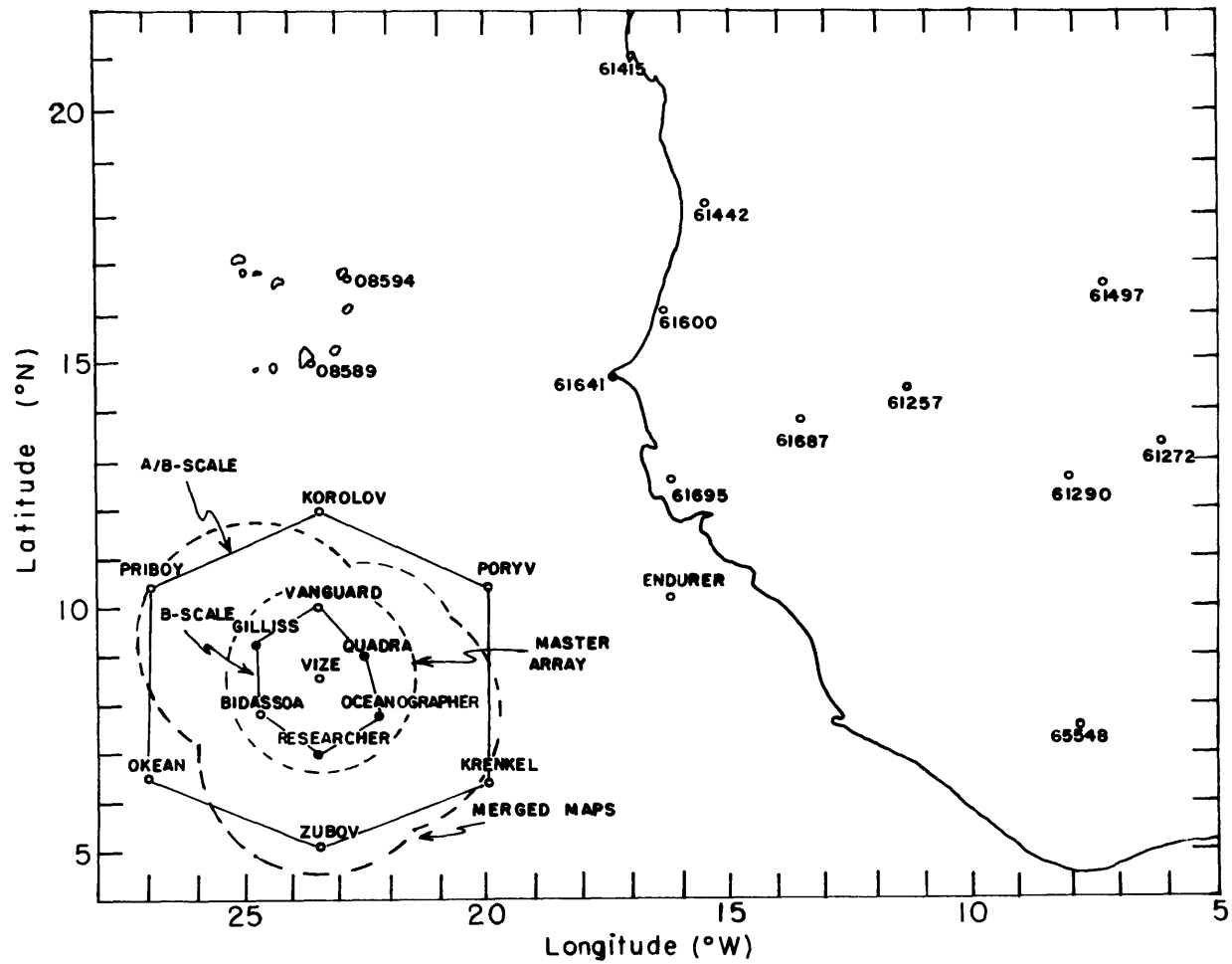


Fig. 4. GATE ship arrays and selected land stations for Phase III. Area covered by merged radar maps and the Master Array are as indicated. The ships marked with an "X" had the C-band radars.

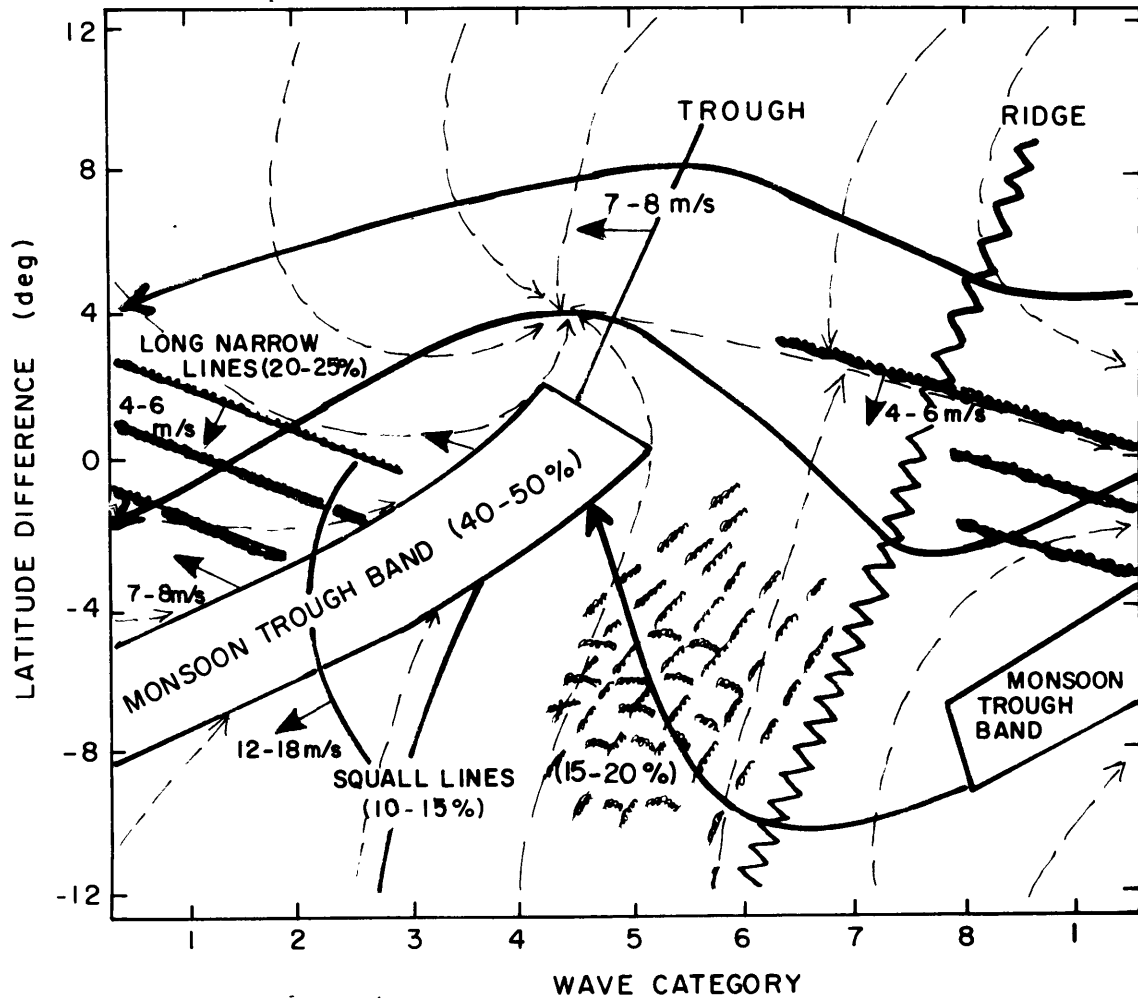


Fig. 5. Schematic diagram of precipitation features in the wave. Arrows and speeds indicate typical motion of features. Dashed and heavy solid lines indicate surface and 700 mb streamlines, respectively. Percent of total precipitation is indicated for each feature. Wave category and  $\Delta$ -latitude is as defined in Fig. 1.

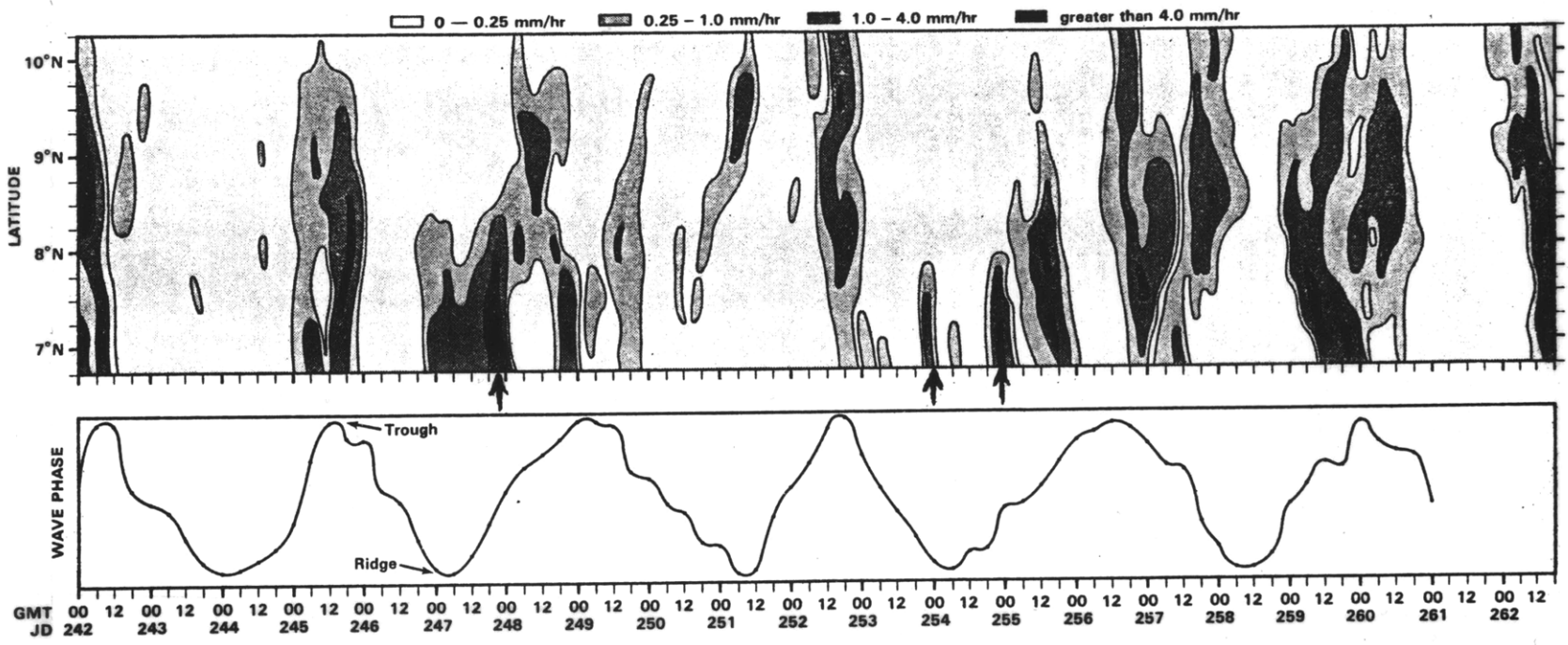


Fig. 6. Time-latitude cross-section of precipitation for Phase III through center of B-scale array (upper) and time series of the wave category at the center of the B-scale array (lower). Contoured precipitation rates ( $\text{mm h}^{-1}$ ) are drawn from 3 h averages over  $0.5 \times 0.5$  degree lat.-long. squares. The three squall line events are indicated by the heavy arrows.

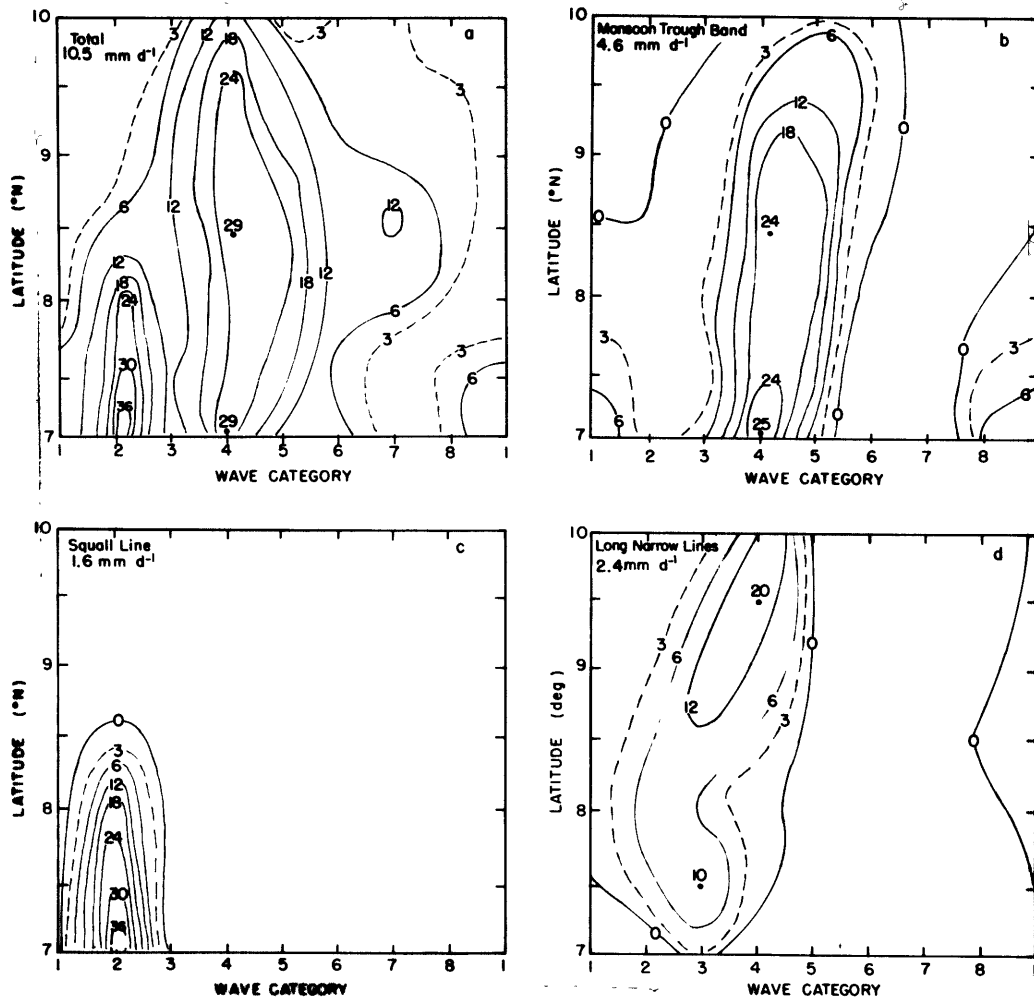


Fig. 7. Radar precipitation analyses over Master Array for Phase III ( $\text{mm day}^{-1}$ ). (a) total, (b) Monsoon trough bands, (c) Squall lines, (d) Long narrow lines. Wave category is defined as in Fig. 1 and the ordinate is latitude within the bounds of the Master Array. The latitude resolution is 0.5 degrees, the width of a wave category about 3.0 degrees, and each element of the precipitation analysis covers an area of about  $1.5 \times 10^3 \text{ km}^2$ .



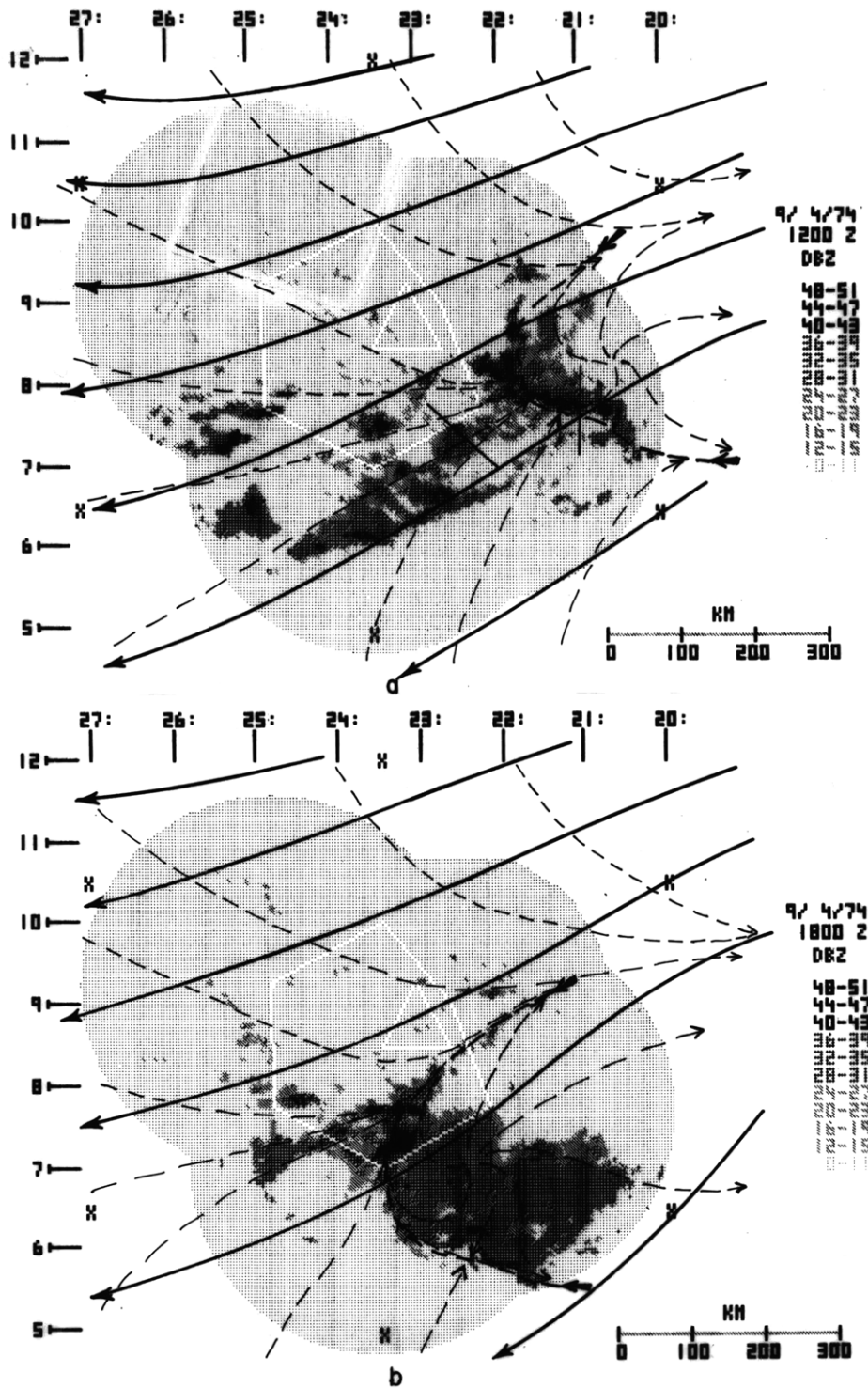


Fig. 9. Merged radar maps together with surface and 700-mb streamlines for (a) 1200 GMT and (b) 1800 GMT, 4 September 1974. See Fig. 7 for further description. Light solid lines in (a) denote position of cross-sections in Fig. 10.

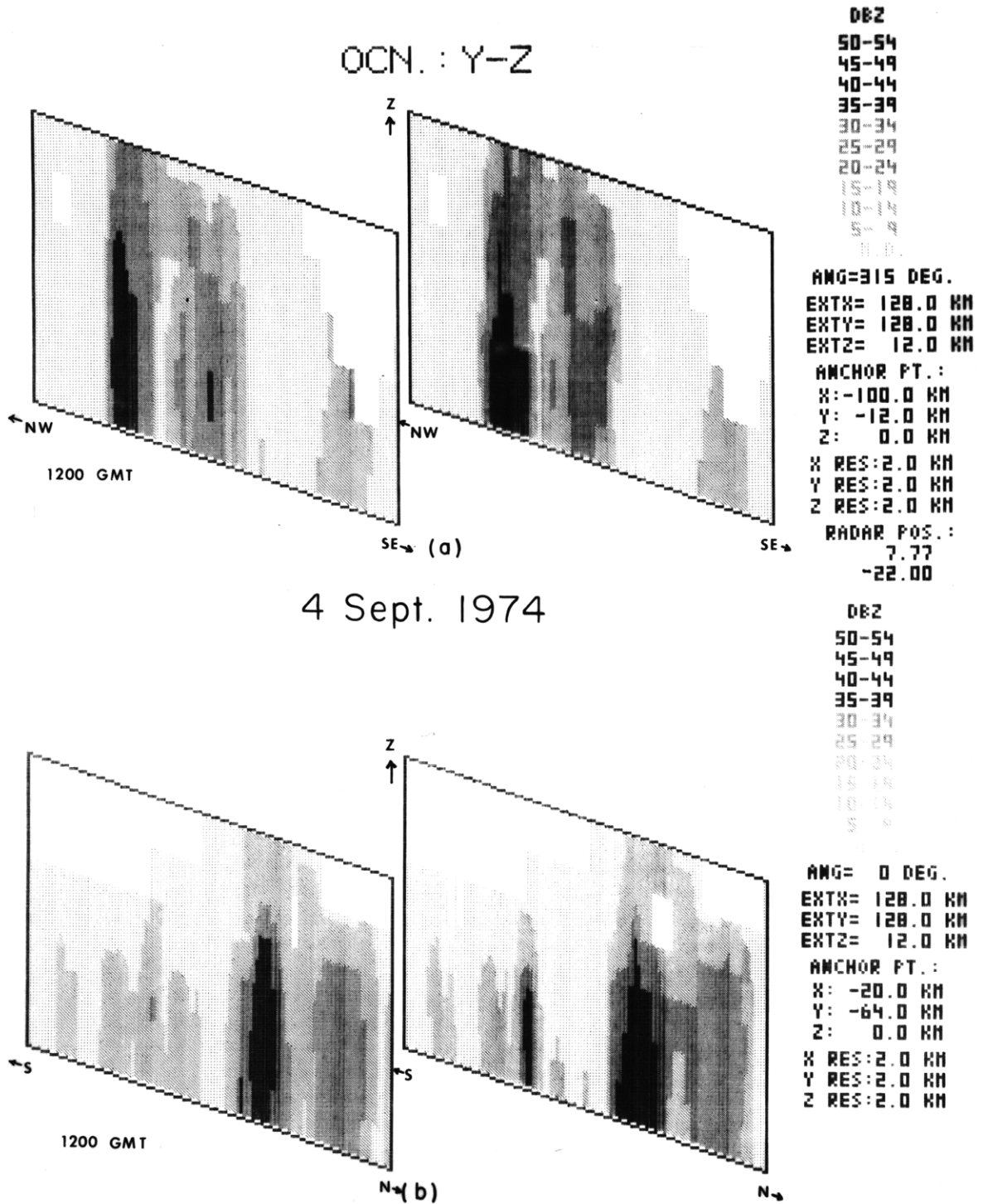


Fig. 10. Vertical cross-sections of radar reflectivity factor (dBZ) from Oceanographer radar at locations in Fig. 9 a for (a) monsoon trough band and (b) squall line at 1200 GMT, 4 September 1974. Vertical and horizontal extent of cross-sections is 12 km and 128 km, respectively. Y-axis is oriented 315 deg. in (a) and 0 deg. in (b).

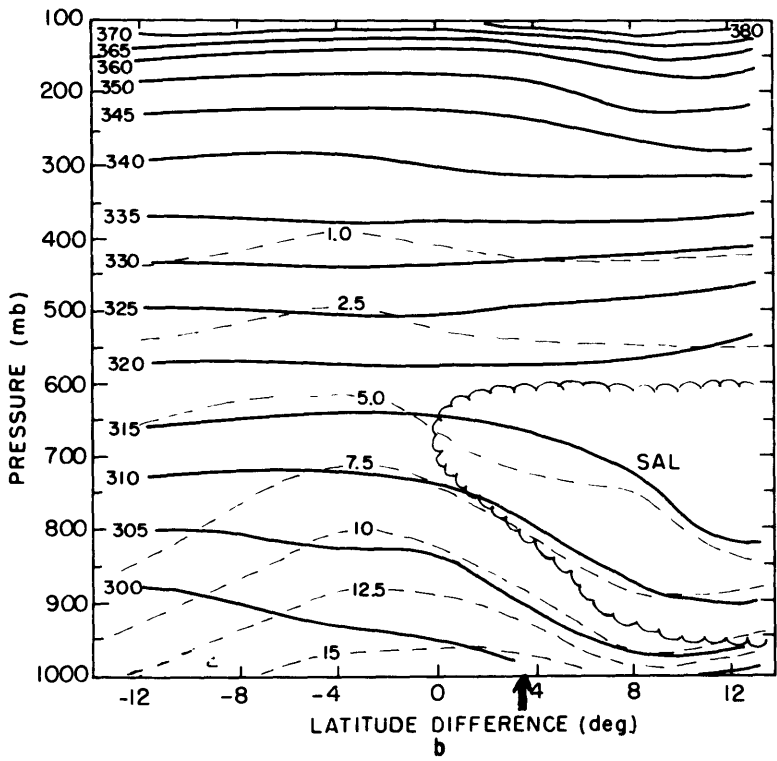
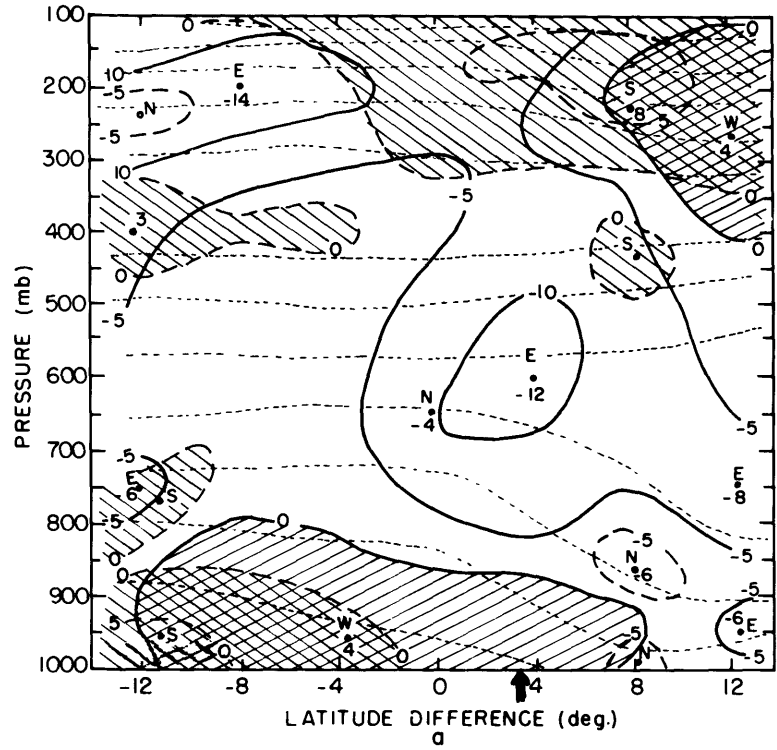


Fig. 11. North-south vertical cross-sections of (a) zonal and meridional wind ( $\text{m s}^{-1}$ ) and (b) potential temperature and mixing ratio ( $\text{K}$  and  $\text{g kg}^{-1}$ ) for wave ridge. In (a), the heavy solid and dashed lines indicate zonal and meridional wind, respectively, and light dashed lines, potential temperature. Right and left hatching indicate westerly zonal or southerly meridional wind components, respectively. In (b), solid and dashed lines indicate potential temperature and mixing ratio, respectively. Scalloped line indicates the boundary of the SAL.  $\Delta$ -latitude is as defined in Fig. 1. Heavy arrows indicate typical position of long narrow convective lines.

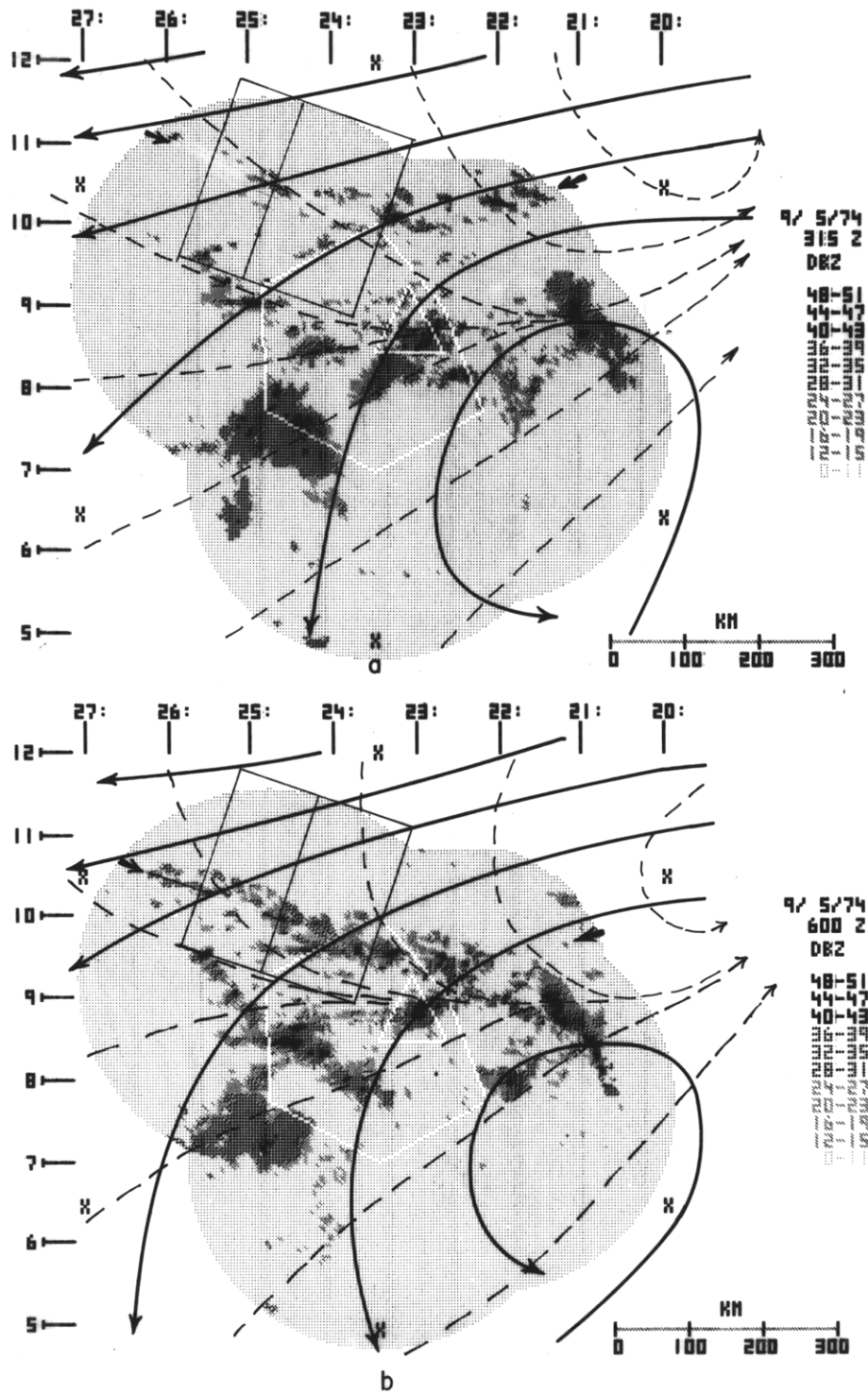


Fig. 12. Merged radar maps together with surface and 700-mb streamlines for (a) 0315 GMT and (b) 0600 GMT, 5 September 1974. Regions selected for three-dimensional analyses are indicated by light lines. See Fig. 7 for further description.

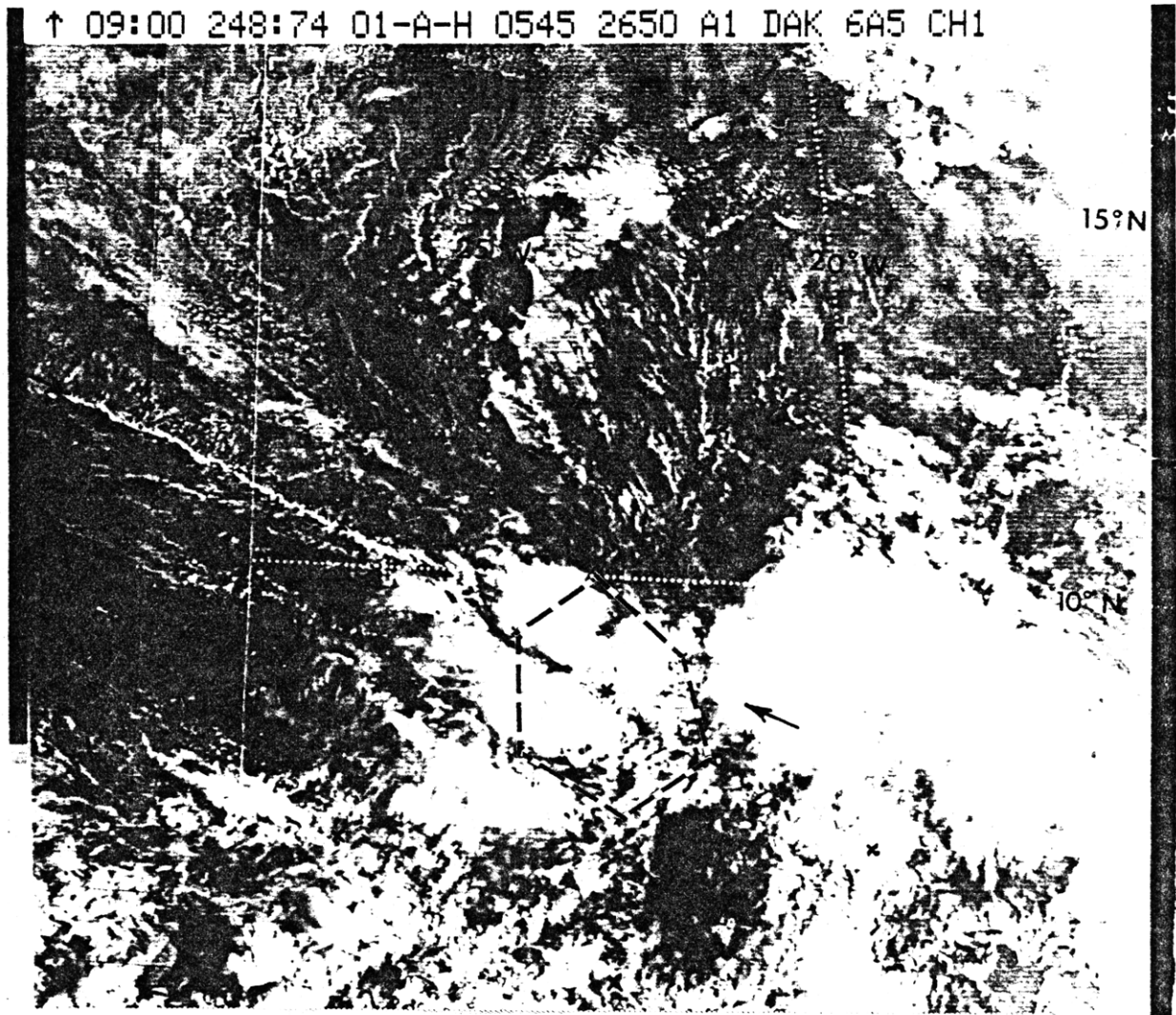


Fig. 13. (a) Visible SMS-I satellite image for 0900 GMT, 5 September 1974. The convective line is denoted by arrows. "x" indicates the location of the A/B-scale ships and the B-scale array is outlined. The coast of Africa is outlined on the grid and the dust plume labelled. (b) Merged radar map together with surface and 700-mb streamlines for 0900 GMT, 5 September 1974. See Fig. 7 for further description.

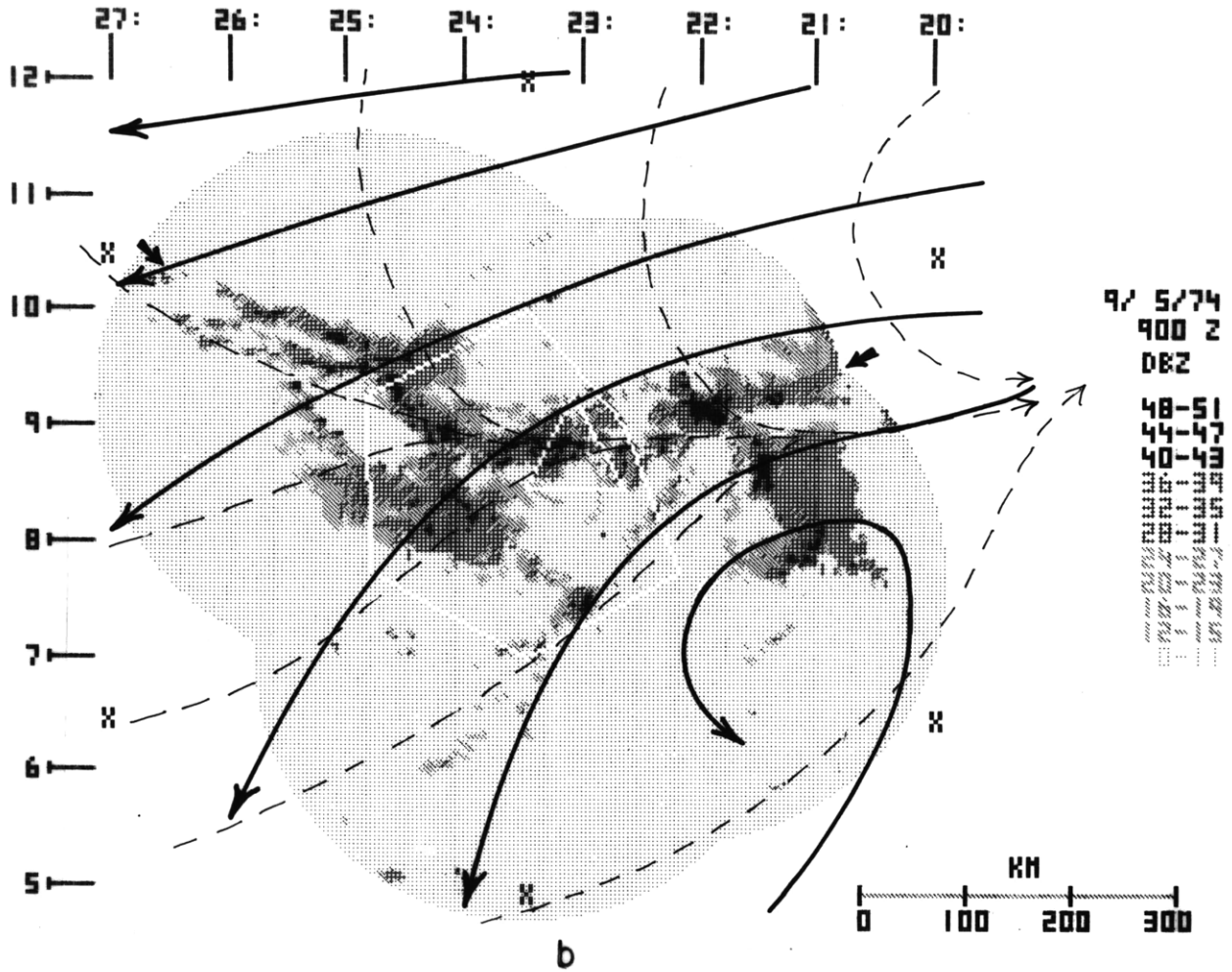


Fig. 13. (continued)

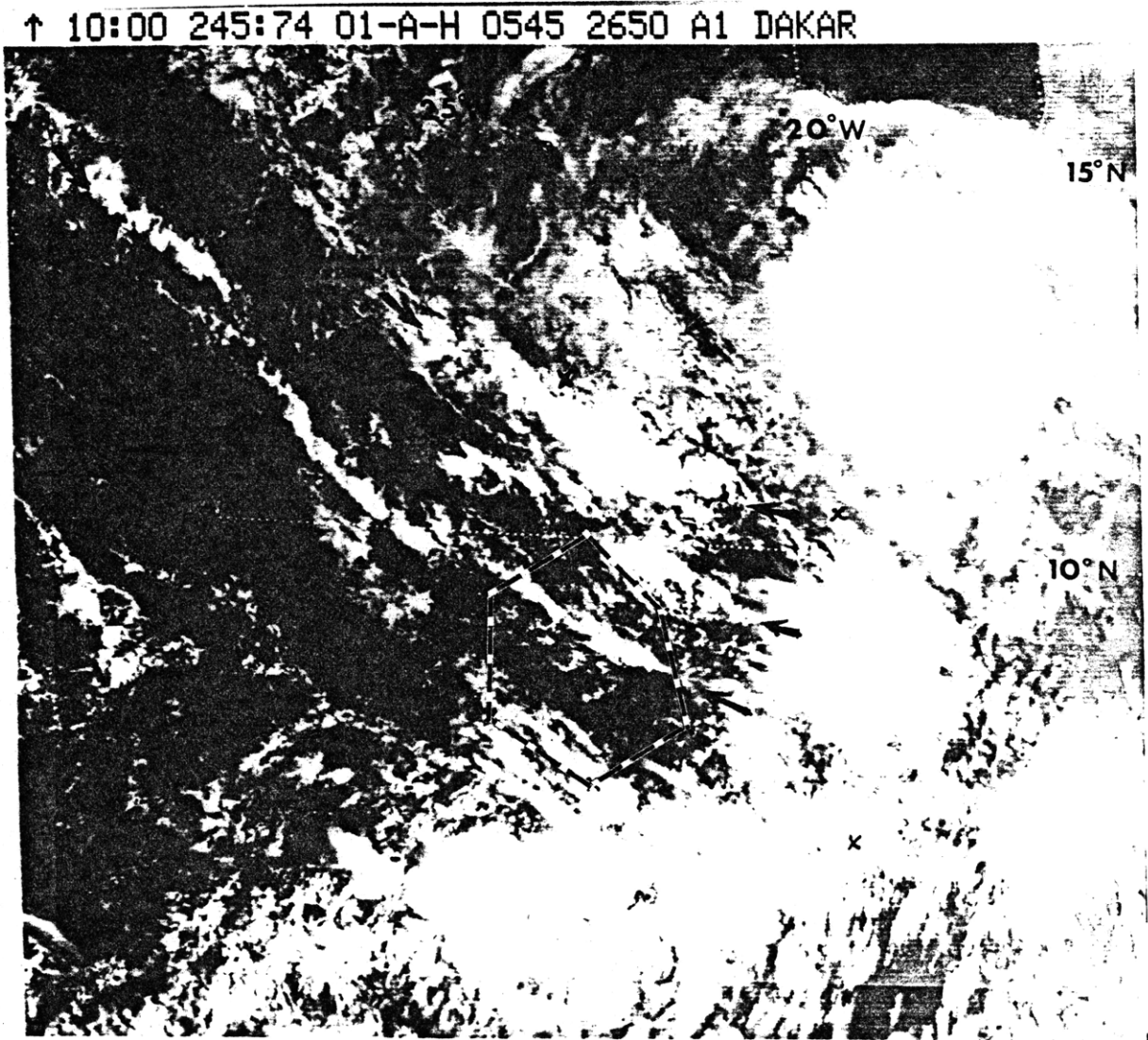
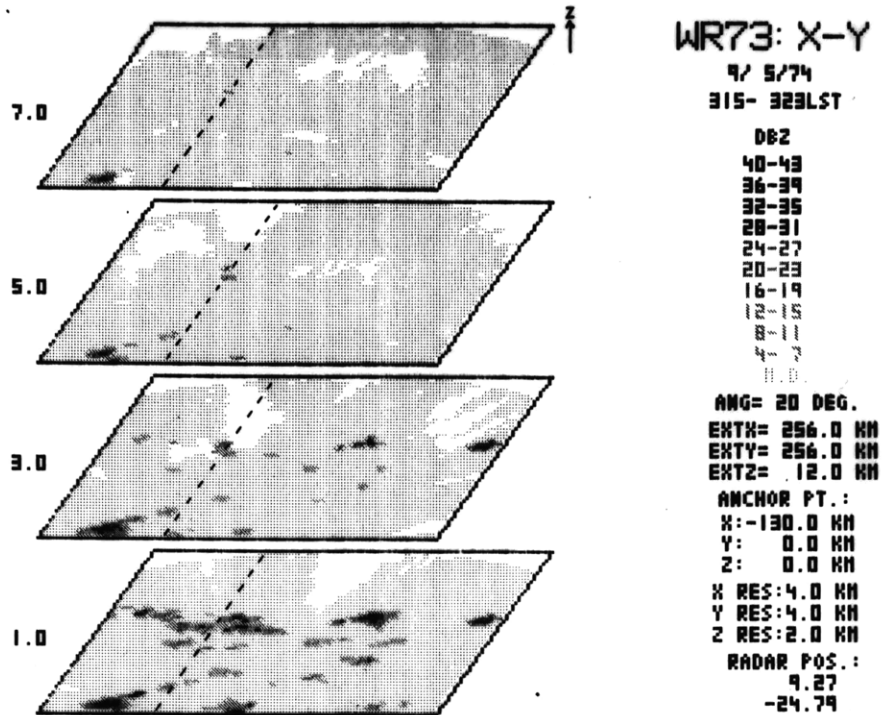
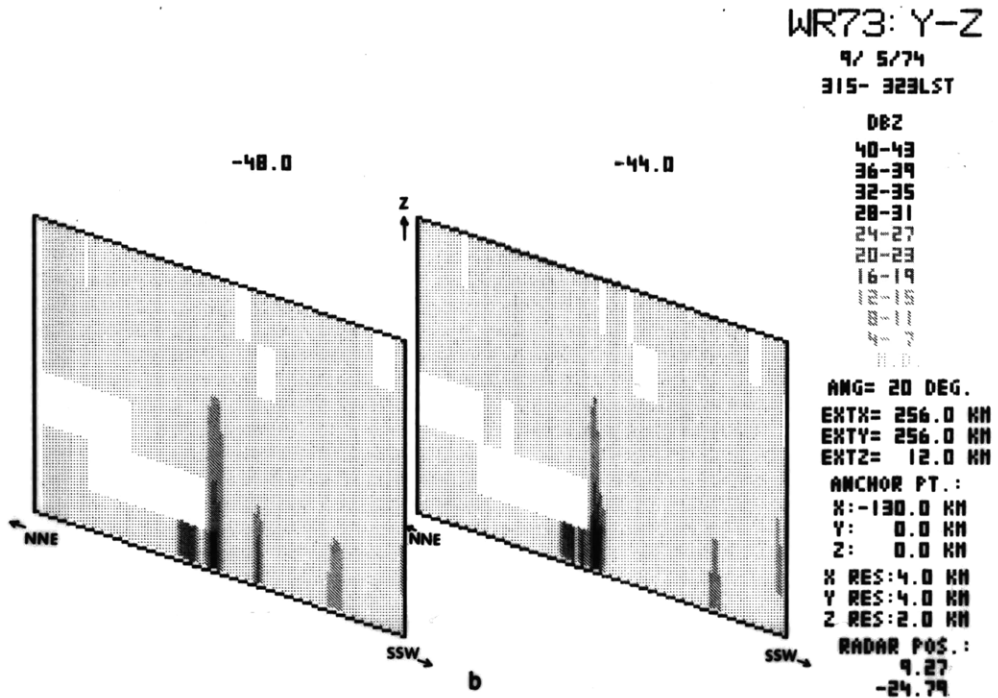


Fig. 14. Visible SMS-1 satellite image for 1000 GMT, 2 September 1974. See Fig. 13 a for further description.

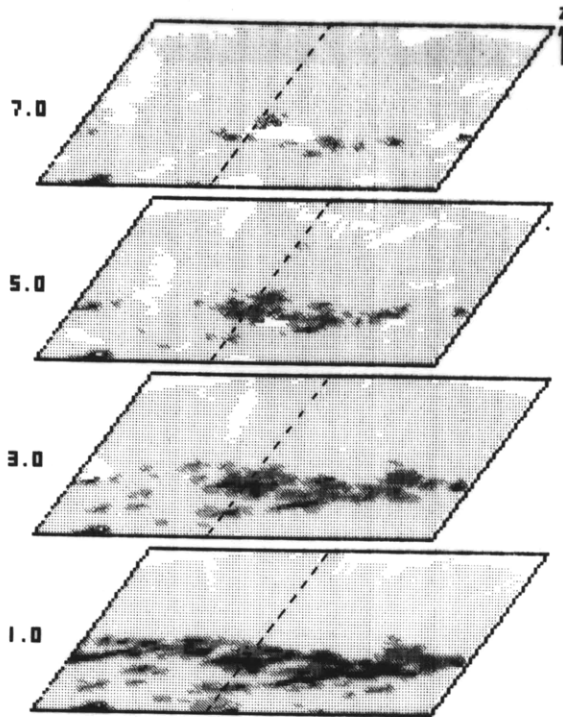


a



b

Fig. 15. Three-dimensional cross-sections of radar reflectivity factor (dBZ) corresponding to regions outlined in Fig. 12. (a) and (b) for 0315 GMT and (c) and (d) for 0601 GMT, 5 september 1974. (a) and (c) are stacks of X - Y planes parallel to the earth's surface, 256 km on a side, at heights (km) indicated to the left of each plane. The positive y and x-axis are into the page and to the right. Dashed lines indicate position of Y - Z slices shown in (b) and (d). Y - Z slices are 12 km high and 256 km long.



WR73: X-Y

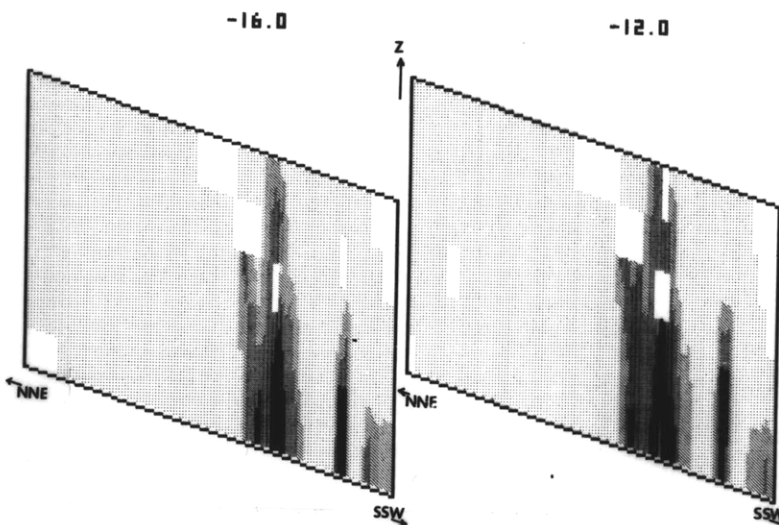
9/ 5/74  
601- 604LST

DBZ  
40-43  
36-39  
32-35  
28-31  
24-27  
20-23  
16-19  
12-15  
8-11  
4-7  
0-3

ANG= 20 DEG.  
EXTX= 256.0 KM  
EXTY= 256.0 KM  
EXTZ= 12.0 KM

ANCHOR PT. :  
X: -130.0 KM  
Y: 0.0 KM  
Z: 0.0 KM  
X RES: 4.0 KM  
Y RES: 4.0 KM  
Z RES: 2.0 KM  
RADAR POS. :  
9.25  
-24.76

c



WR73: Y-Z

9/ 5/74  
601- 604LST

DBZ  
40-43  
36-39  
32-35  
28-31  
24-27  
20-23  
16-19  
12-15  
8-11  
4-7  
0-3

ANG= 20 DEG.  
EXTX= 256.0 KM  
EXTY= 256.0 KM  
EXTZ= 12.0 KM

ANCHOR PT. :  
X: -130.0 KM  
Y: 0.0 KM  
Z: 0.0 KM  
X RES: 4.0 KM  
Y RES: 4.0 KM  
Z RES: 2.0 KM  
RADAR POS. :  
9.25  
-24.76

d

Fig. 15. (continued)

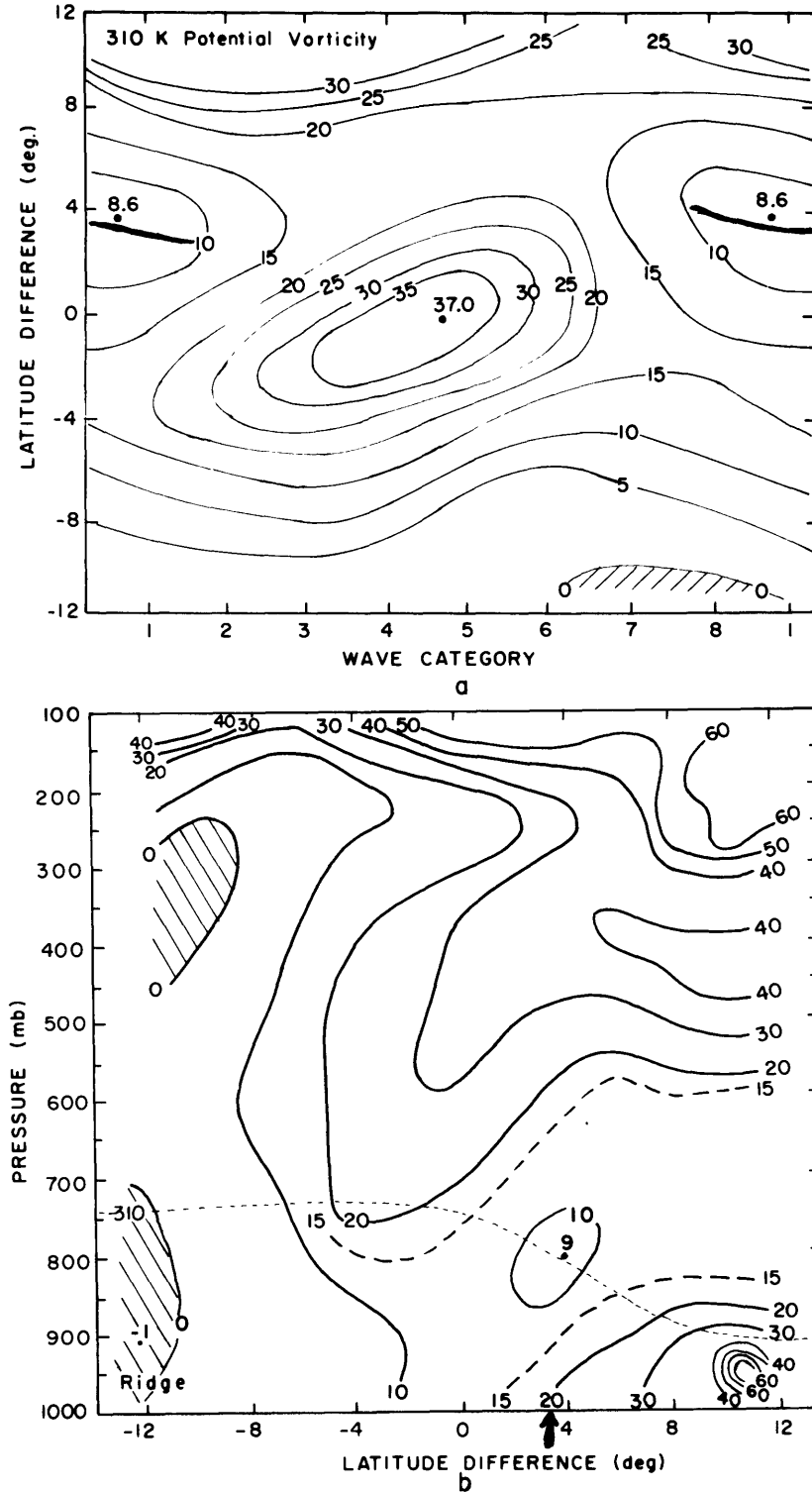


Fig. 16. Potential vorticity as defined by (3.4) divided by  $g$  ( $10^{-7} \text{ K mb}^{-1} \text{ s}^{-1}$ ) for the (a) 310 K isentropic surface, and (b) vertical cross-section of the wave ridge. Negative values are hatched. Wave categories and  $\Delta$ -latitude are as defined in Fig. 1. Solid lines in (a) and heavy arrow in (b) depict the positions where the long narrow convective lines typically occur.

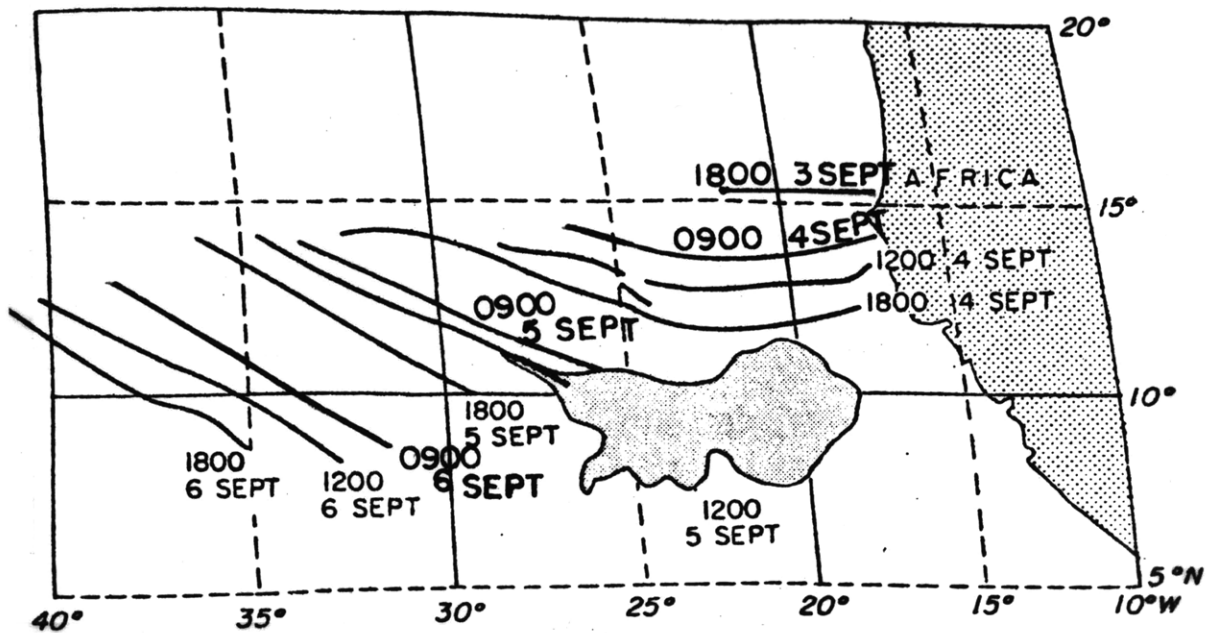


Fig. 17. Isochrones of the convective line position as obtained from SMS-1 visible satellite images. Shaded region at 1200 GMT, 5 September shows outline of the convective cloud in the monsoon trough zone from the visible SMS-1 image.

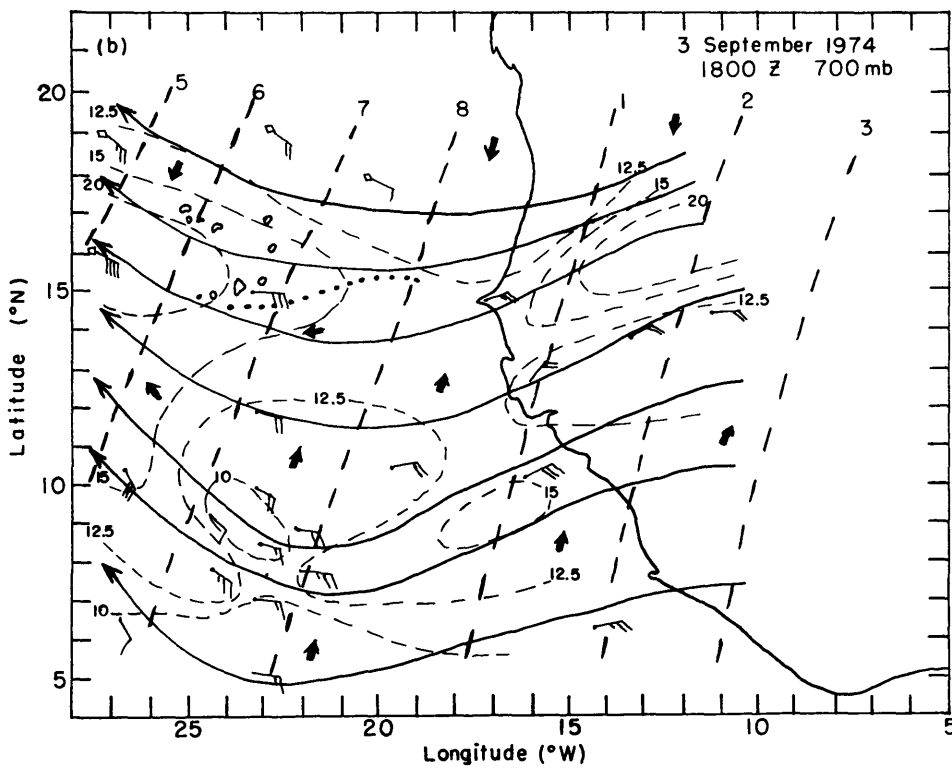
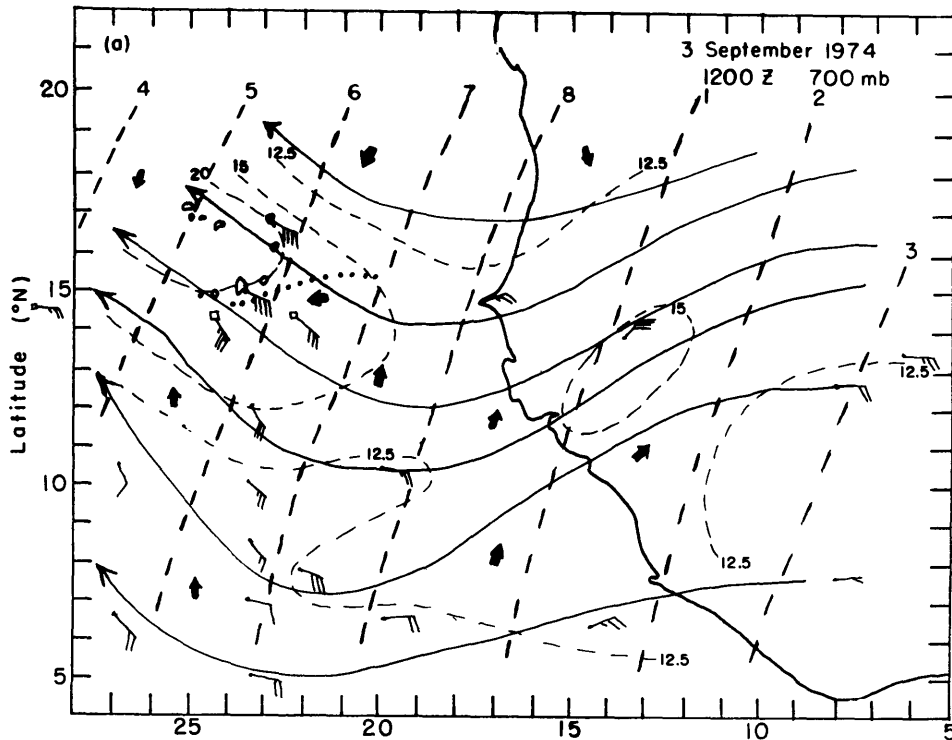


Fig. 18. 700-mb streamline analyses for (a) 1200 GMT and (b) 1800 GMT, 3 September, (c) 0000 GMT, (d) 0600 GMT, (e) 1200 GMT, and (f) 1800 GMT, 4 September, and (g) 0000 GMT and (h) 0600 GMT, 5 September 1974. Light dashed and solid lines denote the 700-mb isotachs and streamlines, respectively. The solid arrows depict the surface wind direction and the barbs the 700-mb winds. One full barb corresponds to  $5 \text{ m s}^{-1}$ , one half barb to  $2.5 \text{ m s}^{-1}$ , and no barb to  $1 \text{ m s}^{-1}$ . Squares denote the position of dropwinsonde winds. The convective line position is depicted by the heavy dotted line, and the heavy solid line in (c - g) represents the squall line position. The wave category (1 - 8) is indicated by the heavy dashed lines.

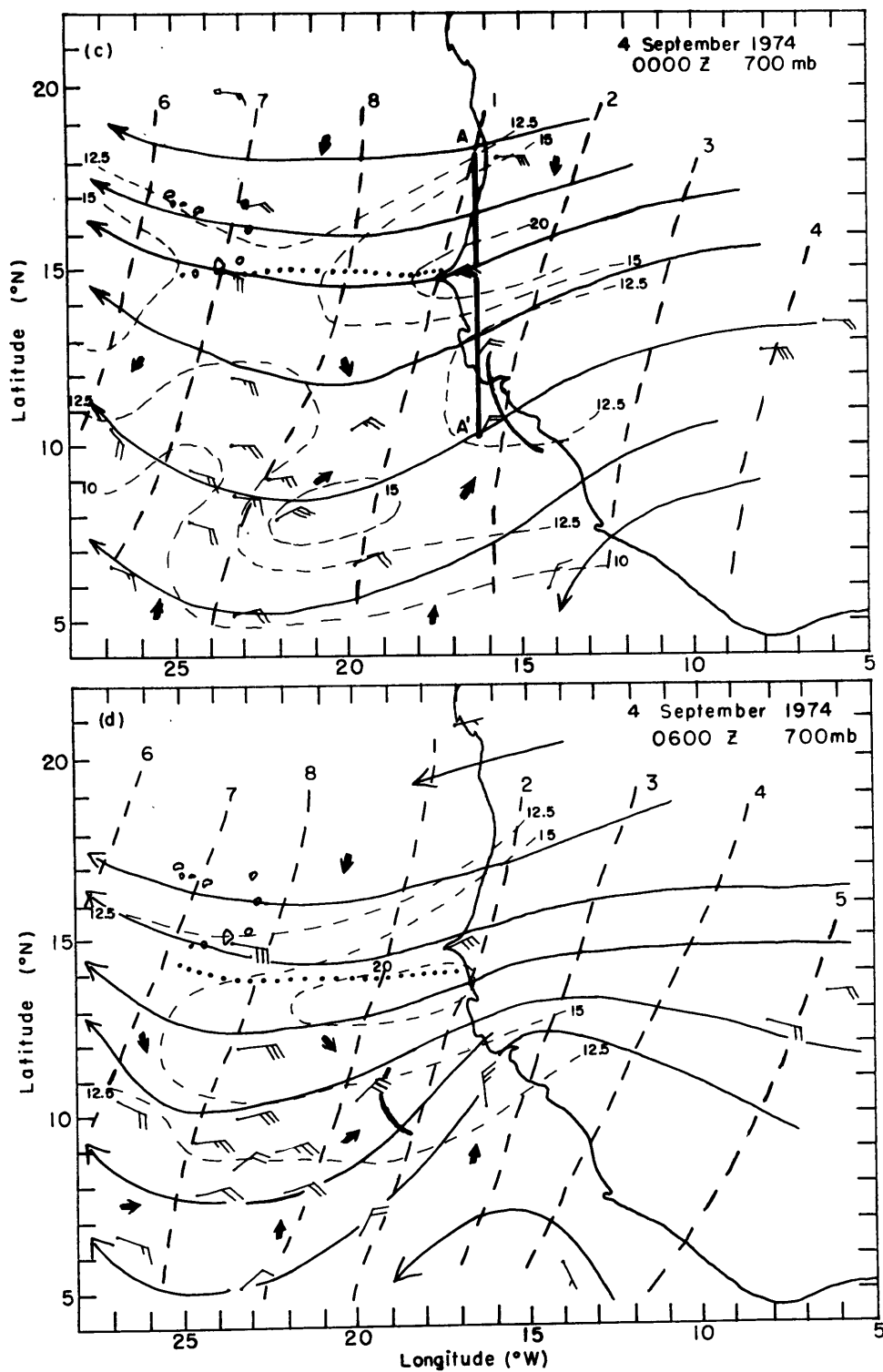


Fig. 18. (continued)

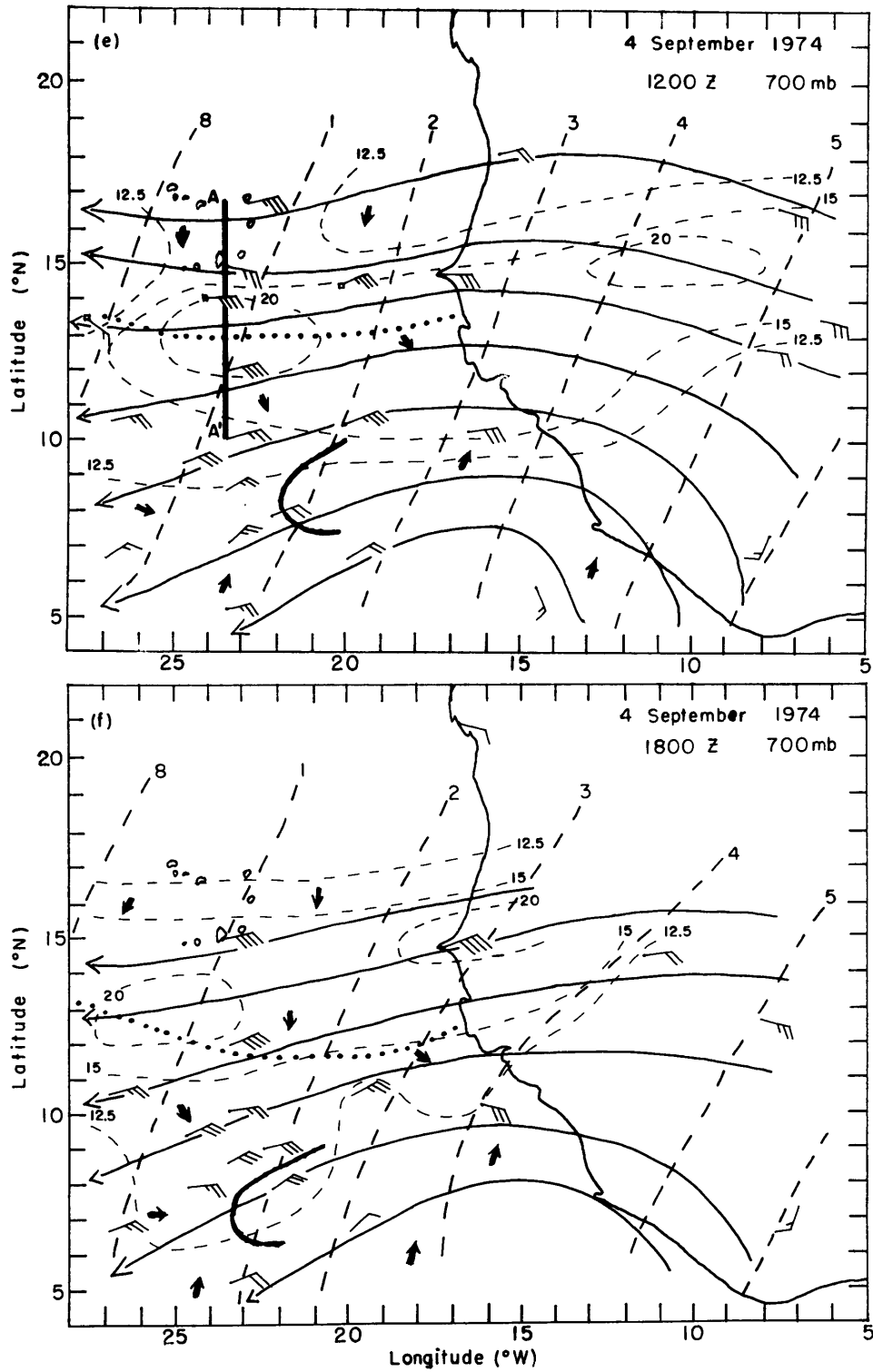


Fig. 18. (continued)

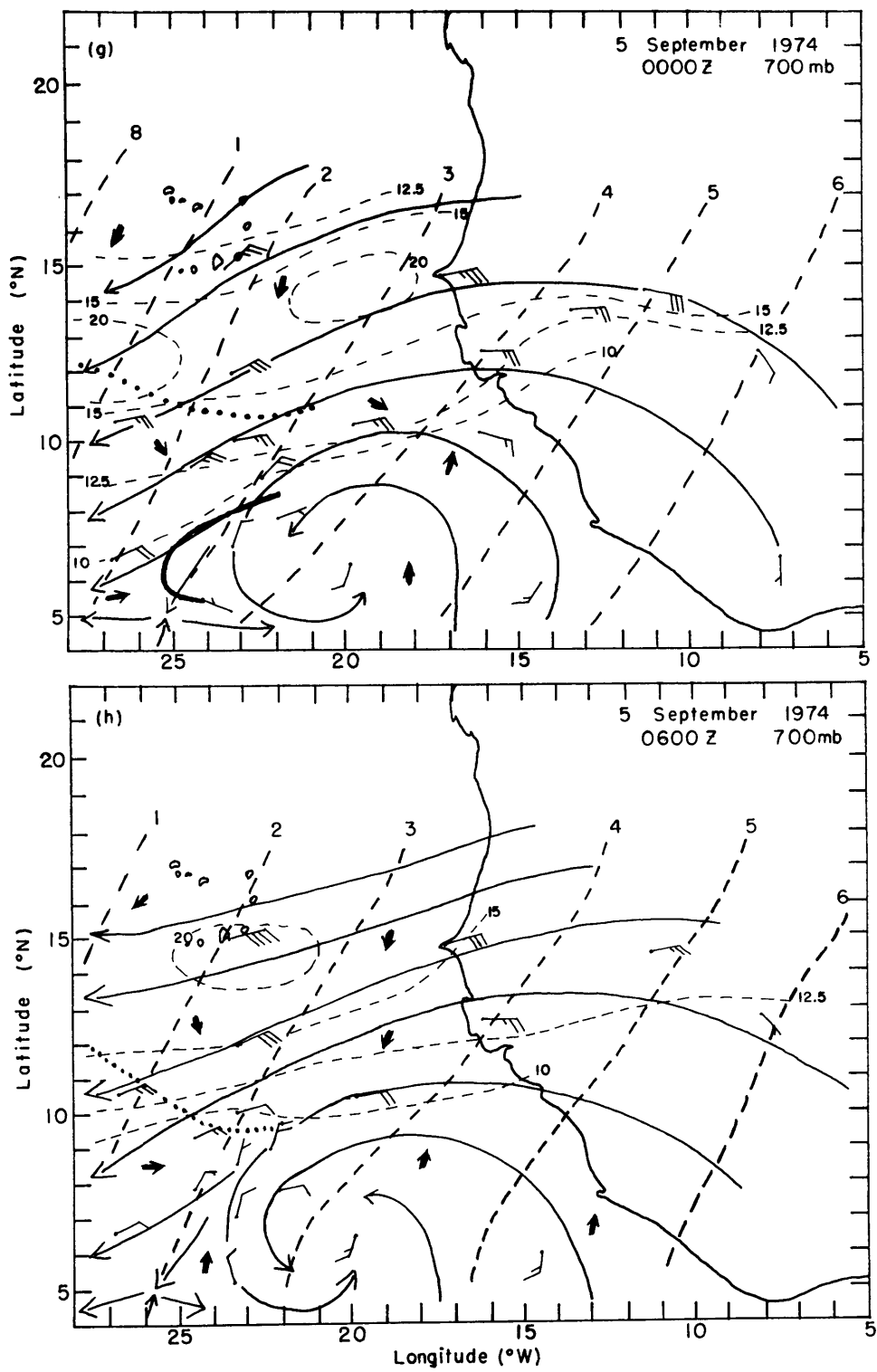


Fig. 18. (continued)



Fig. 19. Visible SMS-I satellite image for (a) 1200 GMT and (b) 1800 GMT, 3 September; and (c) 0900 GMT and (d) 1800 GMT, 4 September 1974. See Fig. 13 a for further description.

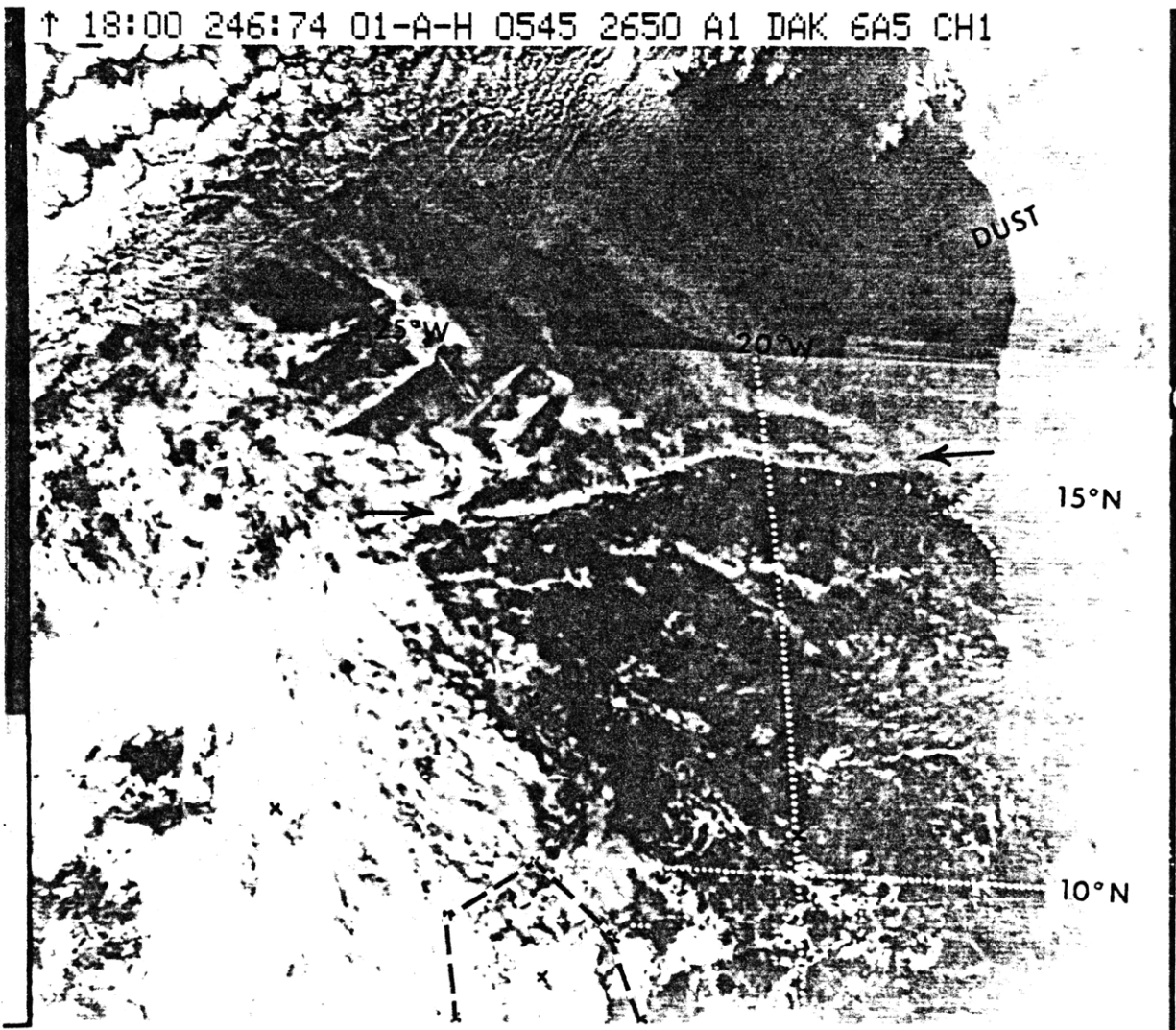


Fig. 19 b

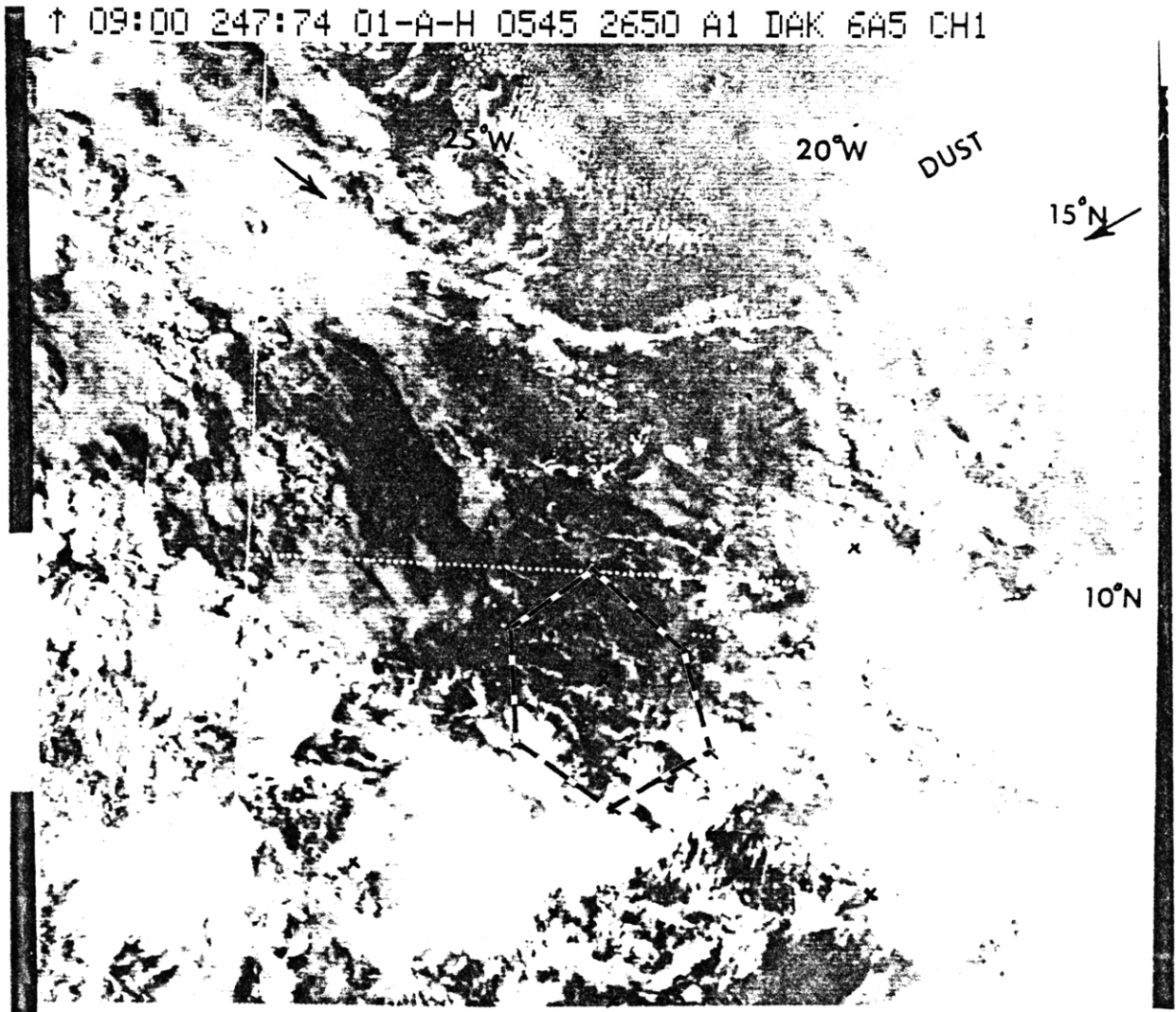


Fig. 19 c

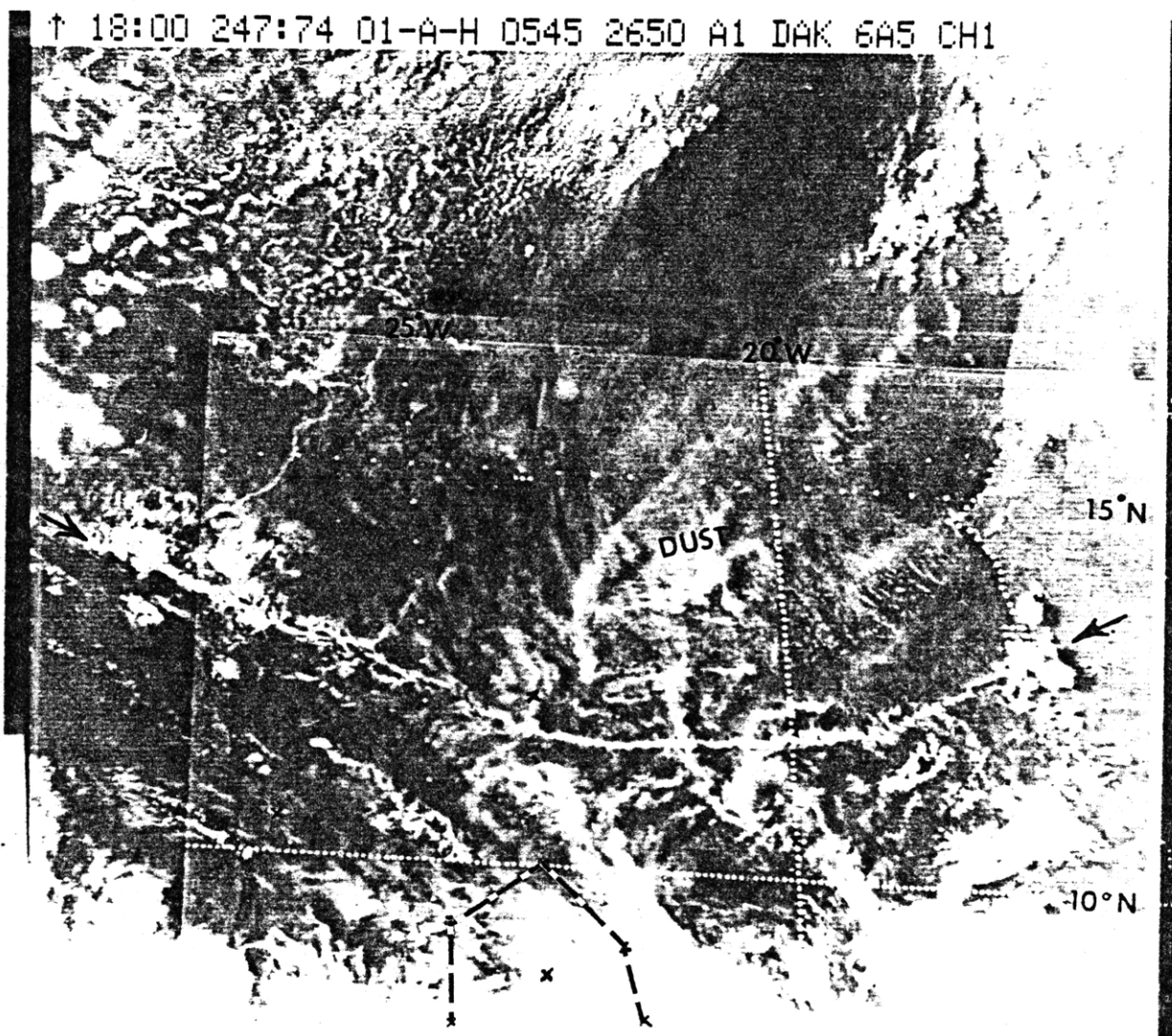


Fig. 19 d

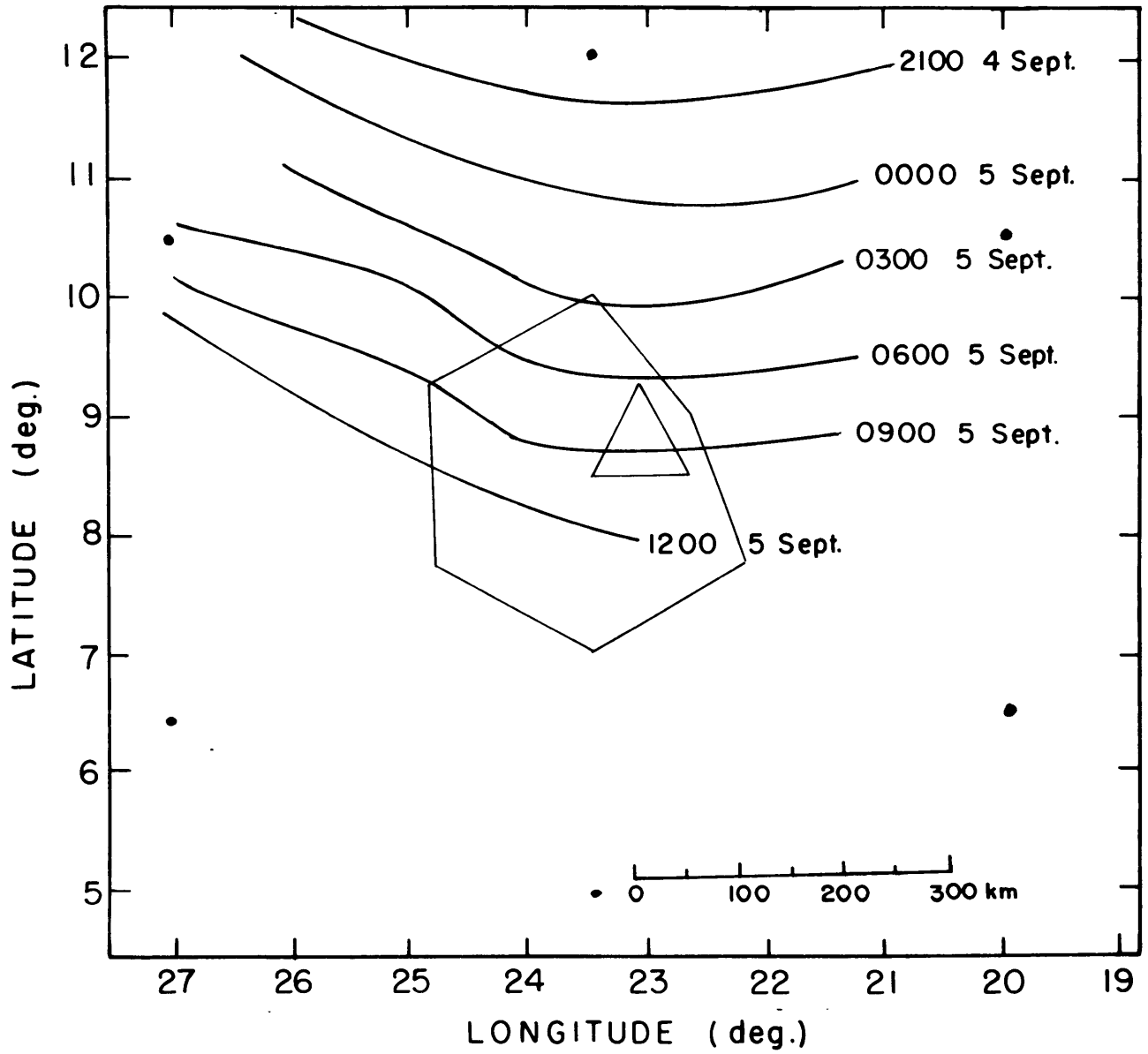


Fig. 23. Isochrones of the convective line position as obtained by merged radar maps. Dots denote A/B-scale ship positions and the B-scale array is outlined.

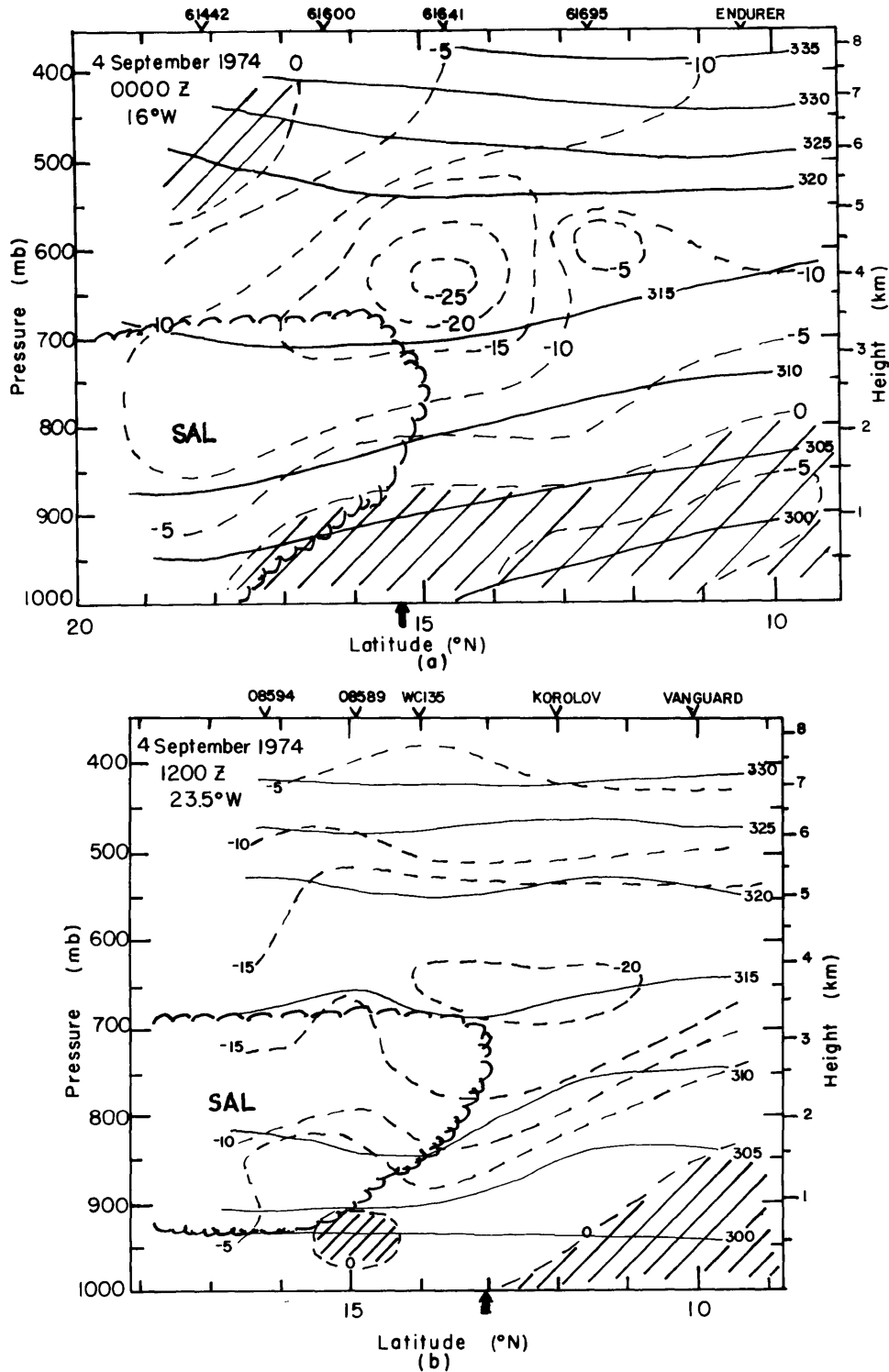


Fig. 21. Cross-sections of zonal wind speed (dashed lines in,  $\text{m s}^{-1}$ ), and potential temperature (solid lines, in K), for (a)  $16^\circ\text{W}$  longitude at 0000 GMT 4 September 1974, and (b)  $23.5^\circ\text{W}$  longitude at 1200 GMT 4 September 1974. Abscissa denotes latitude. Identification and position of the soundings are denoted by marks at the top of each figure. The solid arrows at the base of each figure denote the position of the convective line, and the scalloped line marks the boundary of the SAL.

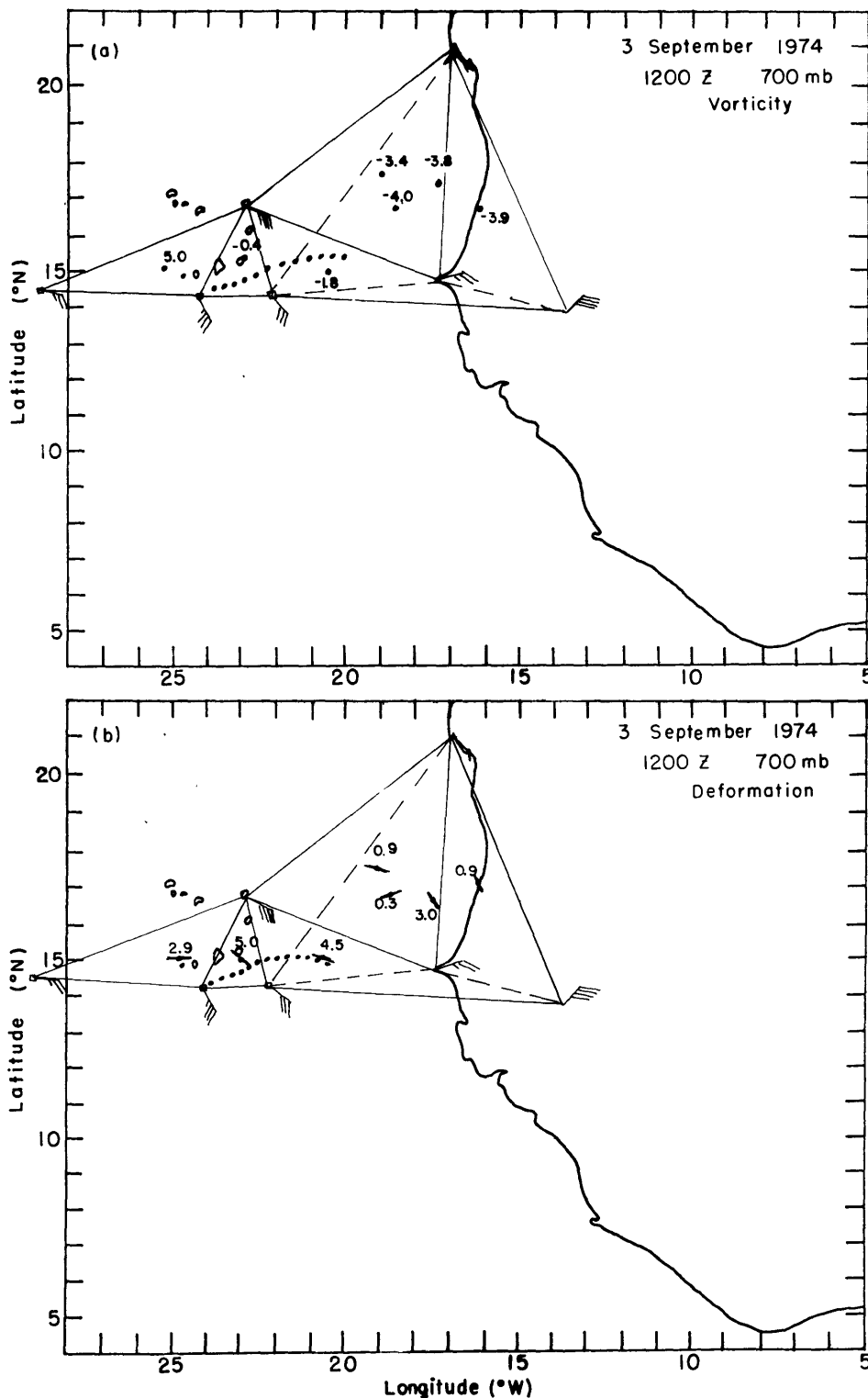


Fig. 22. 700-mb relative vorticity ( $10^{-5} \text{ s}^{-1}$ ) for (a) 1200 GMT, (c) 1800 GMT, 3 September, (e) 0000 GMT, (g) 1200 GMT, 4 September, and (i) 0000 GMT, 5 September 1974. 700-mb resultant deformation ( $10^{-5} \text{ s}^{-1}$ ) and axis of dilatation for (b) 1200 GMT, (d) 1800 GMT, 3 September, (f) 0000 GMT, (h) 1200 GMT, 4 September, and (j) 0000 GMT 5 September 1974. The convective line positions is denoted by the heavy dotted lines and the thin solid and dashed lines outline the triangles used for the computations. The winds are depicted as in Fig. 18.

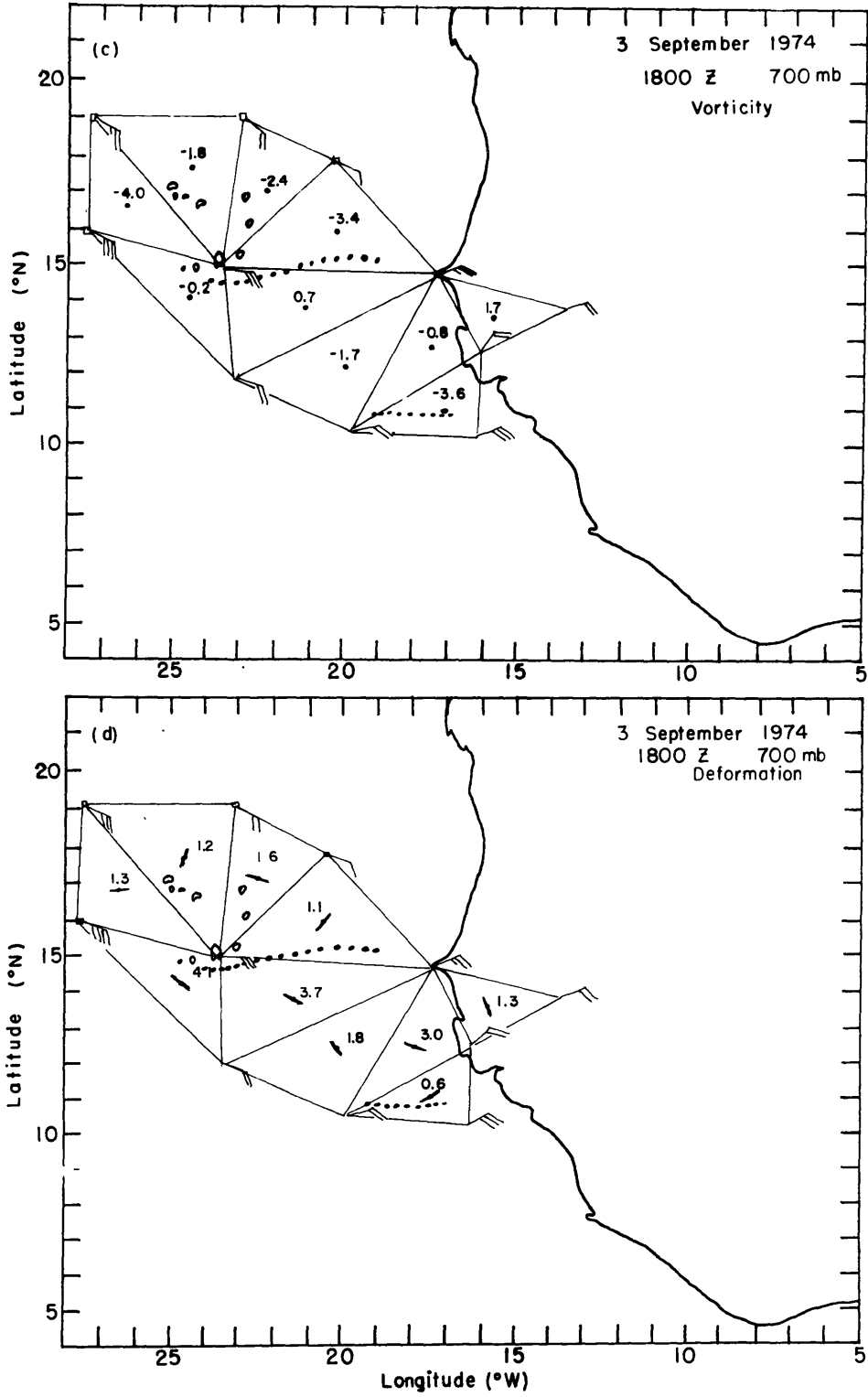


Fig. 22. (continued)

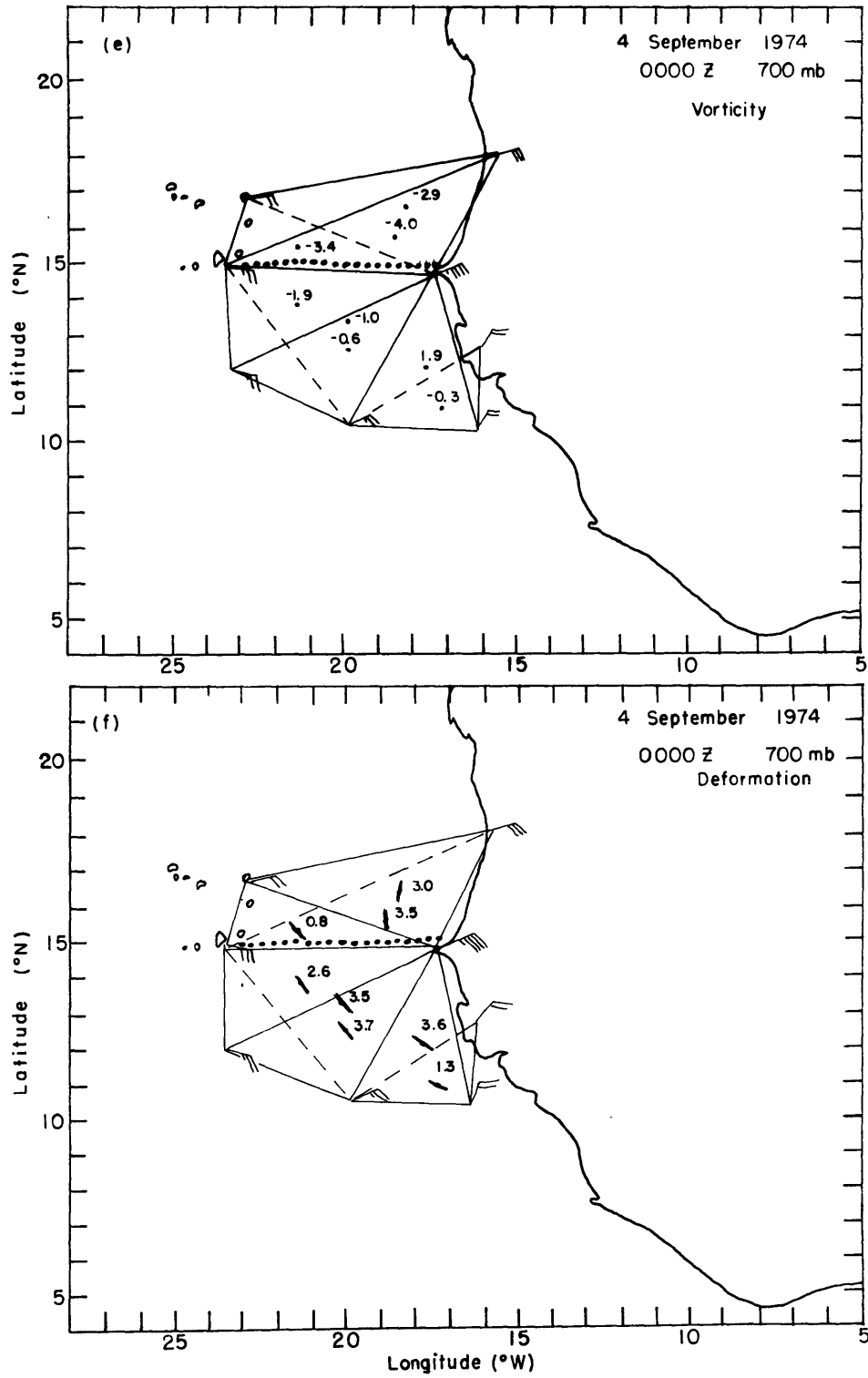


Fig. 22. (continued)

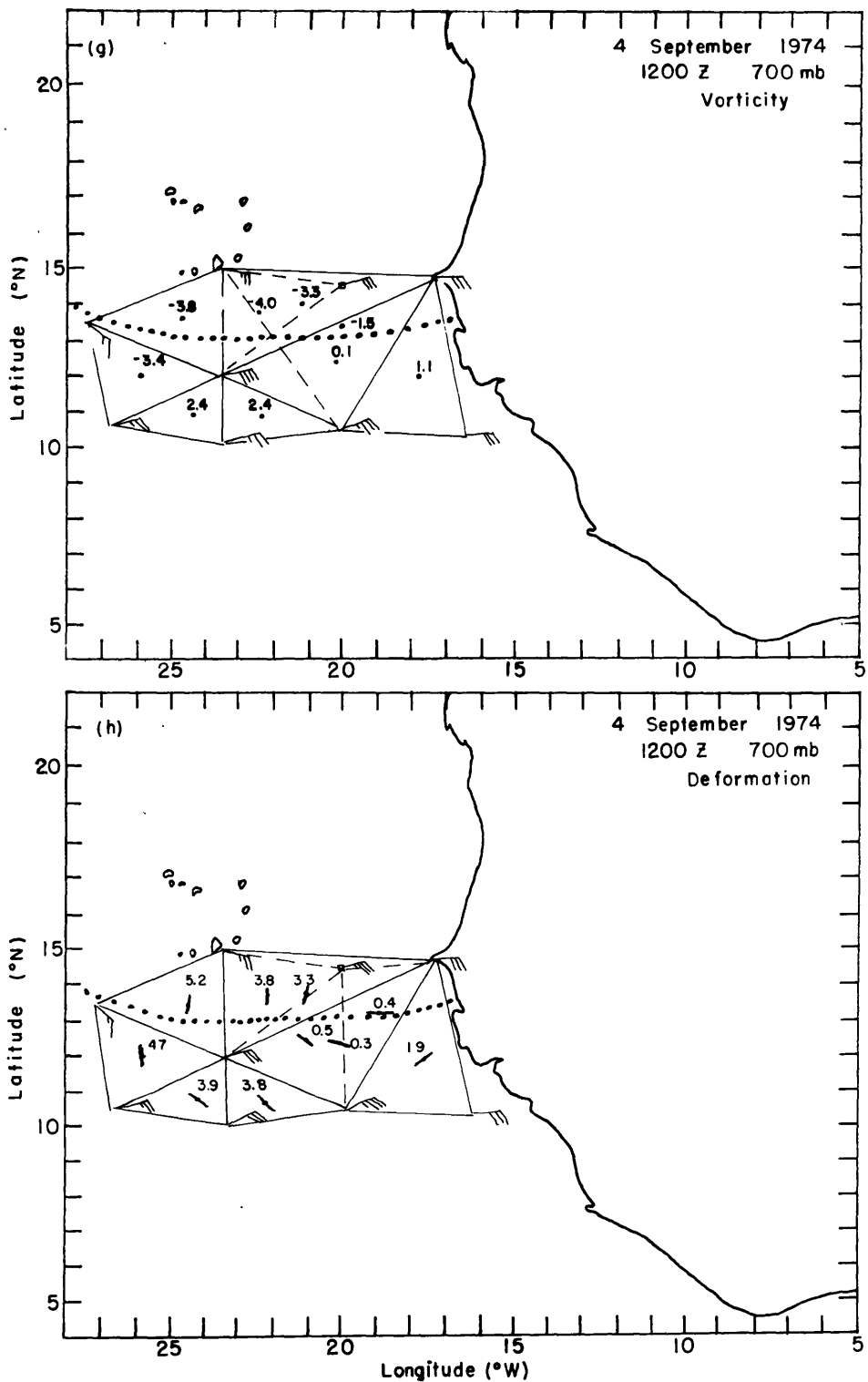


Fig. 22. (continued)

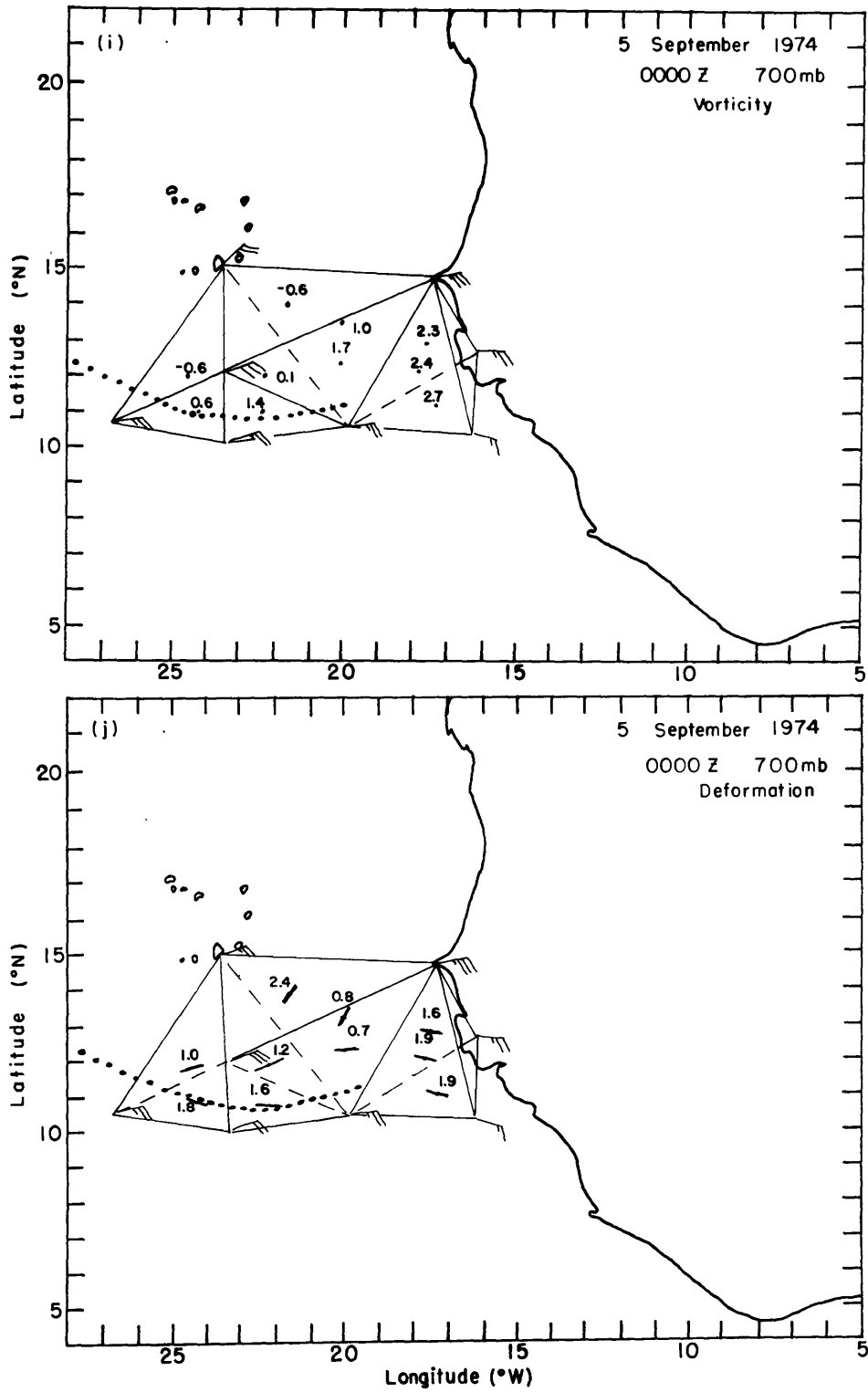


Fig. 22. (continued)

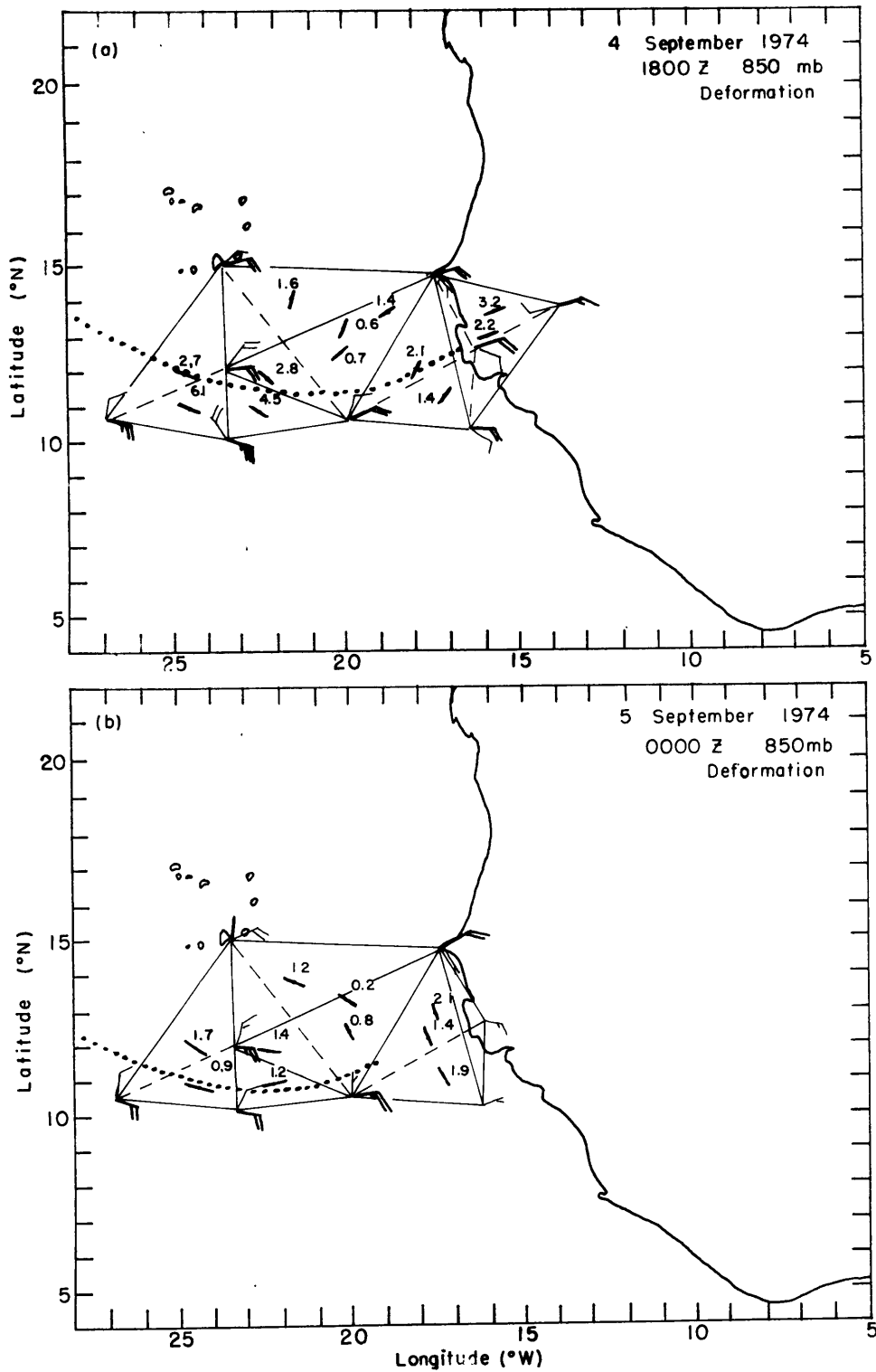


Fig. 23. 850-mb resultant deformation ( $10^{-5} \text{ s}^{-1}$ ) and axis of dilatation for (a) 1800 GMT, 4 September and (b) 0000 GMT, 5 September 1974. Light wind barbs depict the 850-mb wind direction and speed as in Fig. 18. Solid wind barbs represent the 700-850 mb wind shear using the plotting convention in Fig. 18. For further description see Fig. 22.

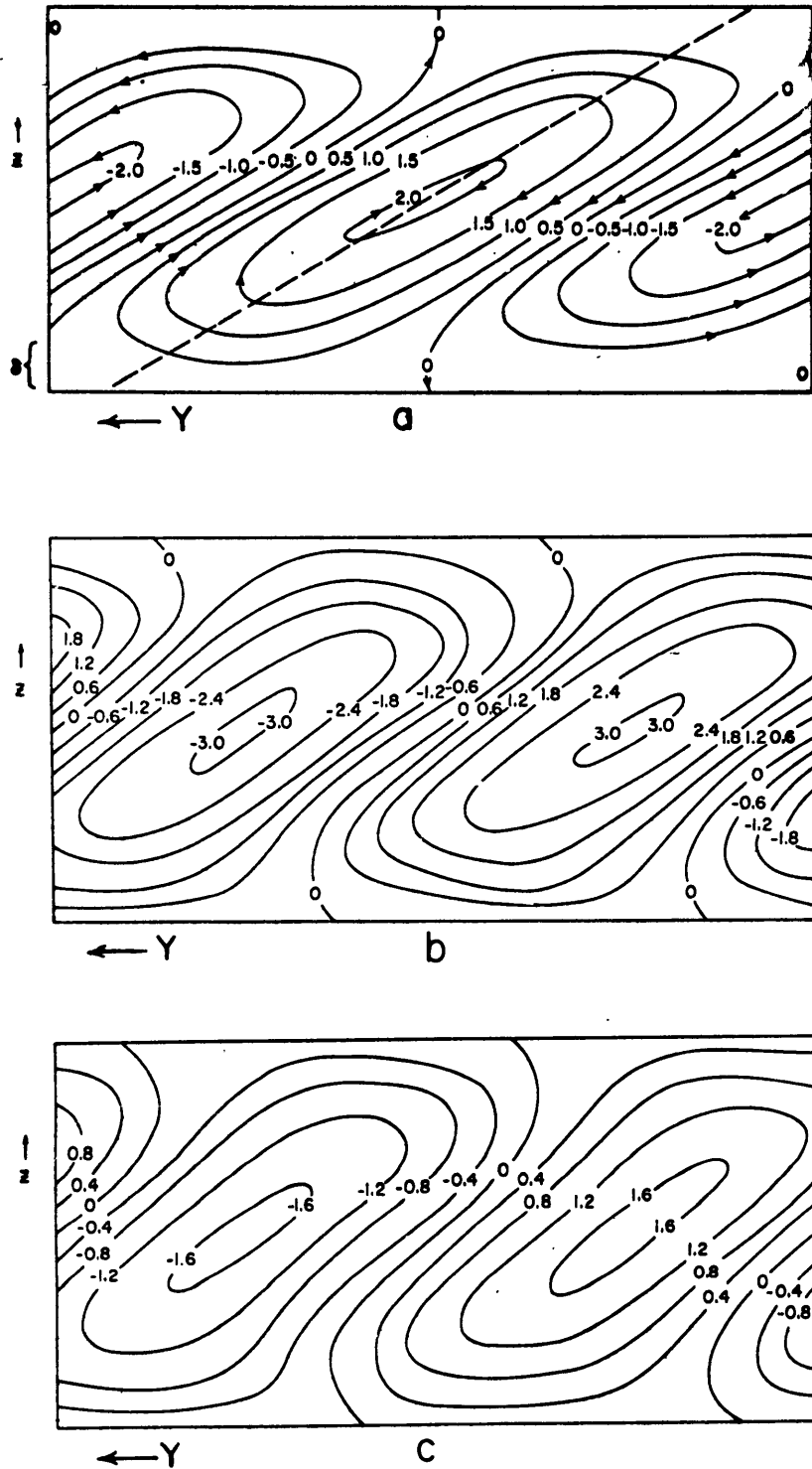


Fig. 24. (a) Streamfunction, (b) along-line velocity perturbation, and (c) temperature perturbation characterizing the onset of symmetric inertial instability in a diffusive fluid with no-slip boundaries, for a moderate value of the viscosity parameter. The horizontal domain spans one wavelength. The units are all non-dimensional (from Emanuel, 1979a).

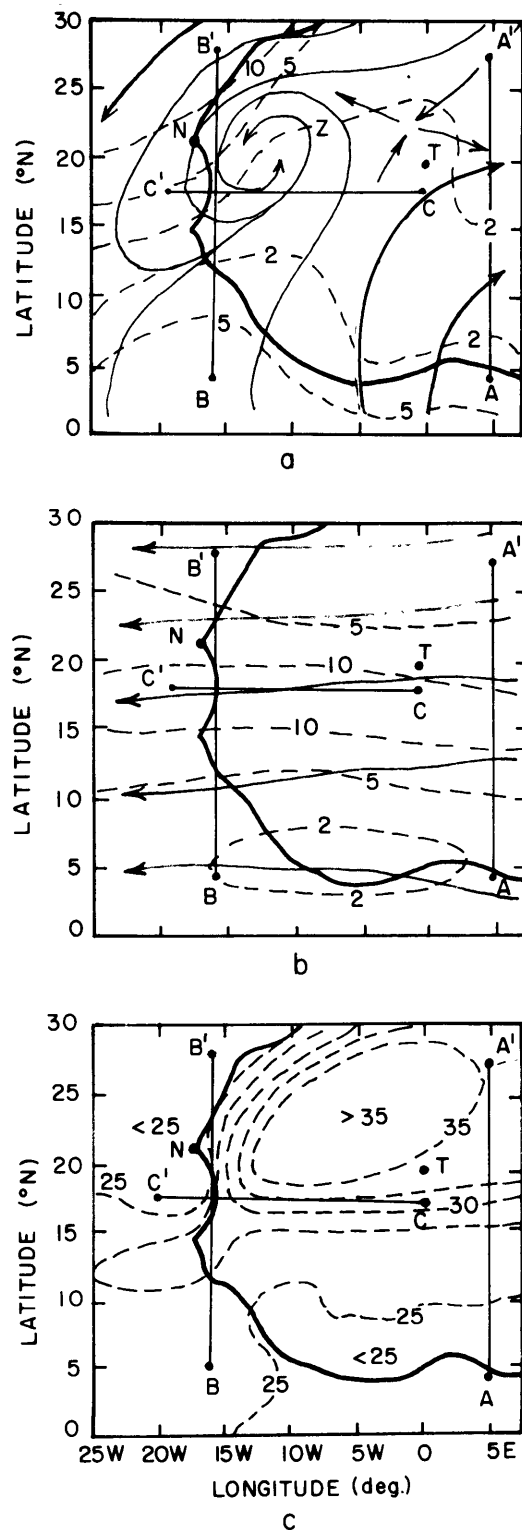


Fig. 25. (a) Mean surface streamlines (solid) and isotachs (dashed, in  $m s^{-1}$ ) and (b) Mean 700-mb streamlines (solid) and isotachs (dashed, in  $m s^{-1}$ ) for Phase III of GATE (from Reynolds, 1977). (c) Mean late summer daily surface temperature ( $^{\circ}C$ ) over Africa (from Burpee, 1972) and mean sea surface temperature ( $^{\circ}C$ ) for Phase III of GATE (from Krishnamurti *et al.*, 1976). Lines marked A - A', B - B', and C - C' denote positions of cross-sections discussed in the text. "N" and "T" denote the locations of stations discussed in the text.

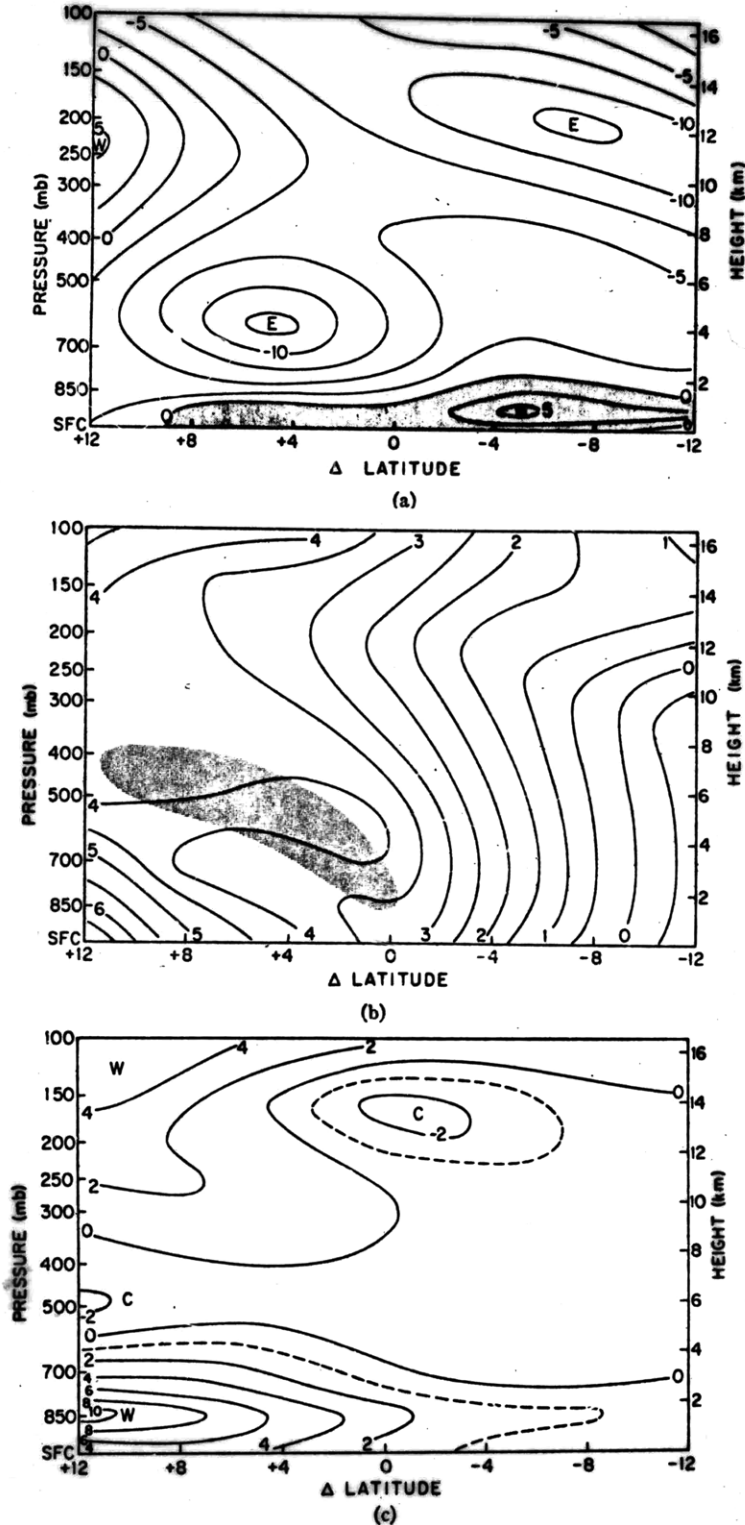


Fig. 26. Zonal mean fields for Phase III of GATE. (a) Zonal wind ( $\text{m s}^{-1}$ ), (b) vertical component of the absolute vorticity ( $10^{-5} \text{ s}^{-1}$ ), and (c) temperature deviations ( $^{\circ}\text{C}$ ) from values at  $\Delta$ -latitude = -12. In (a), positive zonal wind values are stippled. Stippled area in (b) denotes region where the gradient of the absolute vorticity changes sign.  $\Delta$ -latitude is defined as in Fig. 1 (from Reed *et al.*, 1977).

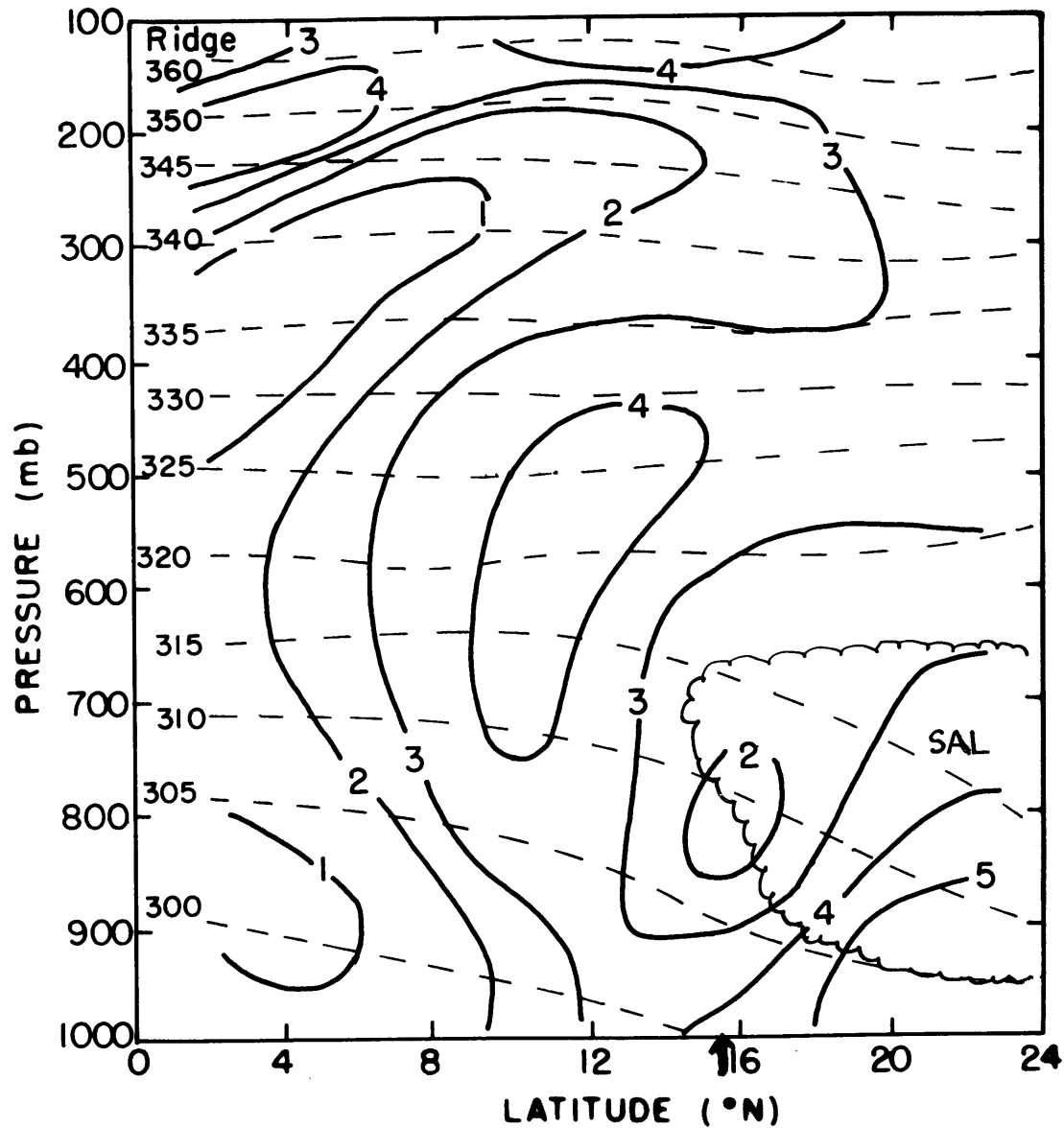
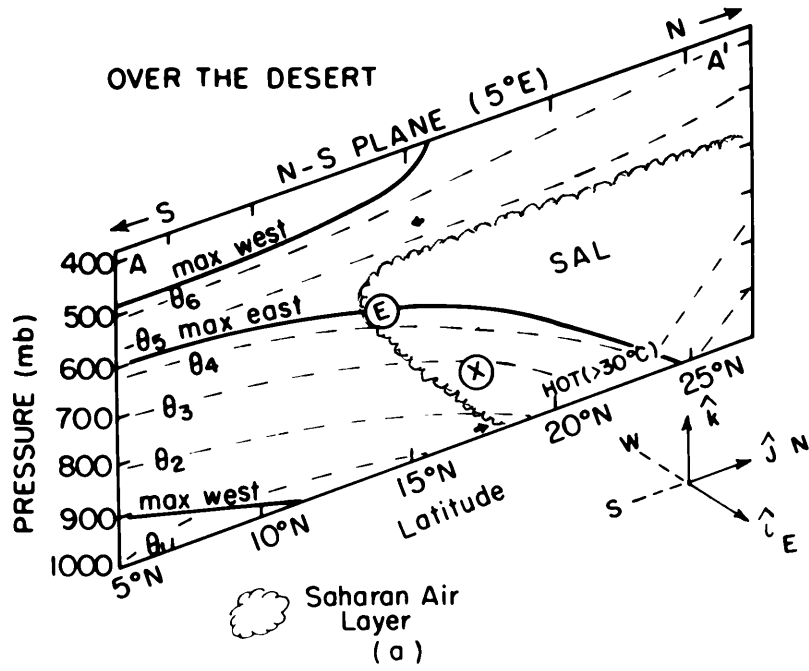
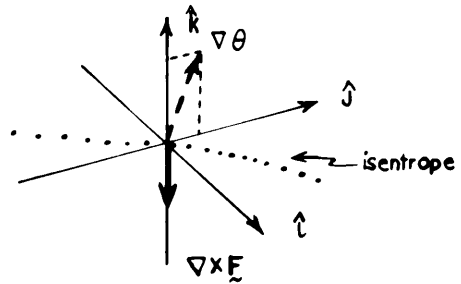
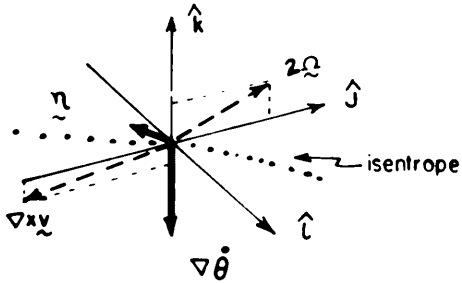


Fig. 27. North-south vertical cross-sections of the vertical component of the absolute vorticity (solid lines in units of  $10^{-5} \text{ s}^{-1}$ ) and potential temperature (dashed lines in K) for the wave ridge.  $\Delta$ -latitude is defined as in Fig. 1. The solid arrow denotes the typical position of the long convective lines, and the scalloped line marks the boundary of the SAL.



OVER THE DESERT

AT (X)



	$\zeta$	$\nabla\theta$	$\frac{dq}{dt}$
$\hat{i}$	$\geq 0$	$\approx 0$	$\approx 0$
$\hat{j}$	$< 0$	$\approx 0$	$\approx 0$
$\hat{k}$	$> 0$	$< 0$	$< 0$

	$\nabla \times \mathbf{E}$	$\nabla \theta$	$\frac{dq}{dt}$
$\hat{i}$	$\approx 0$	$\approx 0$	$\approx 0$
$\hat{j}$	$\approx 0$	$> 0$	$\approx 0$
$\hat{k}$	$< 0$	$> 0$	$< 0$

(b)

Fig. 28. Schematic diagram showing (a) the north-south cross-section over the desert: A - A'. The heavy solid lines denote the locus of the maximum wind components normal to the plane, and the circled letter (E or N), the location of the maximum wind normal to the plane. The solid arrows denote the direction and approximate magnitude of the maximum wind component parallel to the plane. The dashed lines denote isentropes. (b) Schematic diagram showing the components of the stability change and the vorticity change terms in the equation of the time rate of change of potential vorticity in the region denoted by the circled X. The dotted line indicates the slope of the isentropic surfaces.

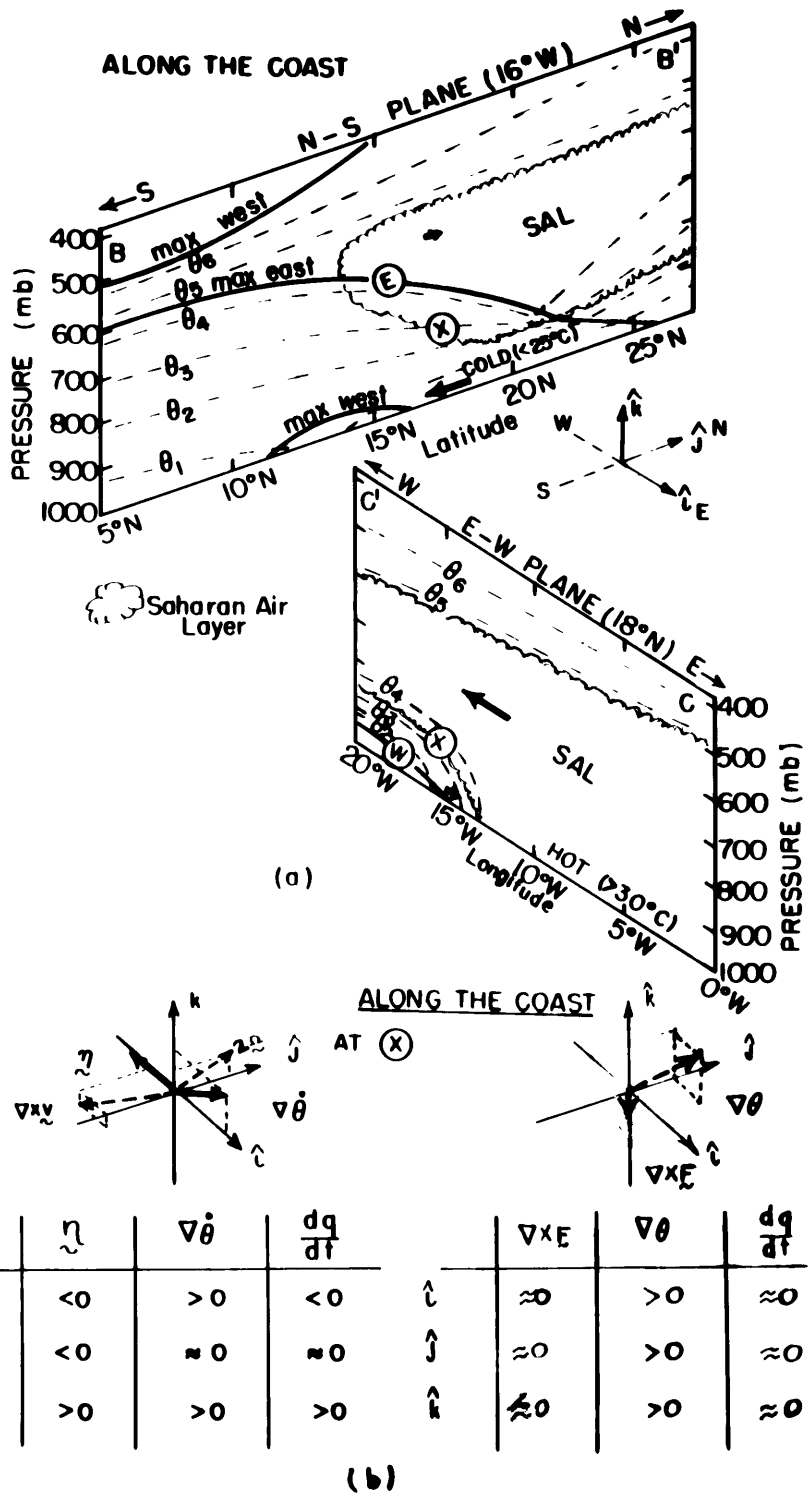


Fig. 29. Schematic diagram showing (a) the north-south and east-west cross-sections along the coast: B - B' and C - C', respectively. (b) Schematic diagram showing the components of the stability change and the vorticity change terms in the equation of the time rate of change of potential vorticity in the region denoted by the circled X. See Fig. 28 for further description.

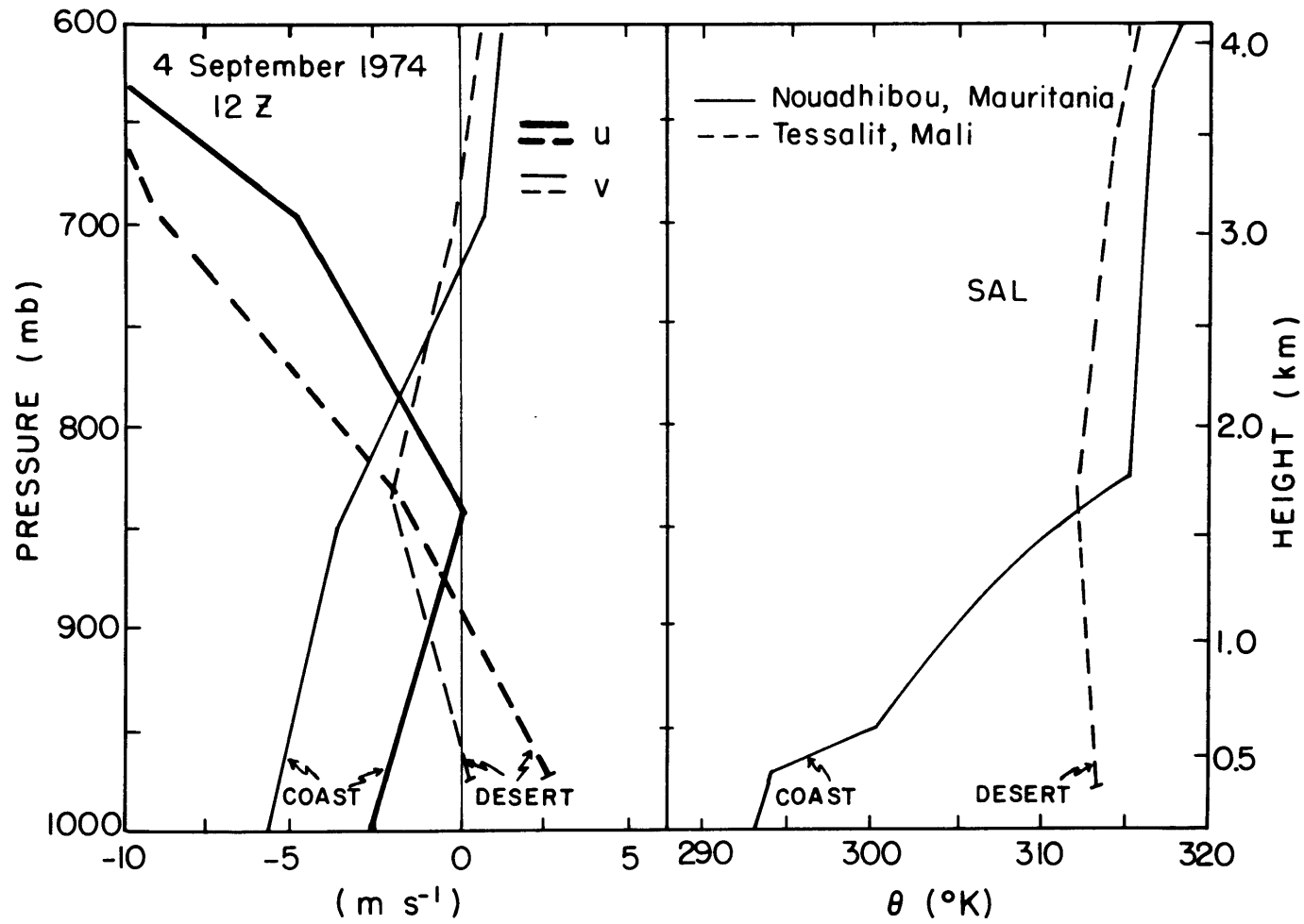


Fig. 30. Soundings from Nouadhibou, Mauritania (solid) and Tessalit, Mali (dashed) for 1200 GMT, 4 September 1974. (a) The u and v-components of the wind ( $\text{m s}^{-1}$ ), and (b) potential temperature (K).

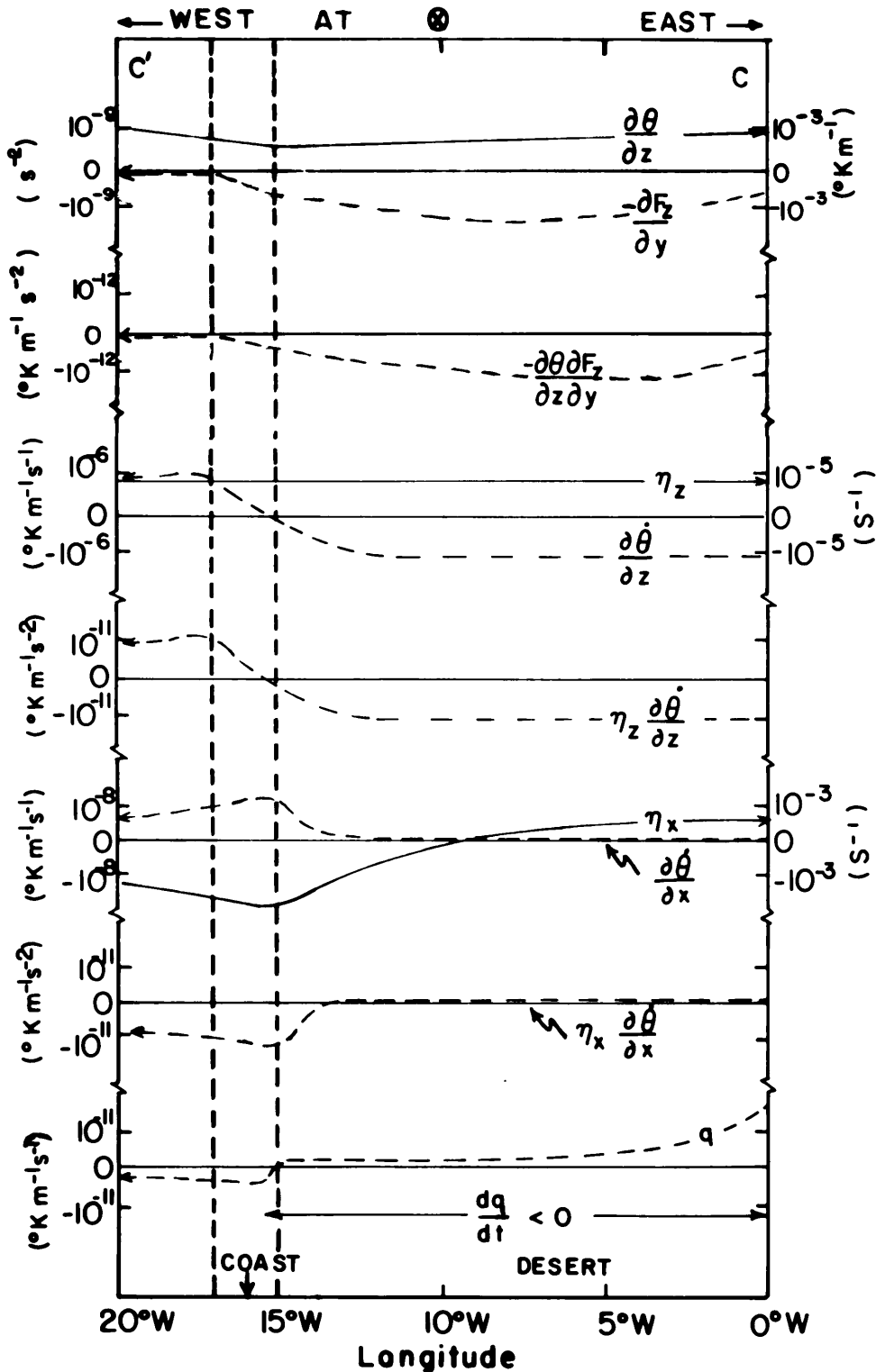


Fig. 31. Schematic diagram showing the magnitude of the components of the vorticity change and the stability change terms and the time rate of change of potential vorticity at the location in Figs. 28 and 29 denoted by the circled X at points along the east-west cross-section C-C'. The scales for the dashed curves are on the left and those for the solid curves on the right. The region from the coast eastward about 150 km is delineated by the heavy, vertical dashed lines. The coast is denoted by the arrow near 17°W.

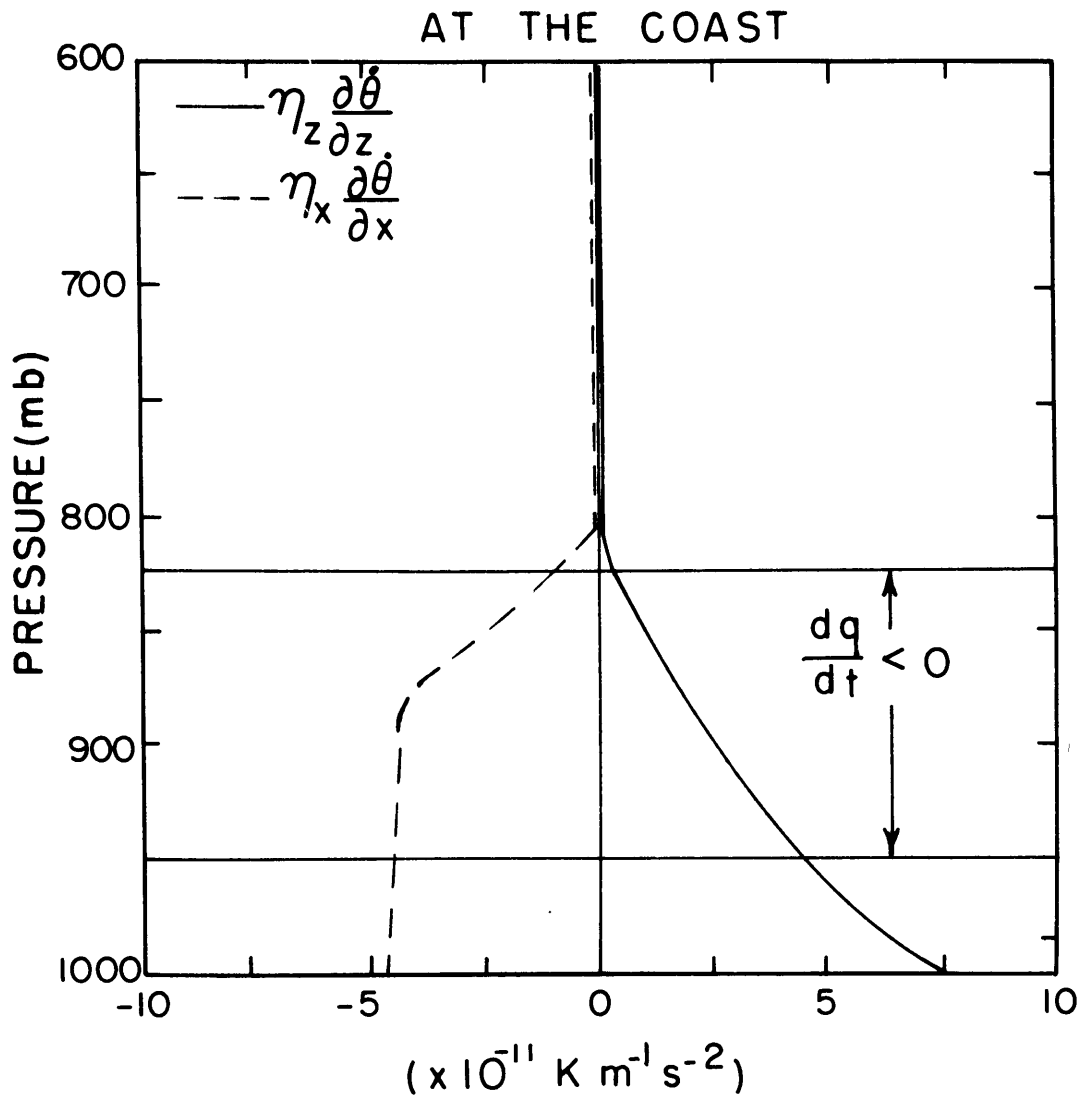


Fig. 32. Schematic diagram showing the magnitude of the components of the stability change term in the vertical for the point marked by the arrow in the coastal region of Fig. 31.

## References

- Adamski, W.J., 1979: A case study of the morphology, thermodynamics, and kinematics of a large-scale GATE cloud band. M.S. Thesis, Dept. of Atmos. Sci., Univ. of Wisconsin-Milwaukee, 50 pp.
- Anderson, R., J. Ashman, F. Bittner, G. Farr, E. Ferguson, V. Oliver, and A. Smith, 1969: Application of Meteorological Satellite Data in Analysis and Forecasting. ESSA Tech. Rept. NESC 51, National Environmental Satellite Center, Suitland, MD, 210 pp.
- Arnold, J.E., 1966: Easterly wave activity over Africa and in the Atlantic with a note on the Intertropical Convergence Zone during early July 1961. SMRP Rept. No. 65, Dept. Geophys. Sci., Univ. of Chicago, 23 pp.
- Aspliden, C.I., Y. Tourre, and J.B. Sabine, 1976: Some climatological aspects of West African disturbance lines during GATE. *Mon. Wea. Rev.*, **104**, 1029-1035.
- Austin, P.M., and S.G. Geotis, 1979: Raindrop sizes and related parameters for GATE. *J. Appl. Meteor.*, **18**, 569-575.
- Bellamy, J.C., 1949: Objective calculations of divergence, vertical velocity and vorticity. *Bull. Amer. Meteor. Soc.*, **30**, 45-50.
- Bluestein, H.B., 1977: Synoptic-scale deformation and tropical cloud bands. *J. Atmos. Sci.*, **34**, 891-900.
- Burpee, R.W., 1972: The origin and structure of easterly waves in the lower troposphere of North Africa. *J. Atmos. Sci.*, **29**, 77-90.
- Burpee, R.W., 1975: Some features of synoptic-scale waves based on compositing analysis of GATE data. *Mon. Wea. Rev.*, **103**, 921-925.
- Burpee, R.W., and G. Dugdale, 1975: A summary of weather systems affecting western Africa and the eastern Atlantic during GATE. Report on the Field Phase of the GATE Scientific Programme, GATE Rept. No. 16, W.M.O., 2.1-2.42.
- Carlson, T.N., 1969a: Synoptic histories of three African disturbances that developed into Atlantic hurricanes. *Mon. Wea. Rev.*, **97**, 256-276.
- Carlson, T.N., 1969b: Some remarks on African disturbances and their progress over the tropical Atlantic. *Mon. Wea. Rev.*, **97**, 716-726.

- Carlson, T.N., 1979: Atmospheric turbidity in Saharan dust outbreaks as determined by analyses of satellite brightness data. *Mon. Wea. Rev.*, **107**, 322-335.
- Carlson, T.N., and J.M. Prospero, 1972: The large-scale movement of Saharan air outbreaks over the northern equatorial Atlantic. *J. Appl. Meteor.*, **11**, 283-297.
- Ceselski, B.F., and L.L. Sapp, 1975: Objective wind field analysis using line integrals. *Mon. Wea. Rev.*, **103**, 89-100.
- Charney, J.G., 1971: Tropical cyclogenesis and the formation of the Intertropical Convergence zone. *Mathematical Problems in the Geophysical Sciences; 1. Geophysical Fluid Dynamics, Lectures in Applied Mathematics*, Vol. 13, Amer. Math. Soc., 355-368.
- Dunn, G.E., 1940: Cyclogenesis in the tropical Atlantic. *Bull. Amer. Meteor. Soc.*, **21**, 215-229.
- Eldridge, R.H., 1957: A synoptic study of West African disturbance lines. *Quart. J. Roy. Meteor. Soc.*, **83**, 303-314.
- Eliassen, A., and E. Kleinschmidt, 1957: Dynamic meteorology. *Handbuch der Physik*, **58**, Berlin, Springer-Verlag, 1-154.
- Emanuel, K.A., 1978: Inertial stability and mesoscale convective systems. Ph.D Thesis, Dept. of Meteor., M.I.T., 207 pp.
- Emanuel, K.A., 1979a: Inertial stability and mesoscale convective systems. Preprints Eleventh Severe Storms Conference, Kansas City, MO, Amer. Meteor. Soc., 421-426.
- Emanuel, K.A., 1979b: Inertial instability and mesoscale convective systems. Part I: linear theory of inertial instability in rotating viscous fluids. *J. Atmos. Sci.*, **36**, 2425-2449.
- Ertel, H., 1942: Ein neuer hydrodynamischer Wirbelsatz. *Meteor. Z.*, **59**, 277-281.
- Frank, N., 1969: The "inverted V" cloud pattern- an easterly wave? *Mon. Wea. Rev.*, **97**, 130-140.
- Frank, N., 1971: A note on Atlantic tropical systems and cloud clusters as related to GATE. Experiment Design Proposal for the GARP Atlantic Tropical Experiment, Vol. 2 (Annexes), ICSU/WMO, Annex VI.
- Geiger, R., 1966: *Climate near the ground*. Harvard University Press, 611 pp.
- Gidel, L.T., and M.A. Shapiro, 1979: The role of clear air turbulence in the production of potential vorticity in the vicinity of upper tropospheric jet stream-frontal systems. *J. Atmos.*

*Sci.*, **36**, 2125-2138.

Hamilton, R.A., and J.W. Archbold, 1945: Meteorology of Nigeria and adjacent territory. *Quart. J. Roy. Meteor. Soc.*, **71**, 231-262.

Hoskins, B.J., 1974: The role of potential vorticity in symmetric stability and instability. *Quart. J. Roy. Meteor. Soc.*, **100**, 480-482.

Houze, R.A., 1977: Structure and dynamics of a tropical squall-line system. *Mon. Wea. Rev.*, **105**, 1540-1567.

Houze, R.A., and C.P. Cheng, 1977: Radar characteristics of tropical convection observed during GATE: Mean properties and trends over the summer season. *Mon. Wea. Rev.*, **105**, 964-980.

Hudlow, M.D., 1979: Mean rainfall patterns for the three phases of GATE. *J. Appl. Meteor.*, **18**, 1656-1669.

Hudlow, M.D., and V.L. Patterson, 1979: GATE Radar Rainfall Atlas. NOAA Special Rept., Center for Environmental Assessment Services, 155 pp.

Hudlow, M.D., R. Arkell, V. Patterson, P. Pytlowany, F. Richards, and S. Geotis, 1979: Calibration and intercomparison of the GATE C-band radars. NOAA Tech. Rept., Center for Environmental Assessment Services, 98 pp.

Joint Organizing Committee for GARP, 1970: Report of the first session of the JOC Study Group on Tropical Disturbances. Appendix 1 in The Planning of GARP Tropical Experiments, GARP Publication Series No. 4, WMO, 70 pp.

Karyampudi, V.M., 1979: A detailed synoptic-scale study of the structure, dynamics, and radiative effects of the Saharan Air Layer over the eastern tropical Atlantic during the GARP Atlantic Tropical Experiment. M.S. Thesis, Dept. of Meteor., Penn. State Univ., 136 pp.

Kennedy, P.J., and M.A. Shapiro, 1975: The energy budget in a clear air turbulence zone as observed by aircraft. *Mon. Wea. Rev.*, **103**, 650-654.

Krishnamurti, T.N., V. Wong, H.L. Pan, G. Van Dam, and D. McClellan, 1976: Sea Surface Temperatures for GATE. Rept. No. 76-3, Dept. of Meteor., Florida State Univ., Tallahassee, FL, 268 pp.

Kuettner, J.P., D.E. Parker, D.R. Rodenhuis, H. Hoerber, H. Kraus, and G. Philander, 1974: GATE: final international scientific plans. *Bull. Amer. Meteor. Soc.*, **55**, 711-744.

Leary, C.A., 1979: Behavior of the wind field in the vicinity of a cloud cluster in the intertropical

convergence zone. *J. Atmos. Sci.*, **36**, 631-639.

Leary, C.A., and R.A. Houze, 1979: The structure and evolution of convection in a tropical cloud cluster. *J. Atmos. Sci.*, **36**, 437-457.

Lilly, D.K., and P.J. Kennedy, 1973: Observations of a stationary mountain wave and its associated momentum flux and energy dissipation. *J. Atmos. Sci.*, **30**, 1135-1152.

López, R.E., 1973: Cumulus convection and larger scale circulations II. Cumulus and mesoscale interactions. *Mon. Wea. Rev.*, **101**, 856-870.

López, R.E., 1976: Radar characteristics of the cloud populations of tropical disturbances in the northwest Atlantic. *Mon. Wea. Rev.*, **104**, 268-288.

Marks, F.D., and M.D. Hudlow, 1976: A study of the precipitating cloud population during GATE. Preprint volume 17th Conference on Radar Meteor., Amer. Meteor. Soc., Boston, MA, 498-504.

Mass, C., 1979: A linear primitive equation model of African wave disturbances. *J. Atmos. Sci.*, **36**, 2075-2092.

McIntyre, M.E., 1970: Diffusive destabilization of the baroclinic circular vortex. *Geophys. Fluid Dyn.*, **1**, 19-58.

Norquist, D.C., E.E. Recker and R.J. Reed, 1977: The energetics of African wave disturbances as observed during Phase III of GATE. *Mon. Wea. Rev.*, **105**, 334-342.

Ooyama, K., and S. Esbensen, 1977: Rawinsonde data quality. Report of the U.S. GATE Central Program Workshop, 25 July-12 August, NCAR, Boulder, CO, 131-164.

Payne, S.W., and M.M. McGarry, 1977: The relationship of satellite inferred convective activity to easterly waves over West Africa and the adjacent ocean during Phase III of GATE. *Mon. Wea. Rev.*, **105**, 413-420.

Pestaina-Haynes, M., and G.L. Austin, 1976: Comparison between maritime tropical (GATE and Barbados) and continental mid-latitude (Montreal) precipitation lines. *J. Appl. Meteor.*, **15**, 1077-1082.

Petterssen, S., 1956: *Weather Analysis and Forecasting*. Vol. 1, McGraw-Hill, 428 pp.

Piersig, W., 1936: Schwankungen von Luftdruck und Luftbewegung sowie ein Beitrag zum Wettergeschehen in Passategebiet des ostlichen Nordatlantischen Ozeans. *Arch. Deut. Seewarte*, **54**, No. 6. Parts II and III have been translated and printed, 1944: The cyclonic

- disturbances of the subtropical eastern North Atlantic. *Bull. Amer. Meteor. Soc.*, **25**, 2-17.
- Prospero, J.M., R.T. Nees, and D. Savoie, 1977: Atmospheric Aerosol Measurements during GATE. Tech. Rept. TR76-5, Univ. of Miami, Miami, FL, 50 pp.
- Raymond, D.J., 1977: Instability of the low-level jet and severe storm formation. Preprints Tenth Severe Storms Conference, Omaha, NB, Amer. Meteor. Soc., 515-520.
- Reed, R.J., 1978: The structure and behavior of easterly waves over West Africa and the Atlantic. *Meteorology Over the Tropical Oceans*. Roy. Meteor. Soc., Bracknell, U.K., 57-71.
- Reed, R.J., and E.E. Recker, 1971: Structure and properties of synoptic-scale wave disturbances in the equatorial western Pacific. *J. Atmos. Sci.*, **28**, 1117-1133.
- Reed, R.J., D.C. Norquist and E.E. Recker, 1977a: The structure and properties of African wave disturbances as observed during Phase III of GATE. *Mon. Wea. Rev.*, **105**, 317-333.
- Reed, R.J., E.E. Recker, and D.C. Norquist, 1977b: The energetics of African wave disturbances. Paper presented at WMO Conference on the Energetics of the Tropical Atmosphere, Tashkent, U.S.S.R., 14-21 September.
- Reeves, R.W., 1978: GATE Convection Subprogram Data Center: Final report on rawinsonde data validation. NOAA Tech. Rept. EDS 29, NOAA, U.S. Dept. of Commerce, Washington, D.C., 31 pp.
- Reeves, R.W., and S. Esbensen, 1977: Appendix to rawinsonde data quality. GATE Workshop recommendations for integrating USSR RKZ and US VIZ rawinsonde thermodynamic observations. Report of the U.S. GATE Central Program Workshop, 25 July-12 August, NCAR, Boulder, CO, 165-168.
- Reeves, R.W., C.F. Ropelewski, and M.D. Hudlow, 1979: Relationship between large-scale motion and convective precipitation during GATE. *Mon. Wea. Rev.*, **107**, 1154-1168.
- Reynolds, R., 1977: Large-scale (A-scale) mean features of the GATE Atmosphere during Phase III. Met.0.20 Tech. Note No. II/105, U.K. Meteorological Office, Bracknell, U.K., 14 pp + figures.
- Riehl, H., 1948: Waves in the easterlies and the polar front in the tropics. Misc. Rept. No. 17, Dept. of Meteor., Univ. of Chicago, 79 pp.
- Riehl, H., and J.S. Malkus, 1958: On the heat balance in the equatorial trough zone. *Geophysica*, **6**, 503-538.

Sadler, J.C., 1975: The monsoon circulation and cloudiness over the GATE area. *Mon. Wea. Rev.*, **103**, 369-387.

Saucier, W.J., 1955: *Principles of Meteorological Analysis*. University of Chicago Press, 438 pp.

Schaefer, J.T., and C.A. Doswell, 1979: On the interpolation of a vector field. *Mon. Wea. Rev.*, **107**, 458-476.

Smith, C.L., E.J. Zipser, S.M. Daggupati, and L. Sapp, 1975a: An experiment in tropical mesoscale analysis: Part 1. *Mon. Wea. Rev.*, **103**, 878-892.

Smith, C.L., E.J. Zipser, S.M. Daggupati, and L. Sapp, 1975b: An experiment in tropical mesoscale analysis: Part 2. *Mon. Wea. Rev.*, **103**, 893-903.

Staley, D.O., 1960: Evaluation of potential vorticity changes near the tropopause and the related vertical motions, vertical advection of vorticity, and transfer of radioactive debris from stratosphere to troposphere. *J. Meteor.*, **17**, 591-620.

Stone, P.H., 1966: On non-geostrophic baroclinic stability. *J. Atmos. Sci.*, **23**, 390-400.

Thompson, R.M., S.W. Payne, E.E. Recker, and R.J. Reed, 1979: Structure and properties of synoptic scale wave disturbances in the intertropical convergence zone in the eastern Atlantic. *J. Atmos. Sci.*, **36**, 53-72.

Vehrencamp, 1953: Experimental investigation of heat transfer at an air-earth surface, *Trans. Amer. Geophys. Union*, **34**, 22-30.

Warner, C., J. Simpson, D. W. Martin, D. Suchman, F.R. Mosher, and R.F. Reinking, 1979: Shallow convection on day 261 of GATE: Mesoscale arcs. *Mon. Wea. Rev.*, **107**, 1617-1635.

Zipser, E.J., 1969: The role of organized unsaturated convective downdrafts in the structure and rapid decay of an equatorial disturbance. *J. Appl. Meteor.*, **8**, 799-814.

Zipser, E.J., 1977: Mesoscale and convective-scale downdrafts as distinct components of squall-line structure. *Mon. Wea. Rev.*, **105**, 1568-1589.

Zipser, E.J., and C. Gautier, 1978: Mesoscale events within a GATE tropical depression. *Mon. Wea. Rev.*, **106**, 789-805.

### Biographical Note

Frank Marks was born 24 October 1951, at West Point, NY. On 1 July 1973 he married the former Anita Hartstone of Newton Centre, MA. He has one daughter, Sara Rebecca, who was born on 7 September 1976.

He attended Lakeland Senior High School and graduated in June 1969. While in high school he was active in a student run weather club. The students took observations, plotted their own maps from teletype data, and made forecasts for the school and over a local radio station. From September 1969 to May 1973 he attended Belknap College in Center Harbor, N.H. majoring in Meteorology and received a B.S. in Meteorology in May 1973. From September 1973 to July 1975 he attended M.I.T. in the Department of Meteorology and received the S.M. in Meteorology. The thesis title was "A Study of the Mesoscale Precipitation Patterns Associated with the New England Coastal Front".

During the summer of 1974, he participated in GATE, working in Dakar, Senegal, as part of the UCAR Student Program. He worked for Dr. David Rodenhuis of the University of Maryland and Dr. Alan Betts of the Colorado State University in the Special Analysis Group of the Convection Subprogram. As part of his duties he analyzed different GATE data sets to check their quality and to compare the different data systems. During the field phase of GATE, he did a study of the diurnal variation of precipitating convection using radar data transmitted to Dakar from the ship arrays which was published in GATE Report 14. During the month of December 1978, he went to Bintulu, West Malaysia on the north coast of Borneo as a member of the M.I.T. Weather Radar Project's team that made measurements of the precipitation in that region with the M.I.T. WR73 radar in cooperation with the Winter Monsoon Experiment.

He is a member of the American Meteorological Society (A.M.S.) and has presented a number of papers at A.M.S. sponsored conferences on radar meteorology and weather analysis and forecasting. He has also authored or coauthored two papers for professional journals.